Static and Dynamic Magnetic Properties of Exchange-coupled Thin Film Systems

im Fachbereich Physik
der Freien Universität Berlin
eingereichte Dissertation
von

Bin Zhang

Berlin, 2014

1st Referee:	Prof. Dr. Wolfgang Kuch Freie Universität Berlin
2nd Referee:	Prof. Dr. Katharina J. Franke Freie Universität Berlin

Tag der Disputation: 24.10.2014

Abstract

This thesis focuses on the coupling and dynamics of magnetic films. Epitaxial FM/Mn/FM [FM (ferromagnetic): Ni, Co] trilayers with a varied thickness (wedged) Mn layer were grown on Cu(001) and studied by magneto-optical Kerr effect measurements. The bottom FM film as well as the Mn film exhibit a layer-by-layer growth mode, which allows to modify both interface roughnesses on the atomic scale by tuning the thicknesses of the films to achieve a certain filling of their topmost atomic layers.

For the Co/Mn/Co systems, the onset of antiferromagnetic order in the Mn layer at room temperature was found at a higher thickness (t_{AFM}) for a filled compared to a half-filled topmost atomic layer of the bottom Co layer. Magnetization loops with only one step were found for half-filled topmost atomic layer of the bottom Co film, while loops with two separate steps have been observed in trilayers with an integer number of atomic layers in the bottom Co film. The small coercivity of the top Co film shows an oscillation with 1 ML period as a function of the Mn thickness above 10 ML, which is interpreted as the influence of the atomic-scale control of the interface roughness on the interface exchange coupling between the antiferromagnetic Mn and the top ferromagnetic Co layer. The strength of the magnetic interlayer coupling between the top and bottom Co layers through the Mn layer for an integer number of atomic layers in the bottom Co layer exhibits an oscillation with a period of 2 ML Mn thickness, indicative of direct exchange coupling through the antiferromagnetic Mn layer. A long-period interlayer coupling of the two FM layers with antiparallel coupling is observed and attributed to indirect exchange coupling of the Rudermann-Kittel-Kasuya-Yosida type.

After deposition of Ni on Mn wedge/atomically filled Co film, the coercivity is enhanced compared to Mn/Co or Co/Mn/Co samples. In the Ni/Mn/Ni trilayer, the top Ni layer also shows a higher coercivity than the bottom layer above 8 ML Mn thickness. Comparing the medium energy electron diffraction oscillations during growth of Mn on Ni and Ni on Cu(001) shows that the surface roughness is reduced by the Mn layer. This indicates that the coercivity of Ni/Mn depends on the interface roughness, i.e., a smoother interface shows a higher coercivity.

The magnetization dynamics of Co wedge/Ni bilayers induced by fs laser pulses close to the spin-reorientation transition (SRT) between out-of-plane and in-plane magnetization has been investigated by photoelectron emission microscopy with pump-probe measurements. The response of the magnetization of the Co layer close to the SRT shows a slower recovery after demagnetization comparing to the region far away from SRT, probably due to a lower Curie temperature.

Kurzfassung

Diese Arbeit befasst sich mit der Kopplung und der Dynamik von magnetischen Schichtsystemen. FM/Mn/FM [FM (Ferromagnet): Ni, Co] Dreilagensysteme mit einer Mn-Lage variable Dicke (Keilform) wurden epitaktisch auf Cu(001) aufgewachsen und mit Hilfe des magneto-optischen Kerr-Effektes untersucht. Die untere FM-Schicht und die Mn-Schicht zeigen lagenweises Wachstum. Dies ermöglicht die Kontrolle der Rauigkeit beider Grenzfläche auf atomarer Skala durch Variation der Schichtdicken, um einen unterschiedlichen Grad an Abgeschlossenheit der obersten atomaren Lage zu erreichen.

Im Co/Mn/Co-Dreilagensystem zeigte sich, dass die antiferromagnetische Ordnung der Mn-Schicht bei Raumtemperatur bei größeren Schichtdicken (Mindestdicke t_{AFM}) einsetzt, wenn die oberste atomare Lage der unteren Co-Schicht vollständig abgeschlossen ist, als wenn diese halb gefüllt ist. Für halb gefüllte atomare Lagen der unteren Co-Schicht zeigten sich Magnetisierungskurven mit nur einer Stufe, während für Dreilagensysteme mit einer ganzzahligen Anzahl an atomaren Lagen Kurven mit zwei voneinander getrennten Stufen beobachtet wurden. Die kleinere Koerzivität der oberen Co-Schicht weist oberhalb von 10 ML eine Oszillation mit einer Periode von einer Monolage als Funktion der Mn-Schichtdicke auf. Diese lässt sich auf die Kontrolle der Grenzflächenrauigkeit auf atomarer Ebene und den dadurch erzielten Einfluss auf die Austauschkopplung an der Grenzfläche zwischen antiferromagnetischer Mn-Schicht und der oberen ferromagnetischen Co-Schicht zurückführen. Die Kopplungsstärke zwischen der oberen und der unteren Co-Schicht über die Mn-Schicht weist für eine ganze Anzahl atomarer Lagen der unteren Co-Schicht Oszillationen mit einer Periode von 2 ML auf, die auf eine direkte Austauschkopplung über die antiferromagnetische Mn-Schicht hindeuten. Des Weiteren zeigte sich eine Variation der Kopplung zwischen den FM-Schichten mit einer längeren Periode und antiparalleler Kopplung, die einer indirekten Austauschwechselwirkung im Sinne einer Rudermann-Kittel-Kasuya-Yosida-Kopplung zugeordnet wurde.

Nach Aufwachsen von Ni auf einer keilförmigen Mn-Schicht auf einer atomar abgeschlossenen Co-Schicht erhöht sich die Koerzitivität gegenüber Mn/Co- bzw. Co/Mn/Co-Proben. Im Ni/Mn/Ni-Dreischichtsystem zeigt die obere Ni-Schicht ebenfalls eine höhere Koerzitivität als die untere Ni-Schicht für Mn-Schichten mit einer Dicke oberhalb von 8 ML. Der Vergleich der Intensitäts Oszillationen der Beugung von Elektronen mittlerer Energie während des Aufwachsens von Mn auf Ni sowie von Ni auf Cu(001) zeigt, dass die Oberflächenrauigkeit durch die Mn-Schicht reduziert wird. Dies deutet darauf hin, dass die Koerzitivität von Ni/Mn von der Rauigkeit der Grenzfläche abhängt, d.h. eine glattere Grenzfläche führt zu einer höheren Koerzitivität.

Die Magnetisierungsdynamik des Co-Keil/Ni-Doppelschichtsystems, die durch fs-Laser-Pulse nahe des Spin-Reorientierungs-Übergangs (SRT) von aus- zu in-der-Ebene-Magnetisierung hervorgerufen wird, wurde mit Photoelektronen-Emissions-Mikroskopie mittels Anrege-Abfrage-Technik untersucht. Die Reaktion der Magnetisierung der Co-Schicht nahe des SRT zeigt eine langsamere Erholung nach der Entmagnetisierung, als Weiter entfernt vom SRT, vermutlich auf Grund der SRT niedrigeren Curie-Temperatur.

Contents

Chapter 1 Introduction

Thales of Miletus first described the phenomenon of magnetism as the attraction of iron by “lodestone” at around 600 BC. It is assumed that the first direction pointers were made by balancing a piece of lodestone during the Qin dynasty more than 2000 years ago.[1] The operation of the compass for navigation in China started in the late 11th century, and one century later in Europe. People started the great voyages to explore the unknown world with the help of magnetic compasses.

The advanced applications of magnetism today are related to the technology underlying data storage and memory.[2,3] Oberlin Smith first proposed magnetic recording in 1888, and later the first magnetic recording device called telegraphone was patented by Valdemar Poulsen in 1894.[2,4] In the 1950s, the magnetic core memories created by An Wang became the dominant computer memories. A major breakthrough for the density of magnetic recording came by using read-head sensors with spin valves based on giant magneto-resistance (GMR). The GMR phenomenon was observed by Fert *et al.*[5] and Grünberg *et al.*[6] independently in 1988. The structure of a typical GMR spin valve consists of two ferromagnetic (FM) layers separated by a nonmagnetic spacer and an antiferromagnetic (AFM) layer in contact with one of the ferromagnetic layers. The thickness of the spacer is chosen such that there is little or no exchange coupling between the two FM layers. The magnetization of one of the FM layers is pinned by the strong coupling to the AFM layer, and thus this FM layer is called a “pinned” or reference layer. On the other hand, the magnetization of the other FM layer is free to rotate to respond to an external field, and thus it is called a “free” layer. If the magnetic moments in the pinned and free layers are parallel, the current can flow easily throughout the structure, and the resistance is low. However, if the layers are magnetized antiparallel, the current is impeded, and the resistance is high. From the variation of the resistance, we can read the information (“0” and “1”) from the magnetic disk. In the 1990s, IBM developed such GMR devices as read-head sensors for magnetic disk drives. Their introduction into the market in 1997 had an almost immediate impact on the disk drive capacity that has lasted to the present day.

The future of magnetic storage and memory technology requires smaller bit sizes and faster magnetic reversal processes. With increasing the density of the magnetic disk, the size of the particles or the magnetic pattern and the distance between bits have to be reduced, such that scientific investigations about the manipulation of the magnetization on the nanoscale and the interaction or interlayer coupling from other particles or layers become important. Nowadays the device switching times are about one nanosecond. In advanced recording studies times as short as 100 picoseconds have been achieved.[1] Studies about the origin of magnetic coupling and spin transport across interfaces and the time dependence of magnetic reversal processes are essential for applications. An important challenge is the understanding of the size and speed limits of magnetic technologies.

This doctoral thesis is about the static and dynamic properties in exchange-coupled ultrathin films. The interplay of the interlayer coupling together with the exchange bias effect are investigated in FM/AFM films with tuning the following parameters: FM/AFM interface roughness, sample temperature, film thickness. Laser-induced magnetization dynamics in Co/Ni films are presented at the end of the thesis.

1.1 Exchange bias in FM/AFM films

Exchange bias has been extensively studied because of its crucial role in spintronics devices, for example, hard disk read heads and magnetic sensors. It was first discovered in 1956 by Meiklejohn and Bean[7] when studying the Co/CoO core/shell nanoparticles, in which the magnetization loop was shifted by -1.0 kOe with a coercivity of 2.2 kOe after field cooling of the sample, as shown in Figure 1. 1. “Field cooling” means that the material with an FM-AFM interface is cooled through the Néel temperature (T_N) of the AFM, and the exchange bias is induced in the FM layer. The phenomenon of the shift of the hysteresis loop is referred to as the “exchange bias”.

Exchange bias can be qualitatively understood by assuming an exchange interaction at the AFM-FM interface.[8] We use the different stages of spin configuration of an FM/AFM bilayer to describe the exchange bias behavior as shown in Figure 1. 2. When the system is at a temperature between T_c and T_N, the direction of magnetic moments in the AFM layer is random, while the ones of the FM layer are along the external field direction [here the positive direction, Figure 1. 2(a)]. As the sample is cooling down, the moments in the AFM layer become ordered, and the spins near the interface to the FM layer will align in the positive direction, as the FM layer, due to ferromagnetic coupling between the spins in the interface (here ferromagnetic coupling is assumed). The other spins in the AFM layer will follow the AFM order as shown in Figure 1. 2(b). When the magnetic field is reversed, the spins in the FM layer start to rotate, while the AFM spins remain unchanged due to the larger anisotropy. In this case, the interaction between the AFM and FM moments at the interface energetically favors one of the two directions of the FM layer magnetization. This leads to a larger field to reverse the FM layer in the direction against the interfacial AFM spins [Figure 1. 2(c)]. When the external field changes back, the FM spins can be switched by a smaller field with the help of the interaction from the AFM layer [Figure 1. 2(e)]. After a complete measurement, the loop is shifted to the negative field direction. This is called exchange bias.

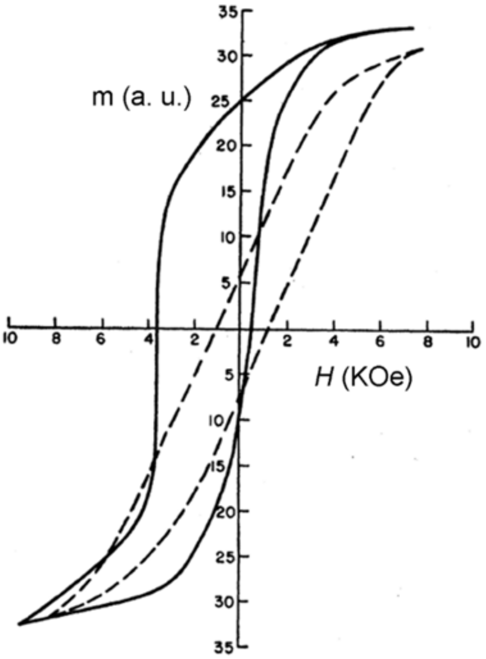

Figure 1. 1 Hysteresis loops of Co/CoO particles at $T = 77$ K after field cooling (solid line) and zero field cooling (dashed line). From the work of Meiklejohn *et al.*[9]

It is already more than half a century since the first discovery of exchange bias. Many systems containing FM-AFM interfaces have been studied including particles, thin films, and inhomogeneous materials. However, the role of many different parameters involved in exchange bias, like roughness, thickness, anisotropy, spin configuration, or temperature, is far from being understood. We will list some experiments targeting specific parameters and theoretical models from literature.[10,11]

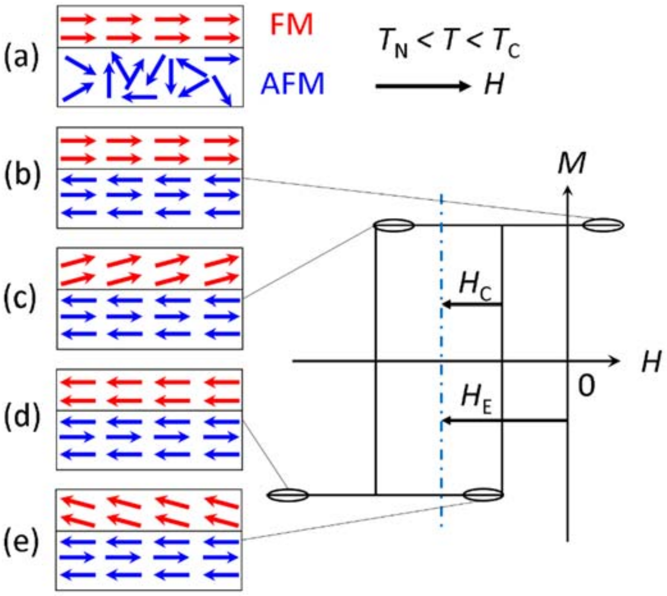

Figure 1. 2 Relative orientations of the atomic moments in the FM/AFM bilayer are shown schematically. The coercive field H_c and exchange bias field H_e are defined in the figure.

FM and AFM layer thickness dependence: From the previous studies, it seems that the exchange bias is roughly inversely proportional to the thickness of the FM layer, $H_e \sim 1/t_{FM}$, in the case when the FM layer thickness is small compared to the domain wall size as shown in Figure 1. 3 (a) and (b).[12-16] However, this linear behavior doesn't exist in ultrathin films, probably due to discontinuities in the films.[17] These results indicate that the exchange bias is an interface effect. For the coercivity, generally H_c decreases with increasing FM layer thickness. In NiCr/FeMn/NiFe and Py/CrAl films (Figure 1. 3), H_c is proportionol to $1/t_{FM}$ and $1/t_{FM}^{2/3}$, respectively.[18,19]

The dependence of H_c on the AFM thickness is complicated. Figure 1. 4 is an example of a Mn/Co bilayer. H_c is independent of t_{AFM} above 20 ML thickness of the AFM layer.[20] As t_{AFM} is reduced, H_c first increases and then decreases sharply and finally tends towards zero at a critical value of the t_{AFM}. Below this critical value of t_{AFM}, the total anisotropy energy in the AFM layer is smaller than the interfacial exchange energy, i.e., $K_{AFM}\, t_{AFM} \ll J_{ex}$ (see below). In this case, the moments in the AFM layer will switch together with those of the FM layer in the external field. Thus there will be no exchange bias in this AFM layer thickness range. The H_c behavior is also relate to T_N and T_B, which are thickness-dependent. Therefore, for thin enough AFM layers, the reduced temperature T/T_B varies with thickness. Apparently, the onset thickness of the exchange bias depends on the specific system, i.e., the temperature and the interface roughness. For thicker

AFM layers, some experiments reported that H_e decreases with increasing the AFM layer thickness in some range. This is probably due to the degeneration of the microstructure or a variation of the coupling angle between the two layers.[21,22]

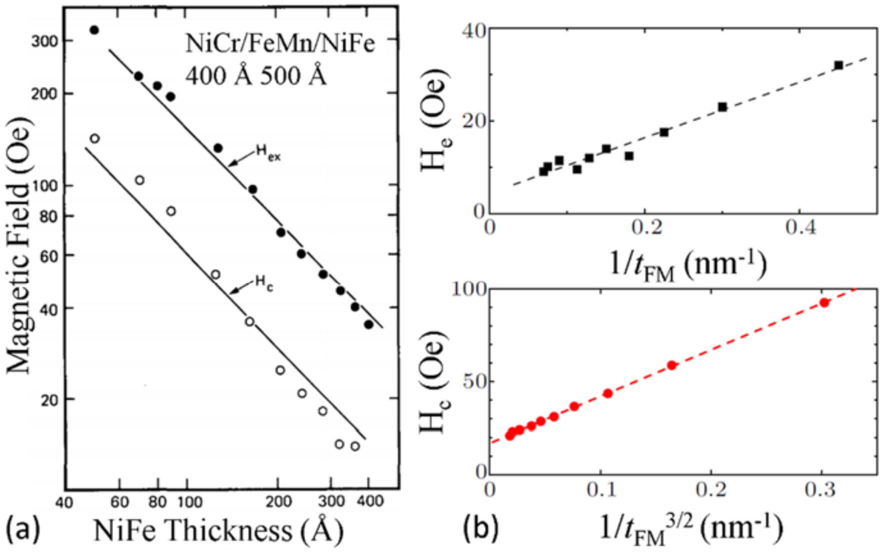

Figure 1. 3 Dependence of exchange bias H_e [filled (a) and black (b)] and coercivity H_c [open (a) and red (b)] as a function of the FM layer thickness for Py/FeMn and Py/CrAl bilayers, respectively. From the work of Mauri *et al.*[18] and Zhou *et al.*[19]

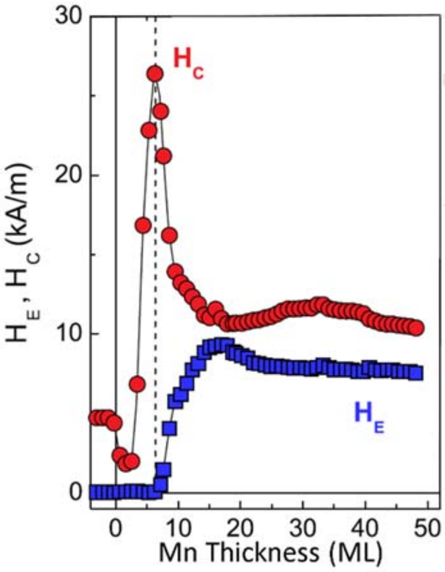

Figure 1. 4 Room temperature values of Hc and He versus the Mn thickness from MOKE measurements on Mn(001) wedge/20 ML Co(001) bilayer. From the work of Kohlhepp *et al.*[20]

Compensated-uncompensated: Due to the interfacial nature of exchange bias, H_c and H_e strongly depend on the AFM/FM interface. One issue is the orientation of the AFM spins. If the net spin on the AFM interface averaged over a microscopic length scale is zero, this is called "compensated". The other case, when some spins are parallel to each other, such that the surface magnetization is non-zero, this interface is called "uncompensated". For example, CoO(001),[23] NiO(001)[24] and FeMn(001)[25] have a compensated surface, while CoO(111) and FeMn(110) are uncompensated. Generally, one would expect that H_e should be zero for compensated surfaces, i.e., NiFe/CoO(100) and NiFe/CoO(110). However, in other compensated interfaces, like FeNi/FeMn(111),[26] not only H_e exists in these systems, but also it's value is larger than for uncompensated interfaces of the same AFM layer. This could be due to a spin rearrangement at the interface. Interface roughness could induce the locally uncompensated spins that lead to exchange bias over the macroscopic surface. Other explanation are the formation of domains in the AFM layer,[27] or non-collinear coupling at the interface.[28]

Interface roughness: Most of the studies show that the exchange bias decreases with increasing roughness,[14,29] although some systems are less sensitive to roughness or behave even in the opposite way.[30] This is independent of the interface magnetization, i.e., compensated or uncompensated. This is somehow difficult to explain. For an uncompensated AFM surface, roughness creates areas of different net magnetization, thus the average number of spins pinning the FM magnetization in one direction will reduce, which decreases H_e. However, for the compensated case, the surface remains compensated independent on the interface roughness, so the magnitude of H_e should be constant.

There exists a lot of theoretical work for explaining the exchange bias behavior. Here we present the Meiklejohn-Bean model as described in Figure 1. 2. This model is based on several assumptions: a, the interface plane is homogeneous; b, the AFM moments at the interface are uncompensated; c, there is one single domain in both the FM and AFM layer.[7-9]

In this model, the energy per unit area of an exchange bias system can be written as

$$\mathrm{E} = -\mathrm{H}M_{FM}t_{FM}\cos(\theta-\beta) + K_{FM}t_{FM}sin^2(\beta)$$
$$+K_{AFM}t_{AFM}sin^2(\alpha) - J_{ex}\cos(\beta-\alpha)$$

where H is the applied field, M_{FM} the saturation magnetization, t_{FM} and t_{AFM} the thickness of the FM and AFM layer, and K_{FM} and K_{AFM} the anisotropies of the FM and AFM layer, respectively. J_{ex} is the interface coupling constant, α, β, and θ are the angles between the M_{AFM} and the AFM anisotropy axis, the M_{FM} and the FM anisotropy axis, and the applied field and the FM anisotropy axis, respectively (see Figure 1. 5). The first term is the effect of the applied field on the FM layer, the second and the third term takes into account the effect of the FM and AFM anisotropy, and the fourth accounts for the consideration of the interface coupling. In the simplest case the FM anisotropy is assumed to be negligible. Then minimizing the energy with respect to α and β, the loop shift is found to be

$$H_e = \frac{J_{ex}}{M_{FM} t_{FM}}.$$

In other words when $K_{AFM}\, t_{AFM} \gg J_{ex}$, with keeping α small independently of β, the H_e is observed. In contrast, if $K_{AFM}\, t_{AFM} \ll J_{ex}$, it is energetically more favorable to keep small, i.e., the AFM spins follow the motion of the FM layer, and there is no exchange bias, only an increase in coercivity.

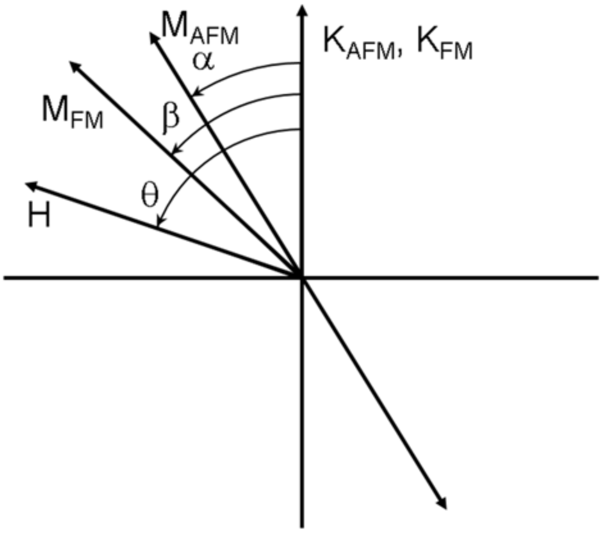

Figure 1. 5 Vector diagram of angles involved in an exchange bias system.

This model can explain some characteristics of the exchange bias. First, the magnitude of H_e is proportion to $1/t_{FM}$, which fits to most of the experiment results. Second, there exists a critical value of t_{AFM} as shown in Figure 1. 4. Binek *et al.*[31] improved this equation assuming a larger K_{AFM}, in which case H_e will reduce and tend to saturate with increasing thickness of the AFM layer. However, the value of H_e is predicted to be several orders of magnitude larger than the experimental results. To account for these discrepancies, different approximations with additional parameters are involved to improve in the simple model. For example, the formation of domains in the AFM layer, or the FM layer, interface roughness, non-collinearity of AFM and FM spins, uncompensated surface spins.

Various other models have also been proposed, for example, the Mauri domain-wall model,[32,33] the Malozemoff random interface model,[27,34] or spin-flop perpendicular coupling.[28] We don't discuss these in detail in this thesis. Often the individual approximations apply for a specific system and are not valid for other systems. Therefore, the nature of exchange bias has not been studied completely, there are still some unsolved issues.

1.2 Interlayer magnetic coupling in FM/AFM films

Magnetic interlayer exchange coupling (IEC) between two separated ferromagnetic (FM) films across a non-ferromagnetic spacer layer is crucial for many applications in modern magnetic storage devices and spin electronics. Understanding the interlayer coupling as well as magnetic properties is important to know the details of the magnetization reversal processes for applications.

IEC is found for spacer layers of nonmagnetic metals,[35-37] antiferromagnetic materials,[38-44] insulating and semiconducting spacer layers,[37,45,46] for both in-plane and out-of-plane orientation of the magnetization. The various interactions giving rise to an interlayer magnetic interaction are: a. direct ferromagnetic coupling, b. Rudermann-Kittel-Kasuya-Yosida (RKKY)-type interlayer coupling. c. dipolar interactions. Dipolar interactions originating from roughness imperfections of the layers ("orange peel" effect) lead to a parallel interlayer coupling as first pointed out by Néel.[47] Dipolar interactions are also important when the magnetic layers are not saturated and split into magnetic domains,[48] or for small samples, where the stray fields from sample edges becomes important.[49] The RKKY interaction was first proposed by Ruderman and Kittel[50] to describe the indirect interactions between nuclear spins in a metal, and then extended to electronic magnetic moments by Kasuya[51] and Yosida.[52] This model is proposed to explain the magnetic ordering of metal alloys exchange coupling between the local magnetic moments.

Concerning an AFM spacer layer, direct exchange coupling through the spacer layer may also contribute to the interlayer coupling. Systems containing AFM layers may also exhibit the exchange bias effect.[5,6] Interlayer coupling across AFM spacer layers has been studied and adjusted in several systems. Grünberg *et al*.[53] first found the AFM coupling in Fe/Cr/Fe trilayers. Later this observation has been confirmed by Carbone and Alvarado[54] and by Baibich *et al.*[5] However, no coupling oscillation was observed in early experiments. A single-period oscillatory behavior of the coupling in sputtered [Fe/Cr] multilayers corresponding to RKKY-type coupling with a period of 12.5 atomic monolayers (ML) thickness has been reported by Parkin *et al.*[43] Then a short-period oscillation with a period of 2–3 ML has been observed in epitaxial [Fe/Cr] multilayers, with a large coupling strength due to the direct *d–d* hybridization at the interface.[41,55] As shown in Figure 1. 6, the coupling of two Fe layers presents an oscillation with period of 10-12 Cr layers in a Fe/Cr/Fe sandwich grown at room temperature, while an oscillation with a period of 2 Cr layers has been observed in a Fe/Cr/Fe with well-ordered Cr interlayer. An oscillation of the sign of the interlayer coupling with two-ML periodicity has also been reported for an insulating NiO spacer layer in $[Pt/Co]_3$/NiO/$[Pt/Co]_3$ with out-of-plane anisotropy.[45] Zhuravlev *et al.* explained this oscillatory coupling by the interfacial interaction with the uncompensated NiO spins at the interface, which alternates in sign for an odd and even number of monolayers of NiO.[56] Moreover, the interfacial exchange coupling strength between FM/AFM/FM decreases with increasing temperature, however, the IEC through metal materials decreases with increasing temperature while it increases for insulating layers. A competition between the interlayer and interfacial coupling has been evidenced in Co/(Cr_2O_3, NiO)/Fe trilayers.[57] The interlayer exchange coupling dominates at higher temperatures, while the interfacial exchange interaction exists below the ordering temperature of the AFM layer. The IEC is most often observed to have a bilinear dependence i.e. to vary as a cosine function of the angle between the magnetizations in the two FM layers. Rührig *et al.*[58] found that, domain structure in a Fe/wedge Cr/Fe(001) trilayer, the moments of two FM layers present with 90° angle configuration, i.e. biquadratic coupling.

Since the spin direction of AFM materials varies on the length scale of the lattice constant, the exchange coupling between FM and AFM layers depends sensitively on the interface morphology. Single-crystalline systems provide the opportunity to tune the interface roughness on the atomic length scale. In particular, systems that exhibit a layer-by-layer growth allow to modulate the interface roughness by choosing the filling of the terminating atomic layer. The interface coupling of systems with compensated AFM interface spin structure may be enhanced by the controlled incorporation of roughness features. Oscillations of the coercivity H_c and the exchange bias field

H_e with a period of 1 ML Co thickness were found in expanded face-centered-tetragonal (e-fct) Mn/Co bilayers on Cu(001), and attributed to the influence of roughness oscillations of the AFM/FM interface due to layer-by-layer growth of the Co layer.[59,60] Atomic-scale control of the AFM–FM exchange coupling was also demonstrated in FeNi/FeMn/Co trilayers.[38]

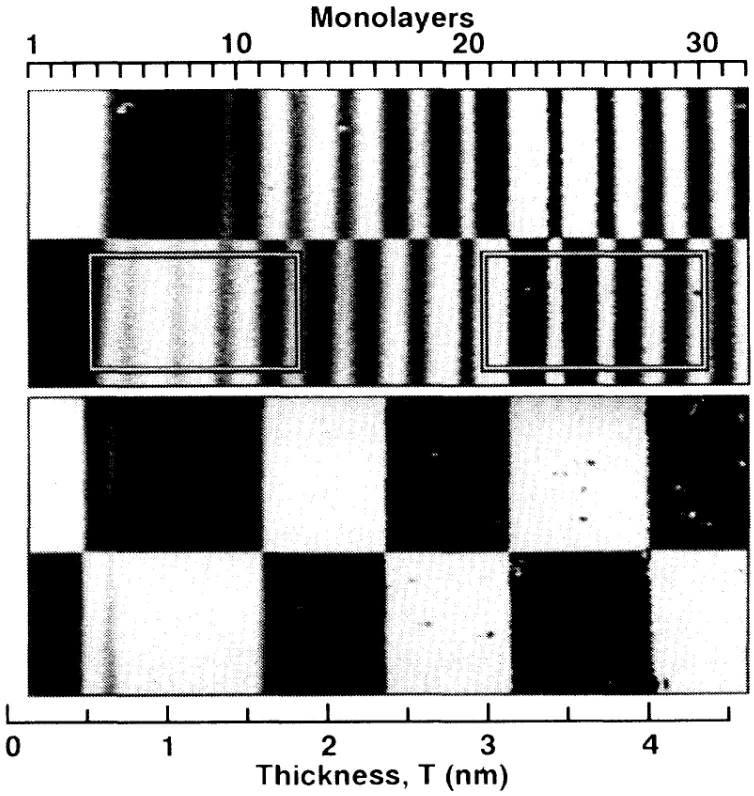

Figure 1. 6 The difference in the magnetic coupling of the Fe layers in an Fe/Cr/Fe sandwich for the Cr wedge grown on a Fe(001) substrate at room temperature (lower panel) and grown on a substrate at elevated temperature (upper panel) are obtained by scanning electron microscopy with polarization analysis. From the work of Unguris *et al.*[41]

Mn is an interesting AFM material because of its rich phase diagram with different ground states corresponding to the α (bcc), β (sc), γ (fcc), δ (bcc) phases.[61] Even small changes of the axial ratio *c*/*a* can induce dramatic changes in the interface coupling. In epitaxial Fe/bct-Mn/Fe (bct: body-centered tetragonal, α phase), the coupling angle between the magnetization directions of the two ferromagnetic Fe layers increases from 0° to 180° and then reduces to 90° with a 2 ML Mn oscillation period.[62] For the [Co/Mn] multilayer case, Kai has calculated that the interlayer exchange coupling both in [Co/α-Mn] and [Co/γ-Mn] multilayers shows oscillations with a period of 2 ML because of the antiferromagnetic order of the Mn layer, while the strength of the interlayer coupling in Co/α-Mn was found weaker than in Co/γ-Mn, which was interpreted as being due to the expanded *d*-band width and the AFM exchange interaction at the interface.[39] However, no such oscillations with two ML period have been observed in Co/γ-Mn multilayers,[63] and no clear antiferromagnetic coupling between Co layers could be observed in contracted fct Mn/Co multilayers.[64] In Co/Mn/Co on GaAs(001), only one Mn thickness regime with antiferromagnetic interlayer coupling could be observed.[65]

In this thesis, a detailed study of tuning the magnetic interlayer coupling in single-crystalline epitaxial Co/e-fct Mn/Co trilayers on Cu(001) is presented. Thanks to the layer-by-layer growth of both the bottom Co FM layer as well as the Mn AFM layer, the interface roughness can be selected with atomic precision. We show that in this system all three interlayer coupling mechanisms, RKKY-type indirect exchange with long-period oscillatory behavior, direct exchange through the AFM layer with an oscillation period of 2 ML of the AFM layer thickness, corresponding to a reversal of the coupling direction with an odd/even number of AFM atomic layers, and magnetostatic Néel-type interlayer coupling are present. The coercivity of minor loops of the top FM layer exhibits clear oscillations with a periodicity of 1 ML Mn thickness, which can be assigned to roughness oscillations at the upper Co/Mn interface. The maxima of the strength of the interlayer coupling due to direct exchange coupling correlate with the maxima of the coercivity. The interplay of the interlayer coupling together with the exchange bias effect leads to an oscillation of the apparent exchange bias of the top FM layer. Our results demonstrate that the Mn layer thickness as well as the atomic-scale roughnesses of the two interfaces can be used to tailor the magnetic interlayer coupling as well as the coercivities of the FM layers in such FM/AFM/FM trilayers.

1.3 Magnetization dynamics of coupled magnetic layers

The performance of data storage devices depends on how fast the magnetization can be switched. For example, storing the information in opposite magnetization directions (“0” and “1”) of a magnetic material, the writing is limited by how fast the magnetic element can be switched. Therefore the challenge of manipulating the dynamic properties of magnetic films or structures has attracted much attention. Generally, the ultrafast laser-induced demagnetization process shows three steps: i), the femtosecond demagnetization, ii), the picosecond recovery, iii), the hundred picoseconds –nanosecond magnetization precession.

In 1996 Beaurepaire *et al.*[66] were the first to employ 60 fs laser pulses to measure nickel thin films by using pump-probe time-resolved magneto-optical Kerr effect, as shown in Figure 1. 7. A reduced remanence was observed within the first picosecond. This behavior was later confirmed by magnetic second harmonic generation[67] and photoemission spectroscopy.[68] Demagnetization at the same order of time scale was also found on Co/Cu(001).[69] A study on Cu/Ni/Cu demonstrated that within the initial few hundreds of fs the dynamical evolution of the Kerr ellipticity and rotation can be affected by state filling effects.[70] Laser-induced magnetization precession and spin waves in canted ferromagnetic thin films were demonstrated in Ref. 71. A phase transition from antiferromagnetic to ferromagnetic was observed on the sub-picosecond time scale.[72,73] The laser-induced demagnetization also can be accompanied by a magnetization reversal.[74-76]

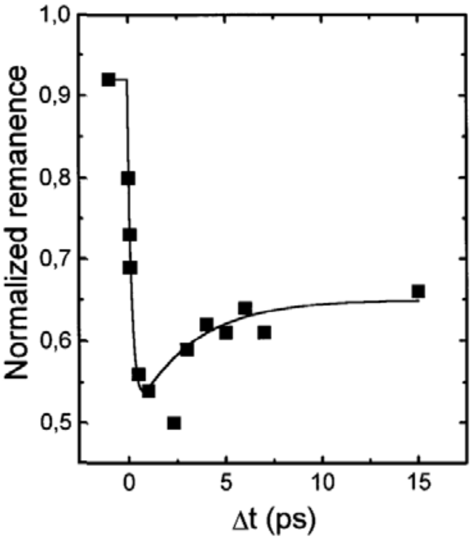

Figure 1. 7 Time-resolved magneto-optic signal from a remanently magnetized polycrystalline Ni film of 20 nm thickness on MgF_2. From the work of Beaurepaire *et al.*[66]

Several phenomenological models used to describe the ultrafast magnetization dynamics: the Langevin dynamics based on the Landau-Lifshitz-Gilbert (LLG) equation and classical Heisenberg Hamiltonian for localized atomic spin moments,[77] Landau-Lifshitz-Bloch micromagnetics,[78] and Koopmans's magnetization dynamics model (M3TM).[79] This thesis mainly focuses on the magnetization recovery process, so we only describe the LLG equation here:[80]

$$\frac{\partial \mathbf{M}}{\partial t} = \gamma \mathbf{M} \times \mathbf{H}_{\text{eff}} + \frac{\alpha}{\mathrm{M}_s} \mathbf{M} \times \frac{\partial \mathbf{M}}{\partial t}$$

where $\mathbf{M}$ is the magnetization, $\mathbf{H}_{\text{eff}}$ the effective field including the exchange, anisotropy, demagnetization, and the external field, M_s the saturation magnetization, γ the gyromagnetic ratio, and α the Gilbert damping coefficient. This equation can be used to resolve the dynamics of magnetic structures after a perturbation. Laser heating can induce a perturbation to change $\mathbf{H}_{\text{eff}}$, by changing magnetization, anisotropy, or coupling. The LLG equation with Langevin dynamics can be used in the atomistic limit to calculate the evolution of the magnetization, which describes the ultrafast magnetization processes.[77] One of the limitations of the LLG equation concerns time scale shorter than the time scale of spin-orbit coupling, then the description with a single gyromagnetic ratio fails and spin and orbital contributions must be considered separately.[81]

Chapter 2 Experimental details

In this Chapter, we will present details of the sample preparation and measurement techniques, which were carried out under ultra-high vacuum (UHV) conditions with a pressure of ~ 10^{-10} mbar: Auger electron spectroscopy (AES), low energy electron diffraction (LEED), medium energy electron diffraction (MEED), X-ray magnetic circular dichroism photoelectron emission microscopy (XMCD-PEEM), and magneto-optical Kerr effect (MOKE).

2.1 Surface techniques

All the experiments were performed under UHV conditions. A Cu(001) single crystal was used to grow the films. In order to obtain a clean and smooth surface the crystal was cleaned by Ar^+ ion bombardment and subsequent heating to about 830 K. Before annealing the sample was checked by AES. The AES uses the Auger effect to determine the cleanliness of a sample and also to determine the composition of a prepared alloy in surface physics experiments. Auger electrons are emitted from atoms during relaxation of the core level holes. The energy of Auger electrons is determined by the electronic structure of the elements which is unique for each element so that the Auger electrons give the fingerprints of all the elements except H and He.[82] A Φ 10-155 (Cylindrical-Auger Electron Optics) AES system was employed for the AES measurements. After each sputtering cycle, the AES spectrum obtained from the Cu(001) surface, which contains three prominent peaks of the Cu *LMM* Auger transitions at 778 eV, 848 eV, and 920 eV is inspected. If there are no other peaks from oxygen or other materials, the annealing of the clean crystal was started.

Then the sample has been checked by LEED, which is the principal technique for the determination of surface structures.[83] The LEED experiment uses a beam of electrons of low kinetic energy (~ 50-200 eV) incident normally to sample. The elastically backscattered electrons produce a diffraction pattern on a fluorescent screen. Then the LEED images were recorded on a computer via a CCD camera. An example of the diffraction pattern of the Cu(001) clean substrate for 69.8 eV electron energy is presented in Figure 2. 1. The vertical lattice constant of the sample can be studied via LEED/I(V), in which the intensity of the specularly diffracted beam (00 spot) is recorded as a function of the primary energy of the electrons. The kinematic analysis of the vertical interlayer distance is based on the approximation that only single scattering processes occur. We will show these results later.

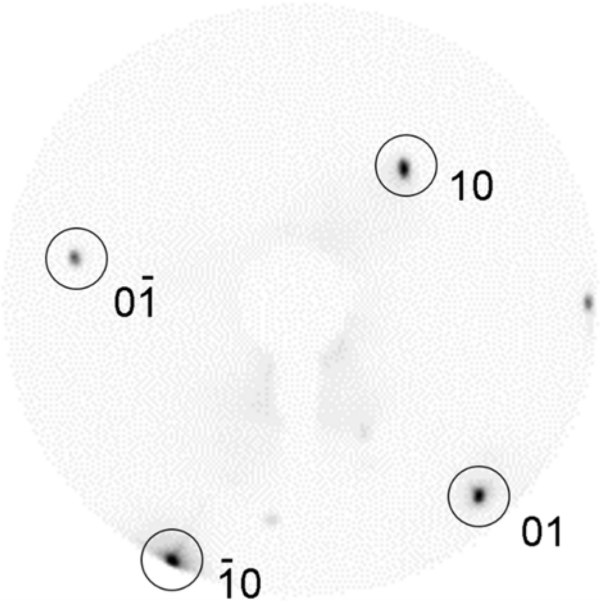

Figure 2. 1 LEED pattern of the Cu(001) substrate for 69.8 eV. Black circles indicate the (01) spots.

The films were grown on the clean substrate by e-beam assisted thermal evaporation. The electron beam from a hot filament is focused on the tip of a rod of the material to be deposited that is on a high positive voltage. The growth rate of the film was controlled by the power of the electron beam on the rod and monitored by the oscillations in the (00) spot MEED intensity recorded during evaporation. The sample is mounted on the manipulator in the center of the chamber, while the Auger electron gun and the LEED screen are facing each other. This allows using electrons from the AES system with a primary kinetic energy of 2 keV in a grazing incidence geometry in connection with the fluorescent screen of the LEED system to do the diffraction experiments. Figure 2. 2 shows the MEED oscillation curve for the growth of Co on Cu(001). The (00) spot intensity is plotted as a function of time. The first drop in intensity of the curve at time zero corresponds to the opening of the shutter. The MEED intensity displays an oscillatory behavior for layer-by-layer growth of the film, where it is assumed that the maxima in the intensity correspond to a filled topmost atomic layer. The amplitude of the oscillation decreases with increasing Co thickness, and above 16 ML Co thickness the oscillation is not visible any more, indicating a rougher surface.

Thanks to the layer-by-layer growth, the interface roughness on the atomic scale can be modified by tuning the thickness of the film to achieve a certain filling of the topmost atomic layer. These results will be presented later.

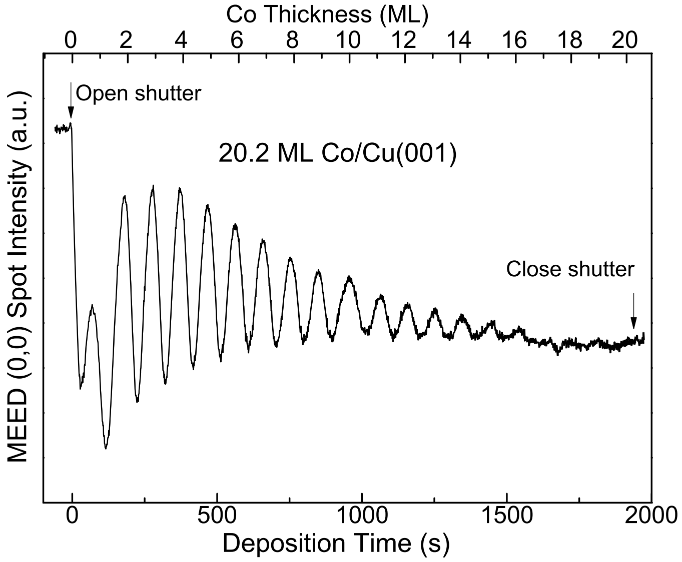

Figure 2. 2 MEED intensity of the (00) spot recorded during the deposition of 20.2 ML Co on Cu(001) at RT.

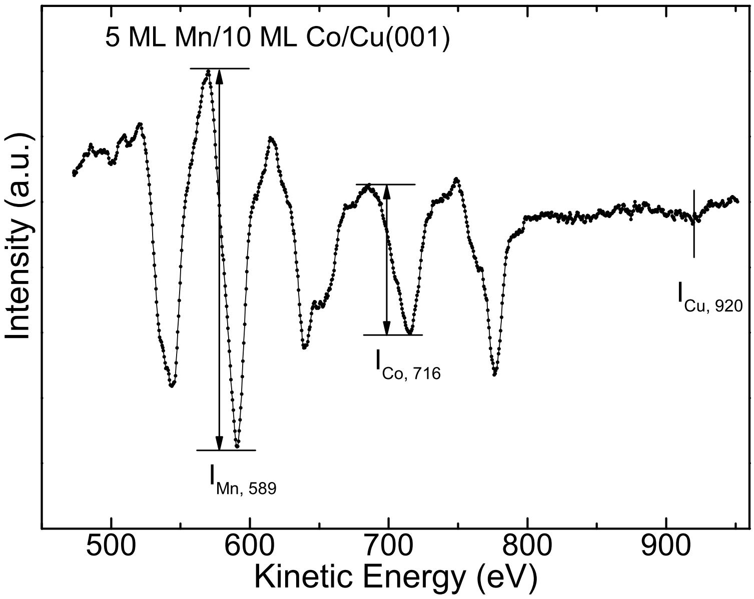

Figure 2. 3 AES result of 5 ML Mn/10 ML Co/Cu(001). Labels indicate the intensity of Mn, Co, and Cu, which are used for estimation the thickness of film.

By counting the oscillations in the MEED result, one can extract the thickness of the film, however, when we prepare a wedged sample, the sample is moving during deposition. In this case, AES was used to estimate the thickness of film. In the general case of a film (F) grown on a substrate (S) in a layer-by-layer mode, the Auger intensity of the substrate and the film of thickness d_F can be expressed as below, with the approximation that the attenuation of the Auger electrons within a material is determined by the mean distance the electrons can travel before an inelastic scattering event occurs.

$$I_S = I_0 S_S e^{-d_F/\lambda_S}$$

$$I_F = I_0 S_F (1 - e^{-d_F/\lambda_S})$$

here the subscripts S and F indicate substrate and film, respectively. The quantities S_i (i = S, F) are the sensitivities of the Auger transition, the λ_i are effective attenuation lengths of the Auger electrons from the respective materials, and I_0 is the intensity of the primary beam. The intensities I_S and I_F can be evaluated from the Auger spectrum, and the parameters S_i and λ_i can be determined once the thickness of the film is known from the MEED curves. Once S_i and λ_I are obtained, the film of thickness can be estimated from above equations in the case no MEED data are available.

Ni/Cu(001)		
AES peak	λ	S
Ni_{718}	4.2	0.3
Cu_{920}	4.8	0.9688
Co/Cu(001)		
AES peak	λ	S_{Cu}/S_{Co}
Co_{656}	3.5	2.27
Cu_{920}	5.45	
Mn/Co(001)		
AES peak	λ (λ′)	S
Mn_{589}	2.61	0.48
Co_{717}	4.1 (3.8)	0.71

Table 2. 1 Parameters of sensitivity of the Auger transition, S, and effective attenuation lengths of the Auger electrons from the respective materials, λ, are used to evaluate the thickness of films.

For the Mn wedge/10 ML Co/Cu(001) films, Figure 2. 3 presents the measured AES results. By using the equation

$$\frac{I_{Co}}{I_{Mn}} = \frac{S_{Co}}{S_{Mn}} \frac{(1 - e^{-d_{Co}/\lambda_{Co}})e^{-d_{Mn}/\lambda'_{Co}}}{(1 - e^{-d_{Mn}/\lambda_{Mn}})}$$

and knowing the values of S_i and λ_i, we estimate the thickness of the top Mn layer to 5 ML. λ'_{Co} is the correctional value of λ_{Co}, which has taken the factor of different interlayer distances for different films into account.

2.2 XMCD-PEEM

X-ray magnetic circular dichroism combined with photoelectron emission microscopy (XMCD-PEEM) is a powerful tool to image magnetic domains in magnetic layered systems. XMCD is the difference of absorption intensities upon changing either the helicity of polarized X rays or the magnetization direction of the sample. The X-ray absorption spectra (XAS) of ferromagnets are governed by resonances that occur if core electrons are excited into unoccupied 3*d* valence states above the Fermi level. In a ferromagnet, the density of unoccupied states is different for electrons of spin parallel or antiparallel to the magnetization direction, leading to a spin magnetic moment defined by the difference in occupation. This difference in the unoccupied states induces a different probability for the *p*→*d* transition excited by oppositely circularly polarized light. If the magnetization and light incidence are parallel to each other, there are more transitions possible, and vice versa. Figure 2. 4 shows as an example the magnetic circular dichroism spectrum of Co films. Figure 2. 4 (a) presents the X-ray absorption spectra for parallel (solid line) and antiparallel (dashed line) orientation of X-ray and sample magnetization direction. Figure 2. 4 (b) shows the dichroism spectrum calculated as the difference in absorption for opposite light helicity. The dichroism at the L_3 and L_2 edges has the opposite sign, this is due to the opposite sign of the spin polarization of the electrons excited from the two spin-orbit split levels ($2p_{3/2}$→3d, $2p_{1/2}$→3d).

In this study an Elmitec PEEM installed on beamline UE49-PGM-A of the synchrotron radiation facility BESSY II in Berlin has been used to investigate the domain structures. The X rays hit the sample under a 17° grazing angle from the sample surface. The emitted low energy electrons (energy up to 10 eV) are accelerated by applying -20 kV electric field to maintain their local information. These fast electrons are passed through several lenses, and are detected by a multichannel plate and then imaged with a CCD camera. Figure 2. 5 shows an example for 15 ML Co/15 ML Ni film grown on Cu(001). Panels (a) and (b) are the images obtained at the L_3 edge of Co for positive and negative helicity, respectively. The field of view is 25 μm and each image was exposed for about 5 minutes. In order to get the magnetic contrast and to eliminate topological information, the asymmetry is calculated as shown in Figure 2. 5 (c).

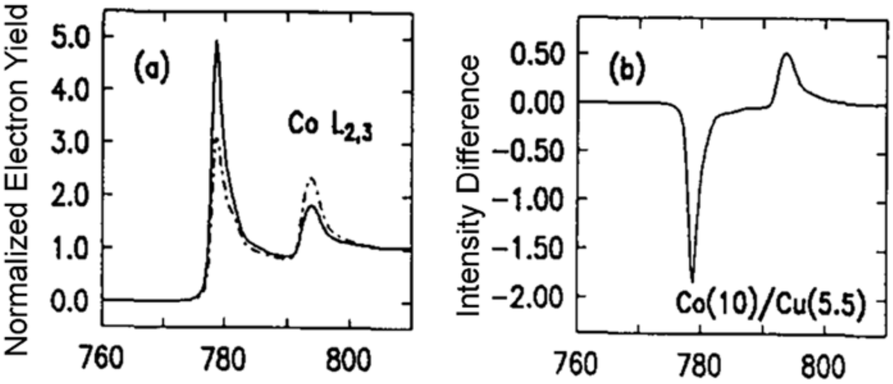

Figure 2. 4 (a) Co $L_{2,3}$ X-ray absorption spectra for Co (10 Å)/Cu(5.5 Å) recorded with parallel (solid line) and antiparallel (dashed line) alignment of photon spin and sample magnetization directions and (b) the difference spectrum. From the work of Stohr *et al*.[84]

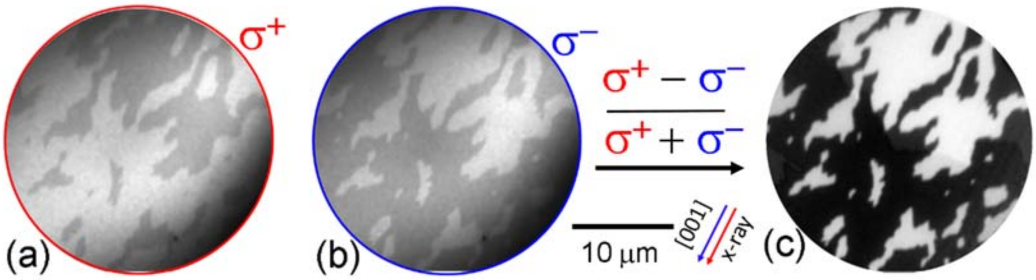

Figure 2. 5 (a, b) Two PEEM images obtained at the L_3 absorption edge of Co for opposite helicity and (c) the XMCD asymmetry image of 15 ML Co/15 ML Ni/Cu(001).

The experiments were performed in an ultrahigh vacuum chamber. The Cu(001) crystal was mounted on the Elmitec sample holder with [001] direction parallel to the sample transfer direction, which means that the [001] crystal direction is parallel to the incoming X rays [Figure 2. 6 (b, c)]. If not mentioned otherwise, XMCD images are obtained with [001] crystal direction parallel to X rays. The sample preparation is similar to Co/Mn/Co system in the MOKE2 chamber (sec. 2.4). Here shutter and sample were fixed during deposition, while the wedged layer is formed in the half shadow of the shutter [Figure 2. 6 (a)]. Figure 2. 6 (b) shows the Co/$Fe_{36}Mn_{64}$ wedged/Cu(001) films, i.e., the left dark side is the 8 ML Co/20 ML $Fe_{36}Mn_{64}$ bilayer and the right bright side is only the 8 ML Co film on Cu(001). The direction of the wedge can be chosen by rotating the shutter before deposition.

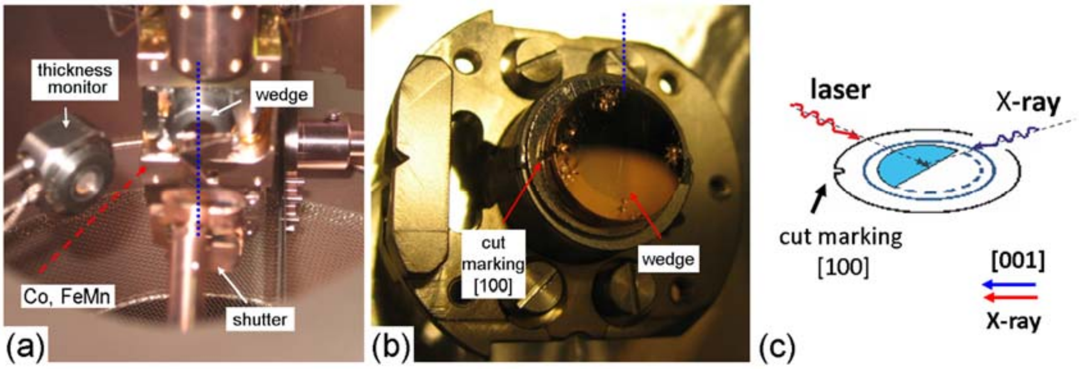

Figure 2. 6 (a) The sketch for the sample preparation in the PEEM chamber. (b) The Cu(001) crystal mounted on the sample holder with the [100] crystal direction parallel to the azimuth of the incoming X rays. (c) The coordinate axis for sample, incoming X rays, and laser.

To measure the magnetization dynamics we use XMCD-PEEM in a stroboscopic pump-probe scheme as shown in Figure 2. 7. The pump laser (Ti:Sa 800 nm, FWHM 80 fs) operates at 5 MHz and is synchronized to the 500 MHz master oscillator of the storage ring. The probe pulse is an X-ray pulse (FWHM 50 ps) using the single bunch mode (1.25 MHz). A computer-controlled trombone allows varying the pump-probe delay in fine time steps within 2 ns, which in combination with the shift in multiples of 2 ns in the synchronization, allows to get arbitrary long delays.

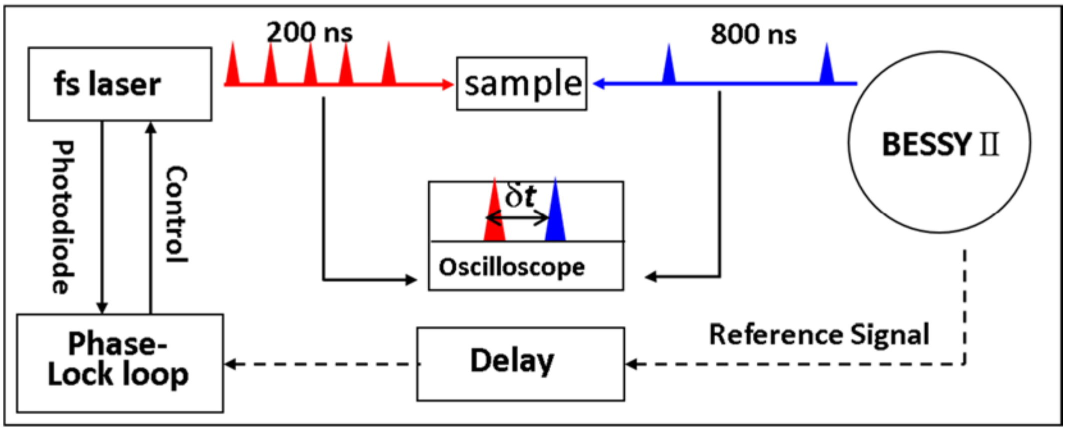

Figure 2. 7 Sketch of the pump-probe setup showing the laser used to generate the pump pulses and the storage ring in single-bunch mode generating the X-ray probe pulses.

2.3 Magneto-optical Kerr effect (MOKE)

Magneto-optical Kerr effect is an interaction between magnetic field and light. However, early searches were first conducted to find the interaction of light with electrical fields. It was believed that the effect of electrical fields should be stronger than that of magnetic fields. Even Michael Faraday's original research was focused on the relation between light and electricity. Until 1845, he verified that the effect of the magnet was to rotate the polarization plane of the transmitted light by an angle that depended on the strength of the magnet. Rev. John Kerr discovered MOKE in 1877 when he was examining the polarization of light reflected from a polished electromagnet pole.[85,86] In 1898, Kerr was presented the Royal Medal, and the presenter said, it was a wonder that Kerr learned so much with the "comparatively simple and ineffectual apparatus at his disposal". Kerr responded, "simple it may be, but not ineffectual; rude, but not crude".[87] This statement represents the simple nature of the technique. 1985 the first experimental application of MOKE to surface magnetism was the study of epitaxially grown ultrathin Fe films on an Au(001) single crystalline substrate.[88,89] Hysteresis loops were successfully obtained as a function of Fe thickness in the atomic layer range, which can be as thin as one atomic layer. J. Zak *et al.* reported Kerr rotation angle and Kerr ellipticity of a multilayer system, and found that the Kerr rotation signal is proportional to the magnetization times film thickness for thicknesses < ~ 10 nm.[90] Besides its scientific importance and high sensitivity to the magnetization within the skin depth region, also the simplicity is another main reason that this technique has been widely used in the field of low-dimensional magnetism.

Magneto-optics is either described in the context of macroscopic dielectric theory or microscopic quantum theory[91]. Macroscopically, magneto-optic effects arise from the antisymmetric, off-diagonal elements in the dielectric tensor. Maxwell[92] expressed linearly polarized light as a combination of the left- and right-circularly polarized components, and the Faraday effect is due to the different propagating velocities of these two circular modes. Microscopically, as a beam of light propagates through a medium, the electric field of the light generates motions of the electrons in the medium. The electrons will perform a left- or right-circular motion with the same radius induced by the left- or right-circular polarized electric field without external magnetic field. If an external magnetic field exists along the propagation direction of the electromagnetic wave, there will be an additional Lorentz force acting on each electron. The radius for left- and right-circular motion will be different, and this will lead to correspondingly different dielectric constants. Quantum descriptions of the magneto-optic effect have focused on the explanation of the larger magneto-optic effect in ferromagnetic materials. In 1932, Hulme pointed out that the spin-orbit interaction that couples the electron spin to its motion gives rise to the large Faraday rotation in ferromagnetic materials[93]. Spin-orbit coupling, $\sim (\nabla V \times \mathbf{p})\,\mathbf{s}$, results from the interaction of the electron spin with the magnetic field the electron ‘‘sees’’ as it moves through the electric field $-\nabla V$ with momentum **p** inside a medium. This interaction couples the magnetic moment of the electron with its motion, thus, connecting the magnetic and optical properties of a ferromagnet. Kittel[94] showed the change of the wave functions due to spin-orbit interaction and later Argyres[95] gave a full derivation of the magneto-optic effect in a ferromagnet using perturbation theory.

MOKE has some advantages for measurements of magnetic properties. First, high sensitivity even for atomic layer thickness of magnetic systems. Second, *in-situ* MOKE can be mounted inside a UHV chamber, such that the sample can be measured without capping layer, which could induce different magnetic properties. Third, the diameter of the laser spot is in the mm range and this can be used to focus on different thicknesses or compositions of a film on the same substrates. Fourth, the sample is not damaged by MOKE measurements.

The magnetic property of FM/AFM/FM films is mainly studied by using MOKE in this thesis. The MOKE set up in our MOKE2 chamber will be presented in sec. 2.4.2, here we describe the principle of MOKE.

Three geometries for MOKE measurements are shown Figure 2. 8: (a) polar, (b) longitudinal, and (c) transverse, respectively. These arise from the direction of the magnetic field with respect to the plane of incidence and the sample surface.

For polar MOKE [Figure 2. 8 (a)], the magnetization is normal to the sample surface and parallel to the plane of incidence. The signal intensity increases with decreasing incidence angle, and is maximum at normal incidence. The polar geometry is the only one where MOKE can be observed at normal incidence.

For longitudinal MOKE [Figure 2. 8 (b)], the magnetization is in-plane and parallel to the plane of incidence. The signal intensity decreases with decreasing incidence angle. Generally, the intensity of the longitudinal signal is around one order smaller than in the polar case, such that are needs to average over several field sweeps to get a better signal.

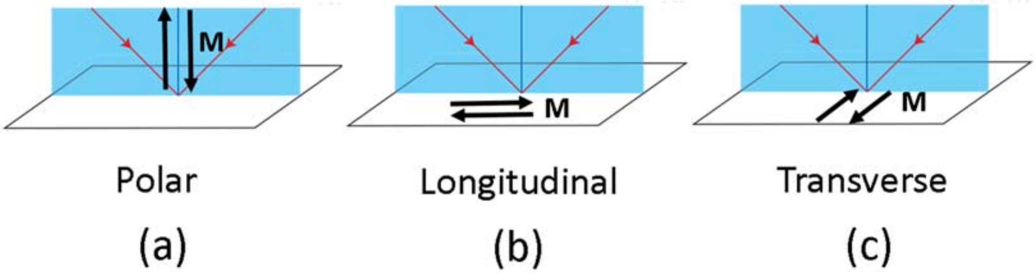

Figure 2. 8 Three geometries for MOKE: (a) polar, (b) longitudinal, and (c) transverse. The red and black arrows indicate the light path and the magnetization direction, respectively.

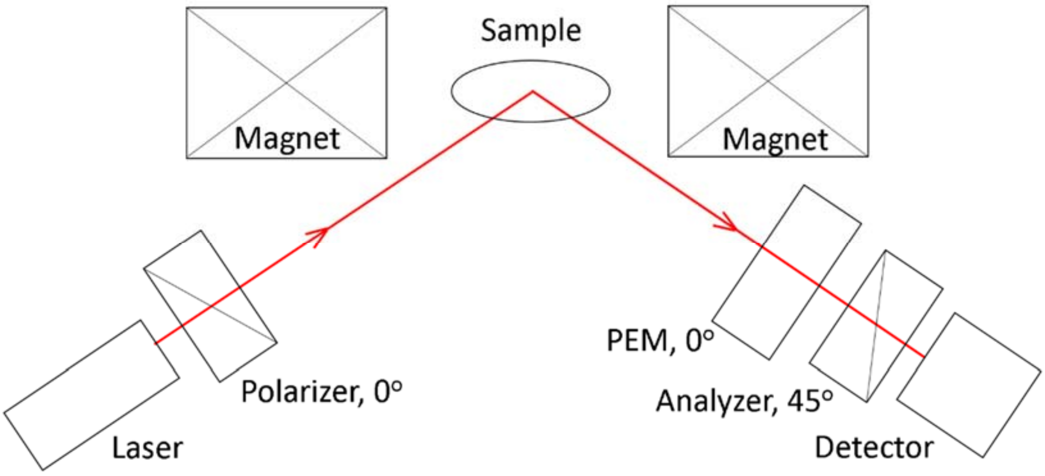

Figure 2. 9 Longitudinal geometry for MOKE. The laser beam first passes through the polarizer, reflects from the sample to the PEM, and after transmission through the analyzer is detected by the photodiode detector.

For transverse MOKE [Figure 2. 8 (c)], the magnetization is in-plane and normal to the plane of incidence. Only p-polarized light shows an effect, where the plane of polarization and the plane of incidence are parallel. In this case a small Kerr vector is generated which is parallel to the reflected polarization. Whether this increases or decreases the polarization amplitude depends on the direction of the magnetic field.[96]

The Kerr rotation angle and the Kerr ellipticity can be measured by AC or DC MOKE. A DC MOKE set up includes laser, two quasi-orthogonal polarizers, the sample, and a photodiode. The disadvantage of DC MOKE is that the signal intensity is influenced by the intensity of the laser and other sources of noise like vibration from the rotary vacuum pump. Using AC MOKE can avoid these influences. There are two types of AC MOKE, one is to modulate the laser intensity, the other to modulate the laser polarization. Figure 2. 9 shows the AC MOKE set up used in this thesis. Here a photoelastic modulator (PEM) is used. By modulating the polarization of the reflected light, the PEM allows one to determine the polarization of that light. The PEM consists of an isotropic optical element, which is kept in a longitudinal mode vibration at the element's natural frequency of $\omega =$ 50 kHz. The vibration is induced by a matched, piezoelectric quartz crystal transducer.

After passing through the analyzer to the photodiode, the signal is extracted by lock-in amplifiers. The intensity of light arriving at the photodiode can be written as:[96]

$$\mathrm{I}(t) = \mathrm{I}_0[1 + 2\theta_k \cos(A_0\omega t) - 2\varepsilon_k \sin(A_0\omega t)]$$

where I_0 represents the DC intensity, ω is the angular frequency of the PEM oscillations, and A_0 is the retardation amplitude of the PEM. Using a Fourier series expansion and neglecting some terms, one obtains[96]

$$\theta_k = \frac{\sqrt{2}}{4J_2}\frac{V_{2f}}{V_{DC}}$$

$$\varepsilon_k = \frac{\sqrt{2}}{4J_1}\frac{V_{1f}}{V_{DC}}$$

Where V_{DC}, V_{1f} and V_{2f} can be measured by voltmeter, 1f and 2f means 50 kHz and 100 kHz, J_1 and V_2 are the Fourier series, respectively.

2.4 Sample preparation

In this section, we will talk about the sample preparation and the MOKE measurements. All of the experiments except the XMCD-PEEM measurement are done in the MOKE2 vacuum chamber. The chamber was equipped with Ar^+ ion sputtering, annealing, three e-beam evaporators, AES, LEED, MEED, and MOKE in polar and longitudinal geometries. The sample is mounted on an Omicron sample holder attached to the manipulator which has four degrees of movement (x, y, z, and θ). The manipulator allows the movement of the sample ± 25 mm in the x- and y-direction, a vertical movement up to 400 mm, and polar rotation by 360°. The movement in the x, y, and polar direction can be manually performed while the z movements are possible manually as well as via a programmable stepper motor controller. The sample can be cooled by a liquid helium down to about 40 K, and heated by a resistive heater up to about 830 K.

The experiments were performed in an ultrahigh vacuum chamber with a base pressure of ~ 1×10^{-10} mbar. The Cu(001) single crystal of 10 mm diameter with < 0.1^{o} miscut was used as substrate for the growth of Co and Ni films. Cu(001) was cleaned by cycles of 1 keV Ar^{+} ion sputtering and annealing at 830 K for 20 minutes. Prior to deposition, the Cu(001) surface was checked by Auger electron spectroscopy and low-energy electron diffraction in order to make sure the sample clean.

Co, Ni, Mn films (Co, Ni, Mn rods: 99.99%) were deposited at a pressure lower than 2×10^{-10}, 2×10^{-10} and 4×10^{-10} mbar, respectively, by electron-beam-assisted thermal evaporation at room temperature. Typical deposition rates of Co, Ni, Mn were 0.5–1, ~ 1, and ~ 0.3 ML/min, respectively. Uniformity of the film thickness was checked by Auger electron spectroscopy (AES). Co and Ni were evaporated using two single Omicron EMF3 evaporators and Mn was evaporated using an Oxford instruments ENG4 evaporator. All of evaporators had a feedback control of the flux during deposition. The advantage for ENG4 is that the evaporation profile is much wider, which it’s useful to get uniform films. However, the disadvantage is that the target is fixed in position, so the rod should be refilled very often. Usually all four targets of this evaporator were filled only with Mn rods, and this will help to evaporate for a long time.

2.4.1 Wedge sample

Wedge-shaped Mn and Co layers were prepared by placing a shutter in front of the sample as shown in Figure 2. 10. The manipulator is moved by a computer-controlled stepper motor. Typical wedge slopes were 0.8–1.4 ML/mm, with a wedge size of 8 mm. Co, Ni, Mn thicknesses were calibrated by medium energy electron diffraction (MEED) intensity oscillations during growth and AES. The total error in the thickness calibration of the bottom Co and Ni layers is about 0.1 ML and 0.3 ML, respectively. For the Mn wedge, a systematic error of about 10% may be involved in the thickness determination for a certain position along the wedge, while the statistical error is smaller than 0.2 ML. Since the top Co and Ni layers do not grow in a layer-by-layer mode, its thickness is determined by the deposition time and the evaporation rate determined by MEED oscillations during the growth of the bottom Co and Ni layers. This yields an accuracy of about 10% for the top Co and Ni layer thickness. Structural properties were determined by LEED and MEED, the film thickness and composition by AES. The magnetic properties were characterized by longitudinal and polar MOKE.

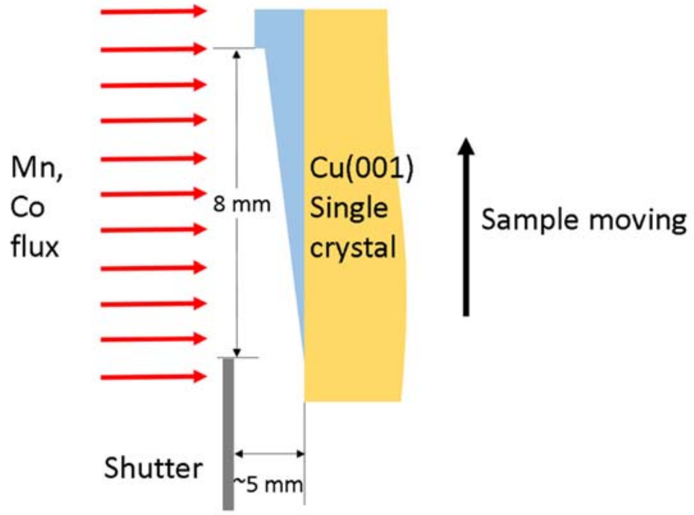

Figure 2. 10 Illustration of the growth of a Mn (Co) wedge using a shutter. The sample was moved by the stepper motor during deposition (not to scale). Usually the wedge size is 8 mm in 10 mm of crystal diameter, and the distance between the sample and the shutter is about 5 mm.

2.4.2 MOKE setup

In-situ magneto-optical Kerr effect (MOKE) measurements were performed in the polar and longitudinal configuration, with a maximum field of 150 mT at sample temperatures between 40 K and 400 K shown in Figure 2. 11. A photoelastic modulator and the lock-in technique was used, where the phase of the reflected light was modulated at a retardation of 1/4 of the wavelength. The diode laser (633 nm wavelength) was focused onto the sample with a beam size of around 0.2 mm. The Kerr ellipticity was measured along the [100] azimuth of the sample, and all of the MOKE signals were normalized to the DC intensity at the photodiode detector. All measurements were performed at RT. The bottom Co layer was magnetized in the negative field direction before deposition of the Mn layer. No field cooling procedure was applied.

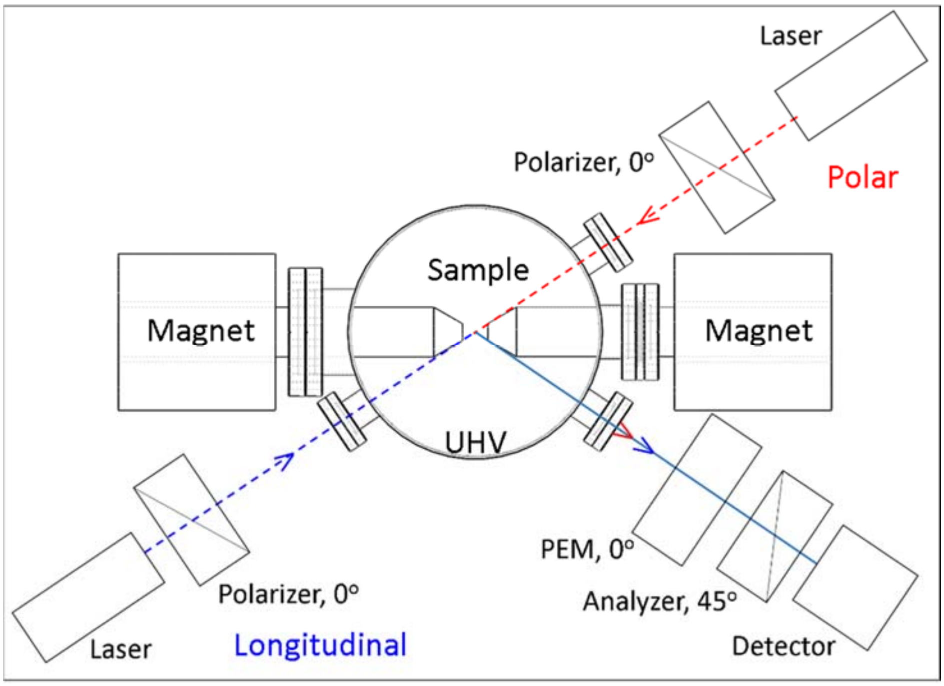

Figure 2. 11 MOKE setup for polar and longitudinal geometries in the vacuum chamber MOKE2.

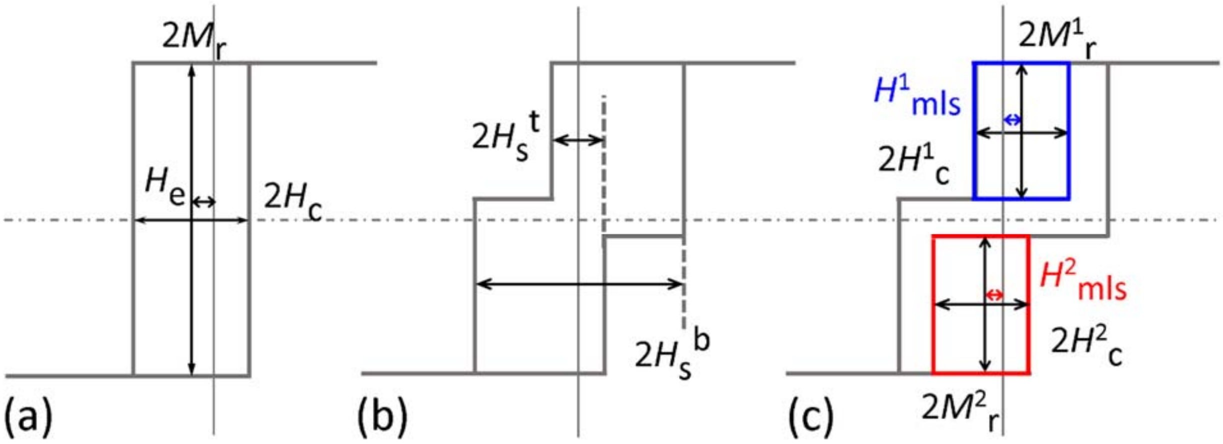

Figure 2. 12 The sketch of the MOKE loops. (a) Magnetization loop with one step, M_r remanent Kerr signal, H_c coercivity, and H_e exchange bias field. (b) Magnetization loop with two steps corresponding to a bottom FM layer with higher H_s^b and a top FM layer with lower H_s^t (here a bottom FM layer with higher coercivity is assumed). (c) H^1_c, H^2_c and M^1_r, M^2_r are the coercivity and remanent Kerr signal of the top FM layer in the positive and negative field minor loop measurements, respectively. $H^{1,2}_{mls}$ defines the shift of the minor loops with respect to zero field.

Figure 2. 12 shows the MOKE loops as analysed in this thesis. Figure 2. 12(a) presents a magnetization loop with one step, for example the signal of a single FM layer, Mn/FM bilayer, and the FM/Mn/FM trilayer with small spacer layer thickness. H_c, H_e, and M_r are used in the data analysis to describe the loop. Figure 2. 12(b) shows a typical magnetization loop for a trilayer

sample with a thick spacer layer, where two coercivites corresponding to the two FM layers are measured. Minor loops are used to estimate the interlayer coupling between two FM layers as shown in Figure 2. 12(c). $H^1{}_{\mathrm{c}}$, $H^1{}_{\mathrm{mls}}$, $M^1{}_{\mathrm{r}}$, and $H^2{}_{\mathrm{c}}$, $H^2{}_{\mathrm{mls}}$, $M^2{}_{\mathrm{r}}$ are the coercivity, minor loop shift, and remanent Kerr signal of the FM layer with lower coercivity in the positive and negative field minor loop measurements, respectively.

2.4.3 Modification of the vacuum chamber

Shutter: Wedged film were prepared by the shutter. For example, the AFM layer was grown into a wedged shape to permit the systematic study of the interlayer coupling as a function of spacer-layer thickness by scanning the laser spot on a single sample. The wedge sample is not only good for studying the interface roughness but also can save much time. Two shutters were mounted in the chamber, one horizontal and another vertical. Combining the horizontal shutter and moving the sample along the *z* direction, a wedged layer can be prepared (Figure 2. 10). Different depositions on the left or right half of the sample can be made by the vertical shutter.

Hall sensor, amplifier: The remanent magnetic field of the two cores of the electromagnet are really large, namely ~ 30 mT in the field range of ±150 mT. The values of the magnetic field are unreliable if just taken from the current through the coils. A Hall sensor (HE144P, Asensor technology AB, Sweden) was mounted in the chamber to measure the magnetic field online during the MOKE measurement. The HE144P has 4 pins of 0.4 mm width. Two of them are for the power input (constant current ~ 1 mA) and another two give the Hall voltage output. The four pins were contacted by a vacuum feedthrough. The Hall sensor was mounted in the center of one core, and the distance between the hall sensor and the sample (MOKE measurement position) is about 15 mm. The Hall voltage was calibrated by a gaussmeter in air. The amplifier for the Hall sensor was made by our electronic workshop, and helps to increase the range of the output Hall voltage and reduce the noise arising from temperature variations. Compared to measurements without Hall sensor, the magnetic field data in hysteresis loops was much enhanced using the Hall voltage. The only problem is that the Hall sensors sometimes just stopped working, such that we had to vent the chamber and mount a new one. Probably this is because the Hall sensor is designed in air, and not in ultra-high vacuum. The size of the pins and the distance between pins are very small (~ 0.5 mm), usually it took one day's work to spot-weld these to the feedthrough.

MOKE setup: This work was done with the help of Dr. Chii-Bin Wu. It included ordering the optical parts like laser, the quartz glass viewports, adjusting the lock-in amplifier, adjusting the geometry, connecting two bipolar operational power supplies (BOP, 20 A, 20 V) in series write out and so on.

Iron cores: This work was done with the help of Dr. Yin-Ming Chang. The previous cores had large remanent magnetic field and a smaller saturation field. Two new cores were made from pure iron. The advantages of the new design are: First, a smaller remanent magnetic field, namely < 3 mT in the test range of ±150 mT. Second, the maximum field at the sample is now should be above 200 mT instead of 150 mT in the previous cores. Third, one of the cores is fixed into the chamber, the other can be moved ±30 mm in order to increase the magnetic field at the sample further. Fourth, the outer diameter of the cores are fit to match the inter diameter of the existing Cu coils, which keeps the magnetic field at the sample constant independent of mounting and unmounting the coils, for example in order to bake the chamber.

Labview programs: The MOKE measurement program was written in Labview, which includes the interpolation, drift correction to obtain closed loops, and averaging functions. Other Labview programs are for AES measurements, PID control of the sample temperature, and stepper motor controller.

Chapter 3 Structure and magnetic properties of Co/Mn/Co trilayers

In this chapter, we present a full study of (Co/)/Mn/Co samples, in which the thickness of Mn and Co layers, temperature, and interface roughness were changed to study this system.

Section 3.1 shows the growth and structure of Mn/Co/Cu(001). A brief overview of the Mn thickness dependence for (Co/) wedged Mn/Co samples will be discussed in sec. 3.2. Details of different thickness of the Mn spacer layer will be presented in these sections: sec. 3.3 focuses on the behavior of the coercivity of the bottom Co film with filled and half-filled topmost atomic layers around the onset of AFM order of the Mn film. Decoupling and RKKY interlayer coupling are discussed in sec. 3.4. In sec. 3.5, the direct exchange coupling between the two Co layers will be investigated for different roughnesses of the AFM/FM interface. Results of wedged Co thickness in Co/Mn/Co trilayers will be presented in sec. 3.6. Part of this section is from the publication: J. Appl. Phys. **115**, 233915 (2014).

3.1 Growth and structure

Figure 3. 1(a) shows typical MEED oscillation curves for the growth of Co on Cu(001) and of Mn on Co/Cu(001). Both show clear periodic oscillations, indicative of layer-by-layer growth. For Mn on bottom Co film with filled layer, the amplitude of the oscillations decreases after the first two monolayers. This can be due to the evolution of the film structure during initial growth of Mn on Co/Cu(001), when Mn atoms fill the channels between Co islands and thus smoothen the surface. Subsequently, this surface forms the substrate for the almost perfect layer-by-layer growth of Mn, which starts from 2 ML thickness.[97,98] For the MEED curve of Mn growth on 10.3 ML Co/Cu(001) in Figure 3. 1(b), it is clearly seen that Mn first fills up the remaining 0.7 ML of the last Co layer and then continues to grow layer by layer with 1-ML oscillations.

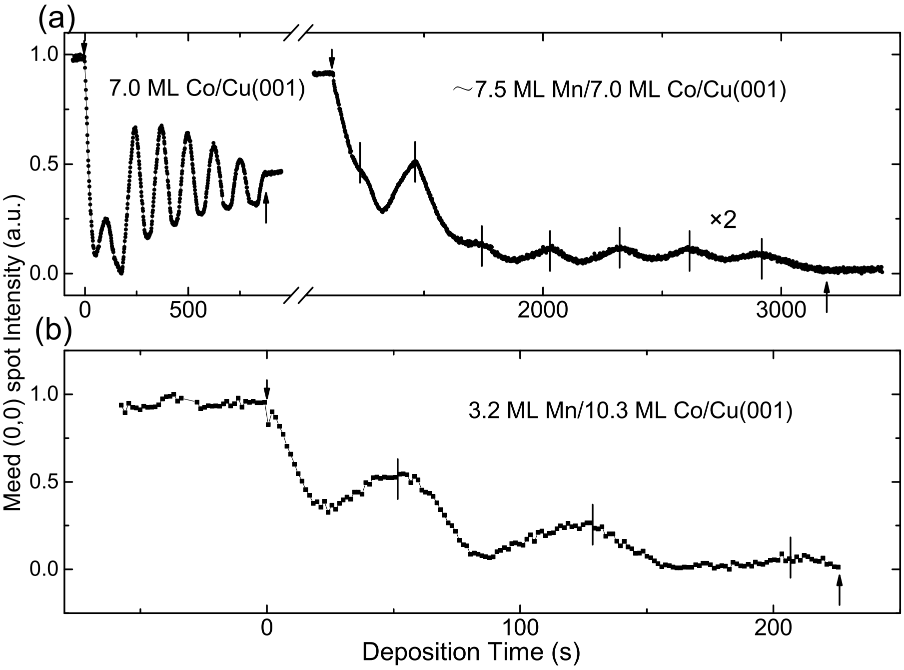

Figure 3. 1 MEED intensity of the (0 0) spot recorded during the deposition of Co on Cu(001) and Mn on Co/Cu(001) at RT. (a) 7.0 ML Co on Cu(001) and 7.5 ML Mn on 7.0 ML Co/Cu(001). (b) 3.2 ML Mn on 10.3 ML Co/Cu(001) at RT. Arrows indicate shutter opening and closing, for example by down arrows and up arrows, respectively.

Figure 3. 2 (a)–(c) show low-energy electron diffraction (LEED) patterns of Cu(001), 10.2 ML Co/Cu(001), and 7 ML Mn/10.2 ML Co/Cu(001), respectively. The spot positions are accordant in the above results, indicating the coherent growth of Mn/Co on Cu(001). LEED-I/V curves of the specular spot are recorded for the analysis of the interlayer distance *d*, as shown in Figure 3. 2 (d). The integer numbers denote the orders of the maxima in the Bragg condition for constructive interference. The values for *d* are labeled to the curves in Figure 3. 2 (d). The interlayer distance of Cu(001) is 1.83 Å, which is close to the bulk value of Cu of 1.805 Å. 10.2 ML Co/Cu(001) show a face-centered-tetragonal (fct) structure with d = 1.73 Å. A smaller d of 1.70 Å is observed for 3.2 ML Mn/10.3 ML Co/Cu(001), corresponding to an axial ratio $c/a = 0.93 \pm 0.01$. 7 ML Mn/10.2 ML Co/Cu(001) reveal a vertical lattice constant of 1.92 Å, corresponding to an axial ratio $c/a = 1.05 \pm 0.01$. a = 1.83 Å is used for calculating the axial ratio as we think that Co(001) is grown coherently on Cu(001), and to cancel out a possible systematic error. The axial ratio *c*/*a* of Mn on Co/Cu(001) changes from 0.93 to 1.05 with increasing Mn thickness, corresponding the phase transition of Mn from contracted to expanded fct structure. Such an expanded face-centered

tetragonal structure of Mn is consistent with theoretical calculations (c/a = 1.048[99]) and previous experimental work.[20,100,101] Concerning that comparison it should be noted that our sample temperature during preparation was RT, while it was 330 K in Ref. 20.

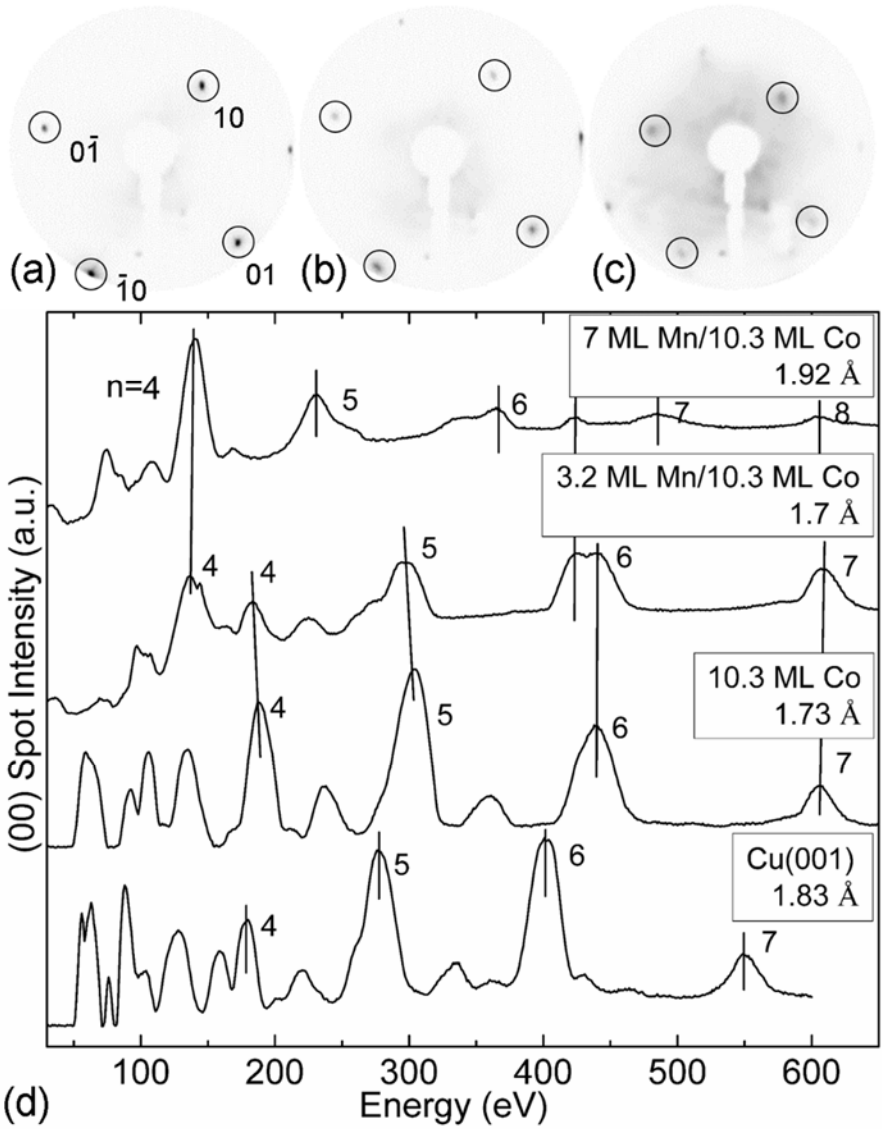

Figure 3. 2 LEED patterns of (a) Cu(001) (69.8 eV), (b) 10.2 ML Co/Cu(001) (70.2 eV), (c) 7 ML Mn/10.2 ML Co/Cu(001) (102.6 eV). (d) LEED-I/V curves of the (00) spot of 7 ML Mn/10.3 ML Co/Cu(001), 3.2 ML Mn/10.3 ML Co/Cu(001), 10.3 ML Co/Cu(001), and Cu(001). Numbers indicate the diffraction order of single-scattering peaks. The vertical layer distances resulting from a simple kinematic analysis are labeled to each curve.

3.2 Overview of the Co/wedged Mn/Co trilayers

In this section, we will give a brief introduction for the whole Mn thickness range of (Co/) wedged Mn/Co samples, and compare the results of integer and half-integer number of atomic layers in the bottom Co film. To avoid any effects related to a too high slopes of Mn thickness, two groups of samples (10.0 ML, 10.5 ML and 8.0 ML, 8.5 ML thickness of bottom Co layer) were prepared.

3.2.1 Magnetic properties of Co/Mn/ 10.0 ML, 10.5 ML Co

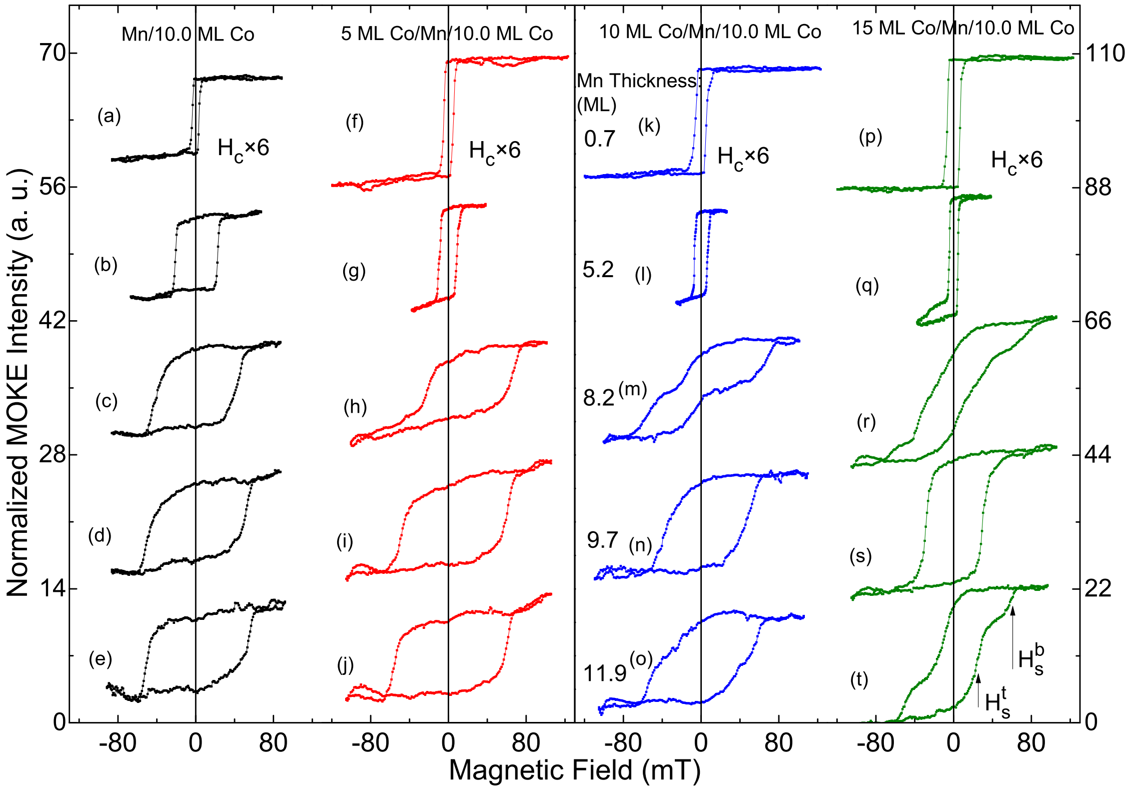

Figure 3. 3 Hysteresis loops measured with the magnetic field aligned parallel to the in-plane [100] crystal direction for Mn wedge/10.0 ML Co (a-e), 5 ML Co/Mn wedge/10.0 ML Co (f-j), 10 ML Co/Mn wedge/10.0 ML Co (k-o), 15 ML Co/Mn wedge/10.0 ML Co (p-t). H_s^t and H_s^b label the switching field of the top and the bottom layer, respectively. The Mn thickness is indicated in the middle of the figure.

Different thicknesses of the top Co layer in the trilayer samples were prepared in order to study the thickness dependence of the exchange bias and the interlayer interaction. Let us first look at the data of 10.0 ML thickness of bottom Co layer samples. (Due to the high coercivity of filled bottom

Co layer samples, the data of exchange bias field shows a large error bar, so we don't discuss about the H_e for the filled bottom Co layer sample in this section.)

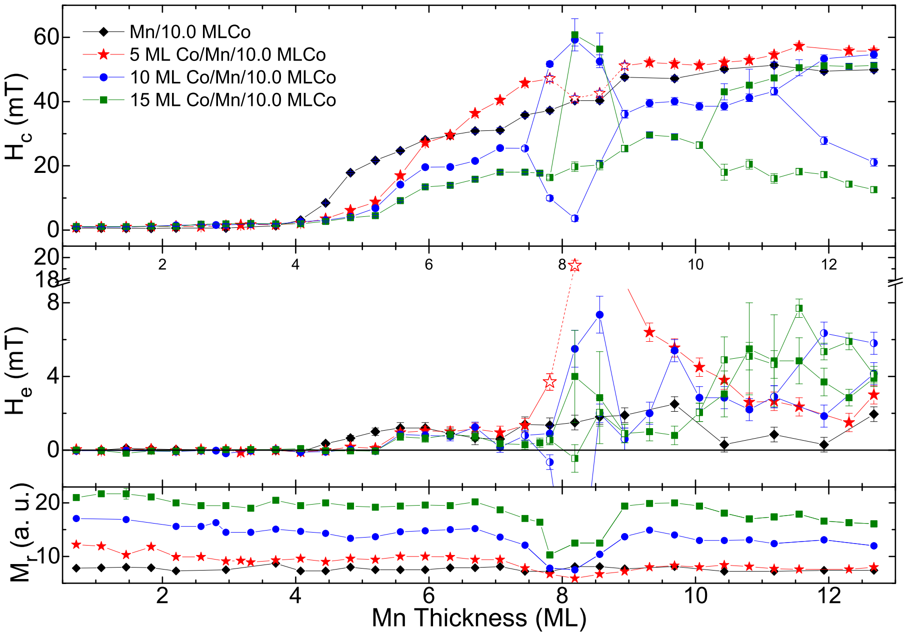

Figure 3. 4 Coercivity H_c (top) and exchange bias field H_e (middle) of 0 ML (black diamonds), 5 ML (red stars), 10 ML (blue circles) and 15 ML (green squares) Co/Mn-wedge/10.0 ML Co samples as a function of Mn thickness. At higher Mn thickness, two different switching fields [bottom Co layer with higher H_s^b, and top Co layer with lower H_s^t (half squares), respectively] are presented for the trilayer samples. Open stars indicate data extracted from minor loops. Bottom: Kerr signal in remanence of the same samples.

Figure 3. 3 shows normalized magnetic hysteresis loops of bilayer and trilayer samples, measured by longitudinal MOKE. The coercivity H_c, exchange bias field H_e, and the remanent Kerr signal M_r are plotted in Figure 3. 4 as a function of Mn thickness. For the bilayer system, square loops with low H_c start from zero Mn thickness and rise in width at around 4.3 ML Mn thickness indicating the onset of antiferromagnetic order in Mn at RT (t_{AFM} indicates the thickness of the onset of antiferromagnetic order). H_c with tilted loops continues to increase sharply until 6 ML, Mn thickness and then with a slower increase up to around 9 ML, after which it then stays about constant. M_r of the bilayer shows nearly constant values for all Mn thicknesses range.

We now turn to the trilayer systems. The loops and H_c show a similar behavior as the bilayer at Mn thicknesses before t_{AFM}. Different thicknesses of the top Co layer of the trilayers exhibit a similar t_{AFM} of around 5.2 ML Mn thickness, which is 0.9 ML thicker than in the bilayer case. Above t_{AFM}, the highest thickness of top Co layer displays the lowest H_c as shown in Figure 3. 3 (5.2 and 9.7 ML Mn thickness). Only the H_c of 5 ML Co/Mn/10 ML displays a higher value than the bilayer above 6 ML Mn thickness. This could be due to the thin top Co layer, which has a higher coercivity than the thick bottom Co layer. The loops at around 8.2 ML and higher Mn thickness look somewhat different. At 8.2 ML Mn thickness, the trilayers separate into two loops, and exhibit a reduced M_r (one part of the loop of the top 5 ML Co sample is missing because of the limited field). This could be due to an antiferromagnetic RKKY interaction. For higher thicknesses of Mn, decoupled loops were observed again in 10 ML and 15 ML Co/Mn/10.0 ML Co samples. It is clearly seen in Figure 3. 3(t) that the top Co layer has a lower coercivity H_s^t and the bottom Co layer has a higher coercivity H_s^b.

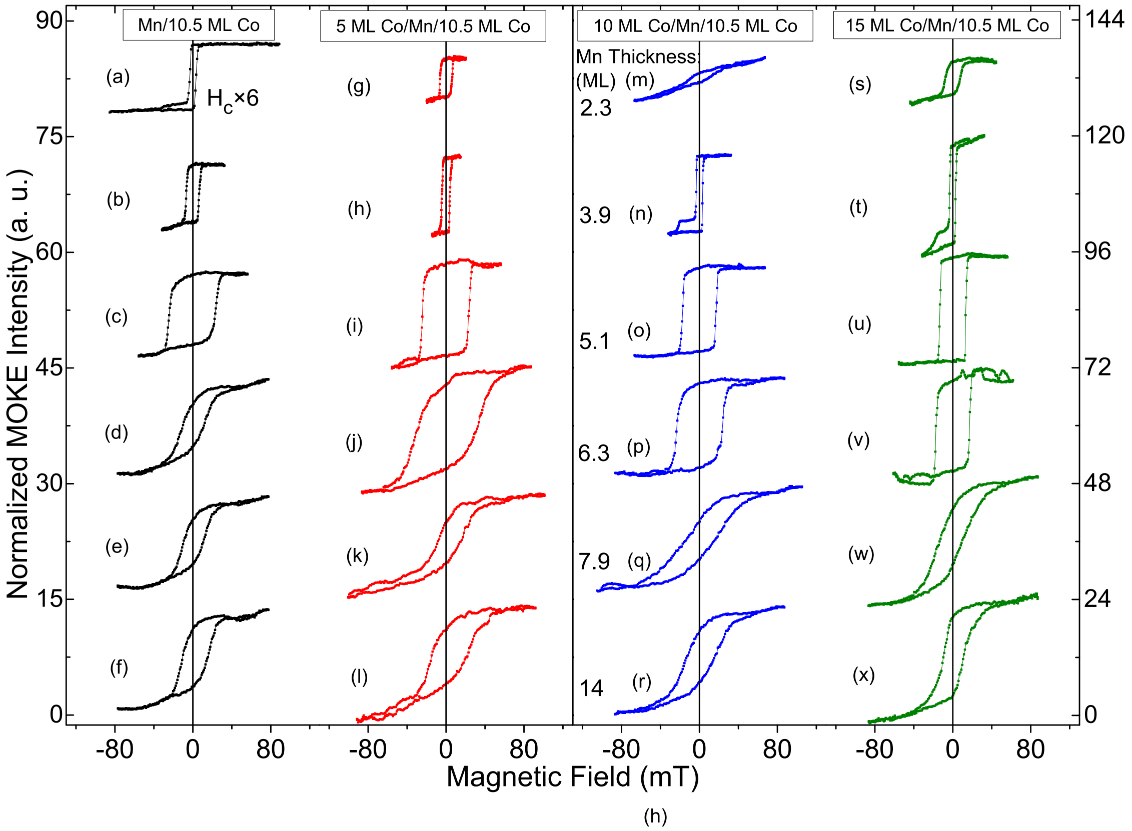

Figure 3. 5 Hysteresis loops measured with the magnetic field aligned parallel to the in-plane [100] crystal direction for Mn wedge/10.5 ML Co (a-f), 5 ML Co/Mn wedge/10.5 ML Co (g-l), 10 ML Co/Mn wedge/10.5 ML Co (m-r), 15 ML Co/Mn wedge/10.5 ML Co (s-x) with different thickness of Mn.

Now let us turn to the (Co/) Mn/10.5 ML Co samples. Normalized magnetic hysteresis loops of bilayer and trilayer samples and the coercivity H_c, exchange bias field H_e, and remanent Kerr signal M_r as a function of Mn thickness are presented in Figure 3. 5 and Figure 3. 6, respectively. Square loops with low H_c start from 1.9 ML Mn thickness. The coercivity then increases at around 3.4 ML (t_AFM) to reach a maximum (24 mT) at 5 ML Mn thickness (5.1 ML in Figure 3. 5). At higher Mn thicknesses, the H_c dramatically decreases to 10 mT at 7 ML Mn thickness. Above 6.7 ML Mn thickness, H_c is independent from the Mn thickness. The slight increase of H_c after 11 ML Mn thickness could be due to a small deviation of thickness in the bottom Co layer. The data of H_e vs Mn thickness, start to devicate from zero at around 6 ML Mn thickness, where H_c already decreases, H_e of the bilayer seems to assume a constant value (1 mT) up to 13 ML Mn thickness. The increase at higher Mn thickness could be due to the same reason at the increase of of H_c at that Mn thickness, namely a deviation of the thickness of the bottom Co layer.

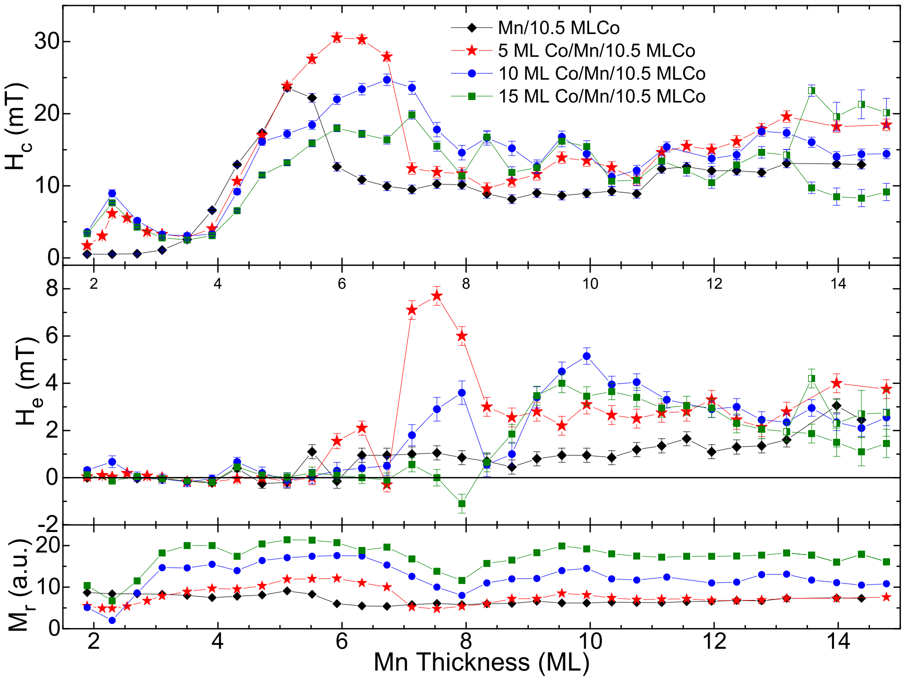

Figure 3. 6 Coercivity H_c (top) and exchange bias field H_e (middle) of 0 ML (black diamonds), 5 ML (red stars), 10 ML (blue circles) and 15 ML (green squares) Co/Mn-wedge/10 ML Co trilayer (bilayer) sample as a function of Mn thickness. For the higher Mn thickness, two different switching fields (bottom Co with higher H_s^b, and top Co with lower H_s^t, respectively) are presented for the trilayer samples. Bottom: Kerr signal in remanence of the same samples.

Compared to the bilayer sample, the trilayers present a different behavior. At around 2.3 ML [(g, m, s) in Figure 3. 5], tilted loops are observed with larger H_c and reduced M_r. The t_AFM of the trilayers is around 3.9 ML Mn thickness similar to the bilayer. H_c maxima of 5 ML (31 mT), 10 ML (25 mT), 15 ML Co/Mn/10.5 ML Co (20 mT) are located at 5.9 ML, 6.7 ML, 7.1 ML Mn thickness, respectively. It seems that the maxima shift to higher Mn thickness with increasing top Co layer thickness. After the maxima, H_c of the trilayer is slightly higher than that of the bilayer. From the reduced M_r at around 8 ML Mn thickness and the data from the trilayer with 10.0 ML thickness of the bottom Co layer, the second antiferromagnetic RKKY maximum could exist in this thickness range, however, the loops do not show a clear antiparallel alignment of the two Co layers (7.9 ML in Figure 3. 5). Above 8 ML Mn thickness, H_c of the 10 ML and 15 ML Co/Mn/10.5 ML Co samples exhibits a weak oscillation with a period of about 1 ML. This could be due to the interface coupling at the top Co/Mn interface induced by the layer-by-layer growth of Mn on Co/Cu(001).

Because of one part of the loop is missing at around 8 ML, the exchange bias field H_e of the trilayers is unreliable in this thickness range. It is difficult to get the starting thickness of H_e for the trilayers. After 9 ML, though the data for H_e should be reliable. The value of H_e of the trilayers are higher than that of the bilayer up to 13 ML Mn thickness. At higher thicknesses, H_e shows different behavior should be due to the different thickness in the bottom Co layer. The details of H_e for the bilayer and the trilayer will be discussed in sec. 3.2.3.

3.2.2 Magnetic properties of Co/Mn/ 8.0 ML, 8.5 ML Co

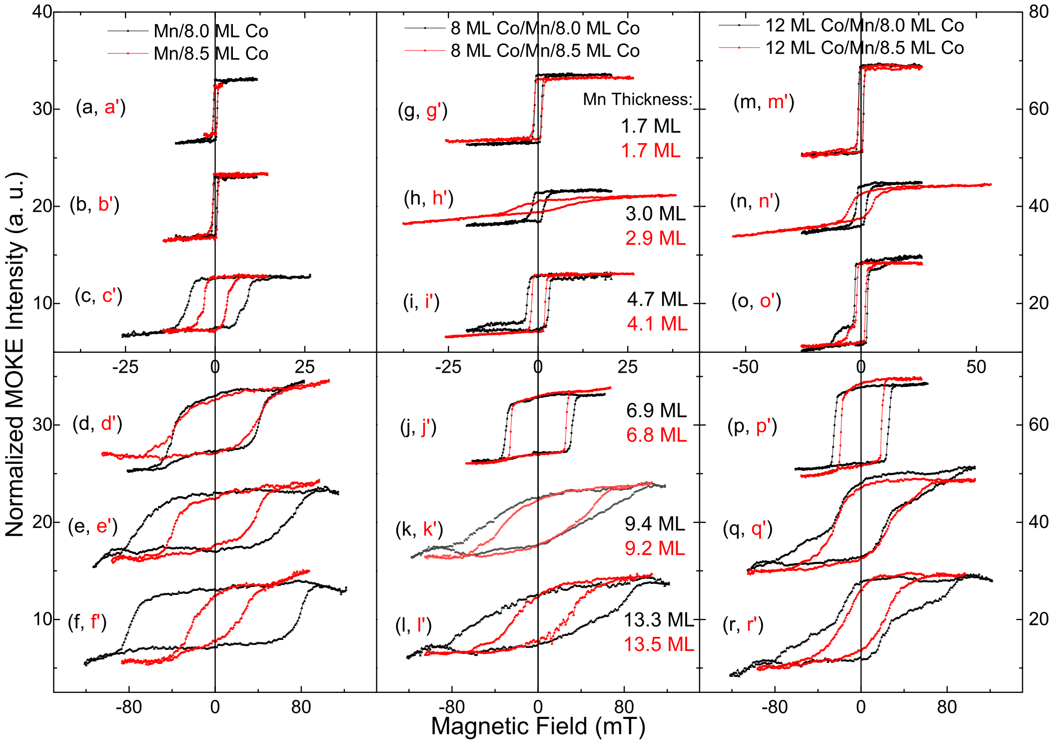

Figure 3. 7 Hysteresis loops measured with the magnetic field aligned parallel to the in-plane [100] crystal direction for Mn wedge/8 (8.5) ML Co, 8 ML Co/Mn wedge/8 (8.5) ML Co, 12 ML Co/Mn wedge/8 (8.5) ML Co with different thickness of Mn, as indicated in the middle panel.

The data for bilayers and trilayers with 8.0 ML and 8.5 ML bottom Co layer are presented in this section. Figure 3. 7 shows normalized magnetic hysteresis loops, measured by longitudinal MOKE. The coercivity H_c, exchange bias field H_e, and the remanent Kerr signal M_r for 8.0 ML and 8.5 ML thickness of the bottom Co layer are plotted in Figure 3. 8 and Figure 3. 9 as a function of Mn thickness, respectively.

For the 8.0 ML bottom Co layer samples, H_c of the bilayer increases by two shoulders up to 10 ML Mn thickness and then stay at a constant value of 80 mT. The t_{AFM} of Mn is around 4.5 ML thickness at RT. The trilayers show two regions of antiferromagnetic RKKY-type coupling in this Mn thickness range, which can be clearly seen from the loops at 3 and 9.4 ML Mn thickness (Figure 3. 7). The t_{AFM} of Mn is around 5.4 ML thickness. Only one minor loop was observed for trilayers with 4 and 8 ML top Co layer thickness at the second antiferromagnetic RKKY maximum due to the limited field range. In the 12 ML Co/Mn/8 ML Co sample, magnetization reversal of the two

Co layers starts decouple from 8.5 ML Mn thickness.

H_c of the bilayer with 8.5 ML bottom Co layer shows a similar behavior as that of the 10.5 ML bottom Co layer sample, however, H_c slowly decreases to 20 mT after passing the peak maximum (40 mT) at 6.5 ML, and t_{AFM} is around 4.1 ML Mn thickness. H_c of the trilayer samples follows that of the bilayer but with a higher t_{AFM} (4.8 ML). Two regions of antiferromagnetic RKKY-type coupling were found at 3 and 9.5 ML Mn thickness (Figure 3. 8). Separate loops at top and bottom Co layer were only observed at around 8.5 ML Mn thickness in the whole Mn range. H_e starting of the trilayers is higher than in the bilayer, and the H_e value seems to increase with increasing top Co layer thickness.

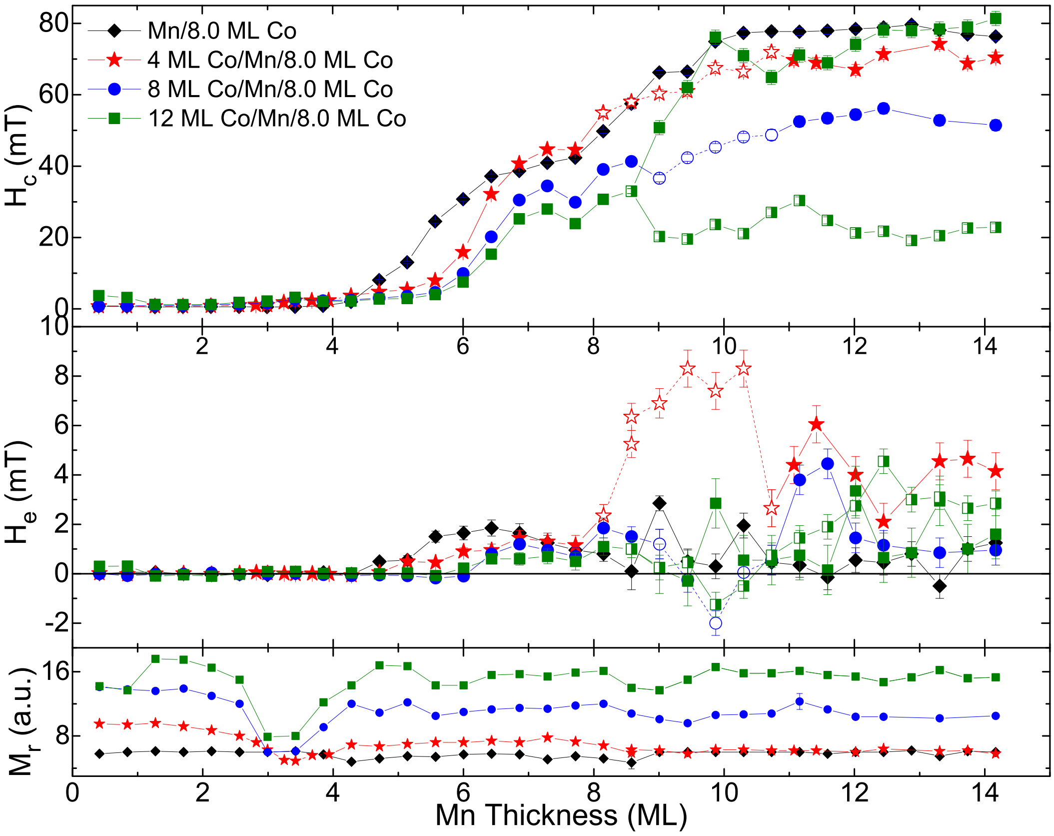

Figure 3. 8 Coercivity H_c (top) and exchange bias field H_e (middle) of 0 ML (black diamonds), 4 ML (red starts), 8 ML (blue circles) and 12 ML (green squares) Co/Mn-wedge/8.0 ML Co trilayer (bilayer) sample as a function of Mn thickness. At higher Mn thicknesses, two different switching fields (bottom Co layer with higher H_s^b, and top Co layer with lower H_s^t (half squares), respectively) are presented for the trilayer samples. Bottom: Kerr signal in remanence of the same samples. Open starts and circles indicate the data from minor loops.

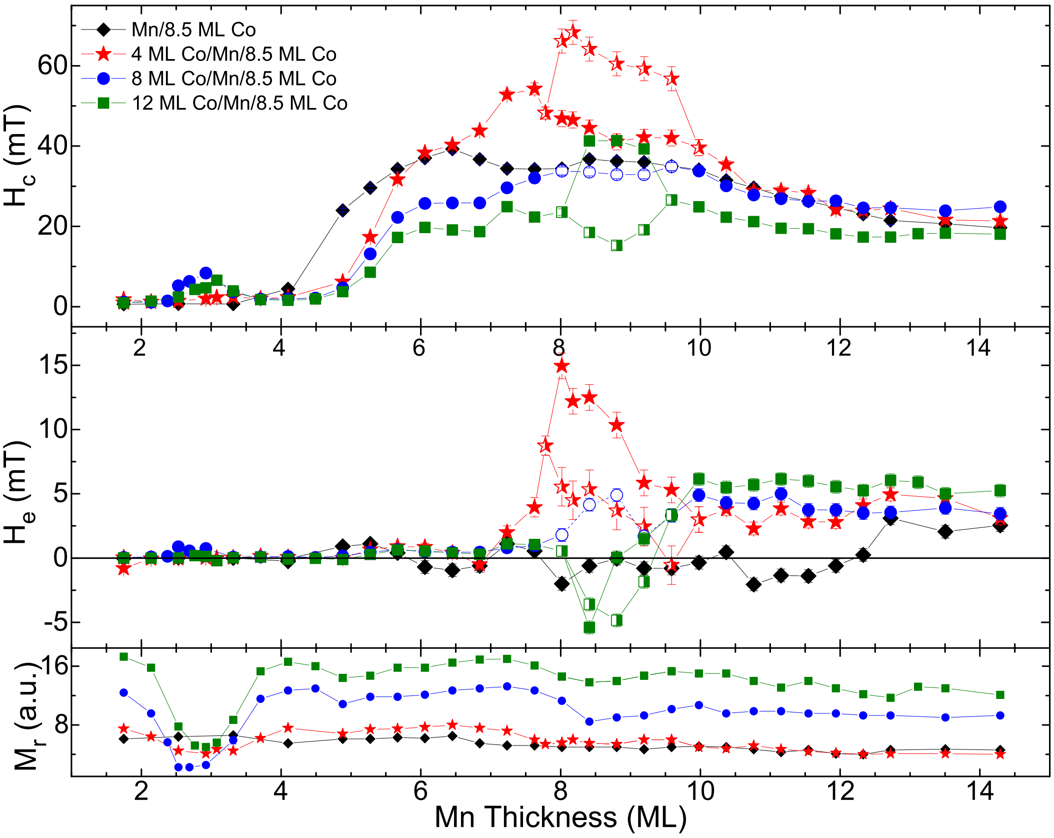

Figure 3. 9 Coercivity H_c (top) and exchange bias field H_e (middle) of 0 ML (black diamonds), 4 ML (red starts), 8 ML (blue circles) and 12 ML (green squares) Co/Mn-wedge/8.5 ML Co trilayer (bilayer) sample as a function of Mn thickness. Half-filled squares are data for the top Co layer for the separated loops around 8.5 ML. Bottom: Kerr signal in remanence of the same samples. Open circles indicate the data from minor loops.

3.2.3 Discussion and conclusions

In this section, we summarize the results from the two different groups of samples that were presented in the last two sections. Figure 3. 10 and Figure 3. 7 are plotted in order to compare these clearly. We don't discuss H_e of the sample with bottom layer with integer number of atomic layers here, the details of this discussion will be presented in sec. 3.3.

First we should clarify some different phenomena in the results. a), there should be two antiferromagnetic maxima of the RKKY-type coupling in trilayer samples in the studied Mn thickness range, i.e., at around 2.5 ML and 8.2 ML Mn thickness. The first maximum was missing in the 10.0 ML bottom Co layer trilayer samples, and the coupling strength was weaker than we expected, both could be due to the bigger thickness variation of Mn within the laser spot, or oxidization of the films could influence the roughness. b), the coercivity of the 10.5 ML bottom Co layer bilayer and trilayer samples decreases quickly after the maximum, whereas the 8.5 ML case shows a slow decrease after the peak maximum. We explain the latter by a slithtly inhomogeneous thickness of the bottom layer. Even a difference of 0.1 ML Mn thickness will influence the coercivity of bilayer and trilayer a lot. This will be discussed in a latter section.

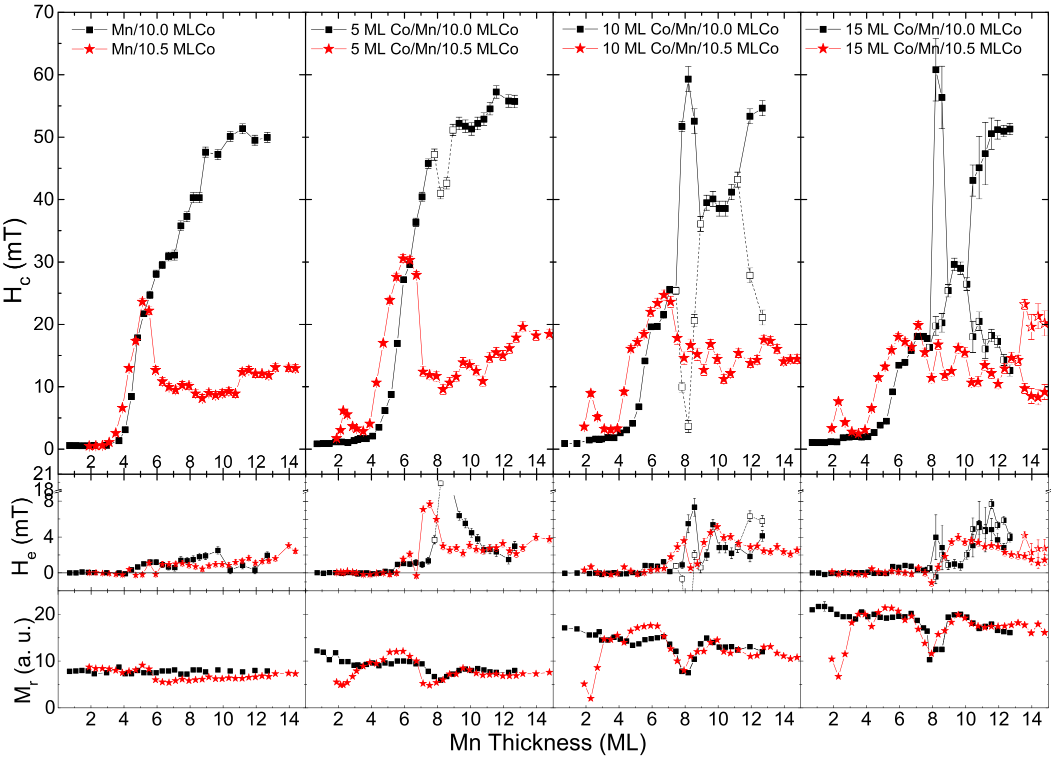

Figure 3. 10 Coercivity H_c (top), exchange bias field H_e (middle), and remanent Kerr signal of 10.0 ML (black squares) and 10.5 ML (red stars) bottom Co bilayers and trilayers as a function of Mn thickness.

Now we can list some results from the above samples.

1. t_{AFM}: Bilayers with Co film with half-filled topmost atomic layer show smaller values of t_{AFM} than in the filled case, i.e., t_{AFM} = 3.4 ML and 4.1 ML for 10.5 ML and 8.5 ML Co thickness, respectively, while t_{AFM} = 4.3 ML and 4.5 ML for 10.0 ML and 8.0 ML Co thickness, respectively. All trilayers have a larger t_{AFM} than the corresponding bilayer, and the difference in t_{AFM} between the bilayers and trilayers is larger for filled than for half-filled Co bottom layers (Table 3.1).

2. H_c: The coercivity of the bilayers with completely filled topmost atomic layer of the Co film shows two times an increase with increasing Mn thickness, i.e., at 4 ML - 7 ML and at 7 ML -10 ML, and then keeps a constant value (~50 mT for 10.0 ML and ~80 mT for 8.0 ML Co layer). H_c of the trilayers displays a similar behavior. Due to the larger t_{AFM} value, these two increasing slopes phenomena appear at thicker Mn layers. Furthermore, the loops of the trilayers show a different behavior due to antiferromagnetic RKKY-type coupling, and the decoupled magnetization reversal of the two Co layers appears at higher Mn thicknesses. The second difference between the two samples that can be related to the different interface roughness is that the H_c of the 10.5 ML bottom Co layer sample shows a sharp maximum at around 5-6 ML Mn thickness and then strikingly decreases to nearly half the value of this maximum (~10 mT for 10.5 ML and ~20 mT for 8.5 ML Co layer). This behavior is consistent with data of a wedged Mn/20 ML Co/Cu(001) bilayer,[20] and may thus be explained by assuming a similar interface roughness of our 10.5 ML and the 20 ML Co layers in Ref. 20. A dependence of H_c on the AFM/FM interface roughness has been observed before in Mn/Co bilayers, and has been attributed to a biquadratic exchange interaction between FM and AFM spins due to roughness.[59,60] For the trilayer case, a major difference to the case of the atomically filled bottom Co layer is that magnetization loops with only one step are observed for all Mn thicknesses under study. This could be due to the lower coercivity of the bottom Co layer, as seen from the Mn/10.5 ML Co or Mn/8.5 ML Co bilayers. It is more similar to the coercivity of the top Co layer, which could lead to a merging of the magnetization reversals, possibly also mediated by stray fields from propagating domain walls. We will talk about these later in wedged Co/Mn/10.0 ML and 10.5 ML Co trilayers in sec. 3.6.2. Furthermore, above 8 ML Mn thickness the H_c of 10 ML Co/Mn/10.5 ML Co shows an oscillation with a period of around 1 ML Mn thickness, which can be attributed to the layer-by-layer growth of Mn on Co. We will discuss this further down in connection with the behavior of the 10 ML Co/Mn/10.0 ML Co trilayers at higher Mn thicknesses in sec. 3.5.

3. H_e: The onset Mn thickness for the appearance of the exchange bias field H_e should be higher than that of the maximum of the coercivity. Unfortunately, the onset thickness of

H_e could not be determined from the above results. One reason is that the coercivity dramatically decreases after the maximum with increasing Mn thickness, and the MOKE signal averages different thicknesses of Mn due to the large Mn slope. This will lead to an big error, such that the data for H_e become unreliable. Another error arises from the RKKY coupling. Errors also come from the not fully separated two magnetization reversals. One reliable conclusion about H_e is that its magnitude for the trilayers is always higher than in the bilayers, and it seems that the intensity decreasing with top Co thickness increasing.

Bottom layer	8.0 ML Co	8.5 ML Co	10.0 ML Co	10.5 ML Co
Bilayer t_{AFM} (ML)	4.5	4.1	4.3	3.4
Trilayer t_{AFM} (ML)	5.4	4.8	5.2	3.9
Δt_{AFM} (ML)	0.9	0.7	0.9	0.5

Table 3.1 The onset thickness (t_{AFM}) for AFM order in Mn/Co bilayer, and Co/Mn/Co trilayer films.

3.3 Co/wedged Mn/Co trilayers with thinner Mn layer

In this section, we focus on thinner Mn thicknesses in Co/Mn/Co/Cu(001) trilayers. The aim of this section is to investigate the trilayer samples with better Mn thickness resolution, comparing to the overview results in sec. 3.2. The thickness of the two Co layers, temperature, and interface roughness were changed to study this system.

3.3.1 Temperature dependence of (Co/) wedged Mn/8.0 ML Co

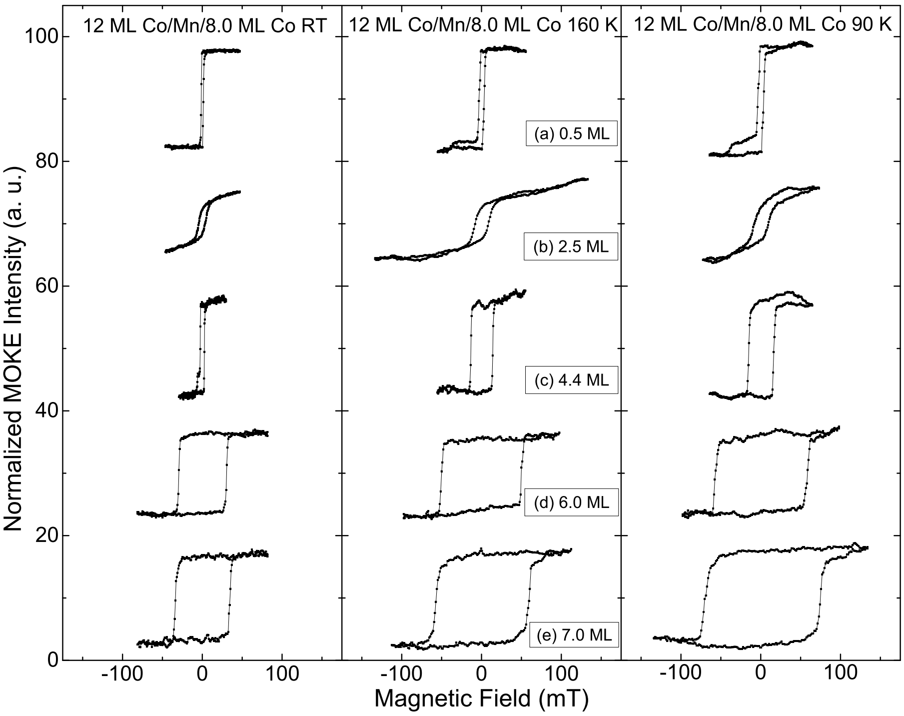

Figure 3. 11 Hysteresis loops measured with the magnetic field aligned parallel to the in-plane [100] crystal direction for 12 ML Co/Mn wedge/8.0 ML Co with different thickness of Mn measured at RT (left), 160 K (middle), and 90 K (right), respectively.

Different thicknesses of the top Co layer of trilayer samples were prepared and measured by MOKE at different temperatures. Coercivity H_c and remanent Kerr signal M_r are plotted as a function of Mn thickness in Figure 3. 12. Figure 3. 11 shows selected magnetization loops for 12 ML Co/Mn/8.0 ML Co at RT, 160 K, and 90 K. First let us see the bilayer sample. The H_c vs Mn thickness presents three sections of increasing slopes from 4 ML-4.7 ML, 4.7 ML-6.5 ML, and above 6.5 ML Mn thickness. The first increase between 4 ML-4.7 ML Mn thickness has not been seen in the bilayer sample with larger ΔMn thickness in sec. 3.2. This first increase of H_c is smaller than the subsequent one between 4.7 ML and 6.5 ML Mn thickness. The onset of antiferromagnetic order of Mn is at around 4 ML for the bilayer, while it is 4.7 ML for the trilayers. The different of t_{AFM} between the bilayer and the trilayer samples is exactly the same as for the samples with layer Mn thickness slope of sec. 3.2.

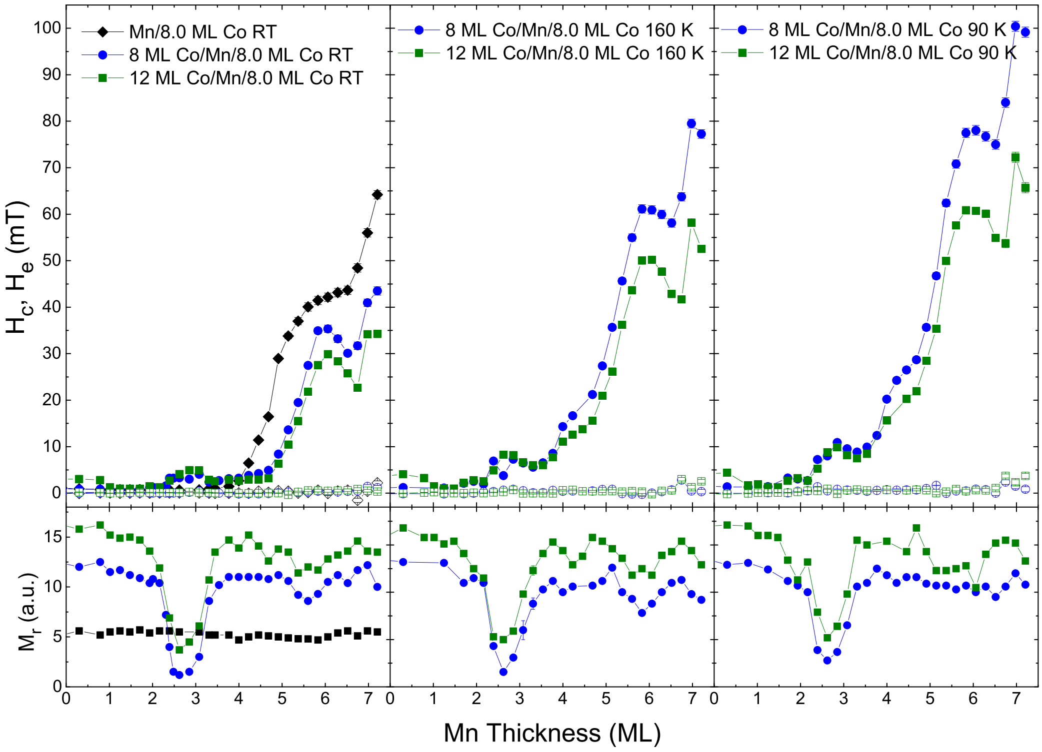

Figure 3. 12 Coercivity H_c (top) and remanent Kerr signal M_r (bottom) of 0 ML (black), 8 ML (blue), and 12 ML (green) Co/Mn wedge/8.0 ML Co bilayers and trilayers as a function of Mn thickness at different temperatures (left: room temperature, middle: 160 K, and right: 90K).

We now turn to the trilayer samples. Because both the loops of trilayer samples with 8 ML and 12 ML top Co layer present similar behavior (Figure 3. 12), only the loops for 12 ML Co/Mn/8.0 ML Co are shown in Figure 3. 11 at different Mn thicknesses and different temperatures. Square loops are observed in the trilayers in this Mn thickness range, and only one antiferromagnetic RKKY-type coupling is observed at around 2.5 ML Mn thickness [(Figure 3. 11(b)]. The first increase of H_c with Mn thickness of the trilayers occurs between 4.7 ML and 6 ML Mn thickness, where H_c increases up to 30 mT [(Figure 3. 11(d)], then it decreases until 6.6 ML Mn to 23 mT. This is the Mn thickness at which the second increase of H_c in the bilayer case with Mn thickness ends (Figure 3. 12). Above 6.6 ML Mn thickness, H_c of the trilayers starts to increase again. In the last section, we saw that H_c of trilayers with bottom Co layer with half-filled atomic termination continued to decrease at these Mn thicknesses.

The H_c of the trilayers at lower temperatures (LT) follow the RT case. The values of H_c are higher than at RT due to the stronger antiferromagnetism of Mn at LT. t_{AFM} at LT is difficult to determine because it coincides with the Mn thickness of the first antiferromagnetic RKKY coupling maximum. One obvious difference of H_c compared to RT is the existence of an additional small increase with Mn thickness between Mn thicknesses of 4 and 4.7 ML, similar as in the bilayer.

3.3.2 (Co/) wedged Mn/10.0 ML Co

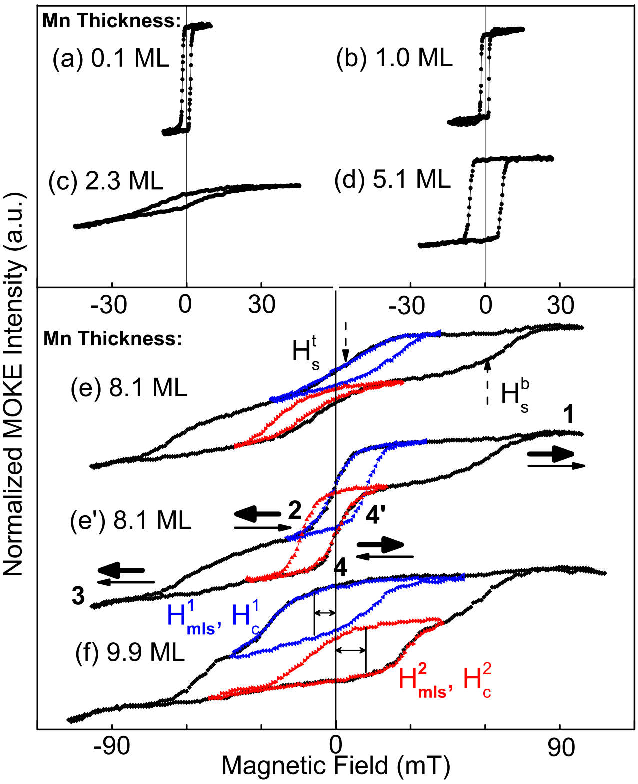

Figure 3. 13 (a–e, f) Hysteresis loops measured with the magnetic field aligned parallel to the in-plane [100] crystal direction for 10 ML Co/Mn wedge/10.0 ML Co, (e′) for 15 ML Co/Mn wedge/10.0 ML Co. H_s^t and H_s^b label the switching field of the top and the bottom Co layer, H^1_c and H^2_c the coercivity of the top Co layer in the positive and negative field minor loop measurements, respectively. $H^{1,2}_{mls}$ defines the shift of the minor loops with respect to zero field. The arrows in (e′) represent the magnetization of the different layers. Blue and red curves indicate positive and negative field minor loop measurements, respectively.

Bilayer and trilayer (Co/) wedged Mn/10.0 ML Co samples with thinner Mn layer were prepared which served to measure the RKKY-type coupling energy around 8.2 ML Mn thickness. Also the exchange bias field is discussed for these samples.

Figure 3. 13 shows normalized magnetic hysteresis loops of a trilayer sample, measured by longitudinal MOKE. Square loops with low coercivity (H_c) start from zero Mn thickness; the tilted loop at 2.3 ML Mn thickness [Figure 3. 13(c)] indicates antiferromagnetic interlayer coupling. The increase in H_c above 5.1 ML Mn thickness is attributed to the onset of AFM order of Mn. Above 7 ML Mn, one with loops with two separate steps are observed, where the one with the lower coercivity H_s^t corresponds to the top Co layer, the higher coercivity H_s^b to the bottom Co layer [Figure 3. 13 (e), (e′), (f)]. Minor loops were measured to estimate the size of the interlayer coupling.

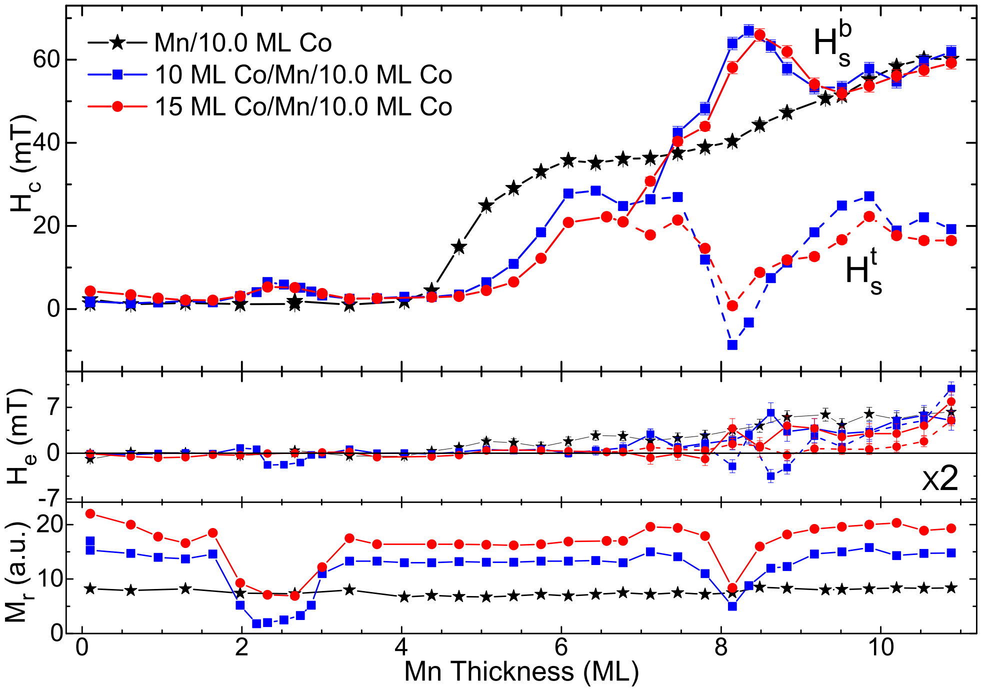

Figure 3. 14 Top: Coercivity H_c (solid symbols) and exchange bias field H_e (open symbols, note here the 2-fold zoom of the H_e data) of 0 ML (stars), 10 ML (squares) and 15 ML (circles) Co/Mn-wedge/10.0 ML Co trilayer (bilayer) sample as a function of Mn thickness. Above 7 ML Mn two different switching fields (bottom Co with higher H_s^b, H_e^b, and top Co with lower H_s^t, H_e^t, respectively) are presented for the trilayer samples. Bottom: Kerr signal in remanence of the same samples.

The coercivity H_c, exchange bias field H_e, and the remanent Kerr signal M_r are plotted in Figure 3. 14 as a function of Mn thickness. The thickness of the bottom Co layer was always 10.0 ML, while the Mn and the top Co layer thickness were changed to modulate the exchange bias and interlayer coupling. Let us first look at the data of the Mn/Co bilayer sample (black stars in Figure

3. 14). The initial small decrease of H_c of the bilayer with increasing Mn thickness, hardly visible in Figure 3. 14, which could be due to a change of the interface structure. The bare Co/Cu(001) film reverses mostly by domain nucleation and domain wall (DW) propagation, the additional Mn atoms could increase the nucleation core, and/or reduce the DW depinning field. H_c of the bilayer starts to rise at around 4.1 ML Mn thickness, indicating the onset of AFM order in Mn at RT. This thickness is larger than in previous works (2 ML[102] and 2.5 ML[20]). This difference could arise from the different preparation temperature of Mn [250 K (t_{AFM} = 2 ML) and 330 K (t_{AFM} = 2.5 ML), respectively]. H_c continues to increase sharply until 6 ML, and then with a slower increase up to around 12 ML, after which it then stays about constant (not shown), with the same typical two shoulders as in the other Mn/Co bilayer samples, as discussed before. Exchange bias appears at around 8 ML Mn thickness.

We now turn to the trilayer systems. Here, both H_c and M_r decrease from 0 to 1.5 ML Mn thickness, which is most clearly seen in the 15 ML Co/Mn/10 ML Co sample. The higher coercivity at 0 ML Mn is attributed to the structural relaxation of the strained Co layer by the appearance of misfit dislocations at the higher total Co thickness when no Mn is present, while with increasing Mn thickness the Co is divided into two separate layers by the Mn spacer layer. As the Mn thickness increases, an antiparallel interlayer coupling at around 2.5 ML Mn thickness is observed. Tilted loops with large H_c and reduced M_r are observed in that Mn thickness range [Figure 3. 13 (c)]. Even the maximum available field was not sufficient to saturate the sample at this Mn thickness, which indicates that the two FM layers are strongly antiferromagnetically coupled to each other. We cannot exclude that at this thickness (around 2.5 ML Mn) a mixed phase of FM and AFM order exists, similar to what has been concluded for Mn/Co bilayers, and also contributes to the antiparallel coupling.[102,103] Competition between direct exchange and indirect RKKY coupling has been also found in Fe/V(001), where the first AF coupling is missing due to the competition with by the V–V direct exchange coupling from the transient ferromagnetism exited in the superlattices.[104]

From the increase of H_c as a function of Mn thickness, the onset of AFM order of Mn at RT is deduced as 4.8 ML, which is about 0.7 ML thicker than in the bilayer. This could be related to proximity effects at the interfaces, which can influence the ordering temperature of an ultrathin

AFM layer,[105] or to a change of the effective thickness due to alloying at the interface.[106] Exchange bias appears at around 9 ML Mn thickness, though a bit weaker than in the bilayer. This may be attributed to the competition of the two FM layers for the same pinning centers for exchange bias in the AFM layer.[107] Also here the higher onset thickness compared to the bilayer may be related to proximity effects and/or a change in the effective thickness.

The reduced remanence is also observed at around 8.2 ML Mn thickness. Figure 3. 13 (e) and (e′) show the major and minor loops at 8.1 ML Mn for 10 and 15 ML Co/Mn/10.0 ML Co, respectively. One notices that the major and minor loops overcross for the 15 ML Co/Mn/10.0 ML Co trilayer [Figure 3. 13 (e′)]. This is because the thicker top Co layer has the lower coercivity and the higher total moment compared to the thinner bottom Co layer. When the major loop is measured for a field sweep from $+H$ [1 in Figure 3. 13 (e′)] to $-H$ [3 in Figure 3. 13 (e′)] and back to $+H$, the top Co layer reverses back into the positive direction at point 4 with a large change in the Kerr signal while the bottom layer still stays magnetized in the negative field direction. For the minor loop, in contrast, a field sweep from $+H$ [1 in Figure 3. 13 (e′)] to $-H_{\mathrm{min}}$ [2 in Figure 3. 13 (e′)] and back to $+H$, the bottom Co layer stays magnetized in the positive direction and the top Co layer reverses its magnetization into the positive direction at point 4′, which is at a larger positive field than point 4 of the major loop because of the antiparallel coupling to the bottom layer. The overcrossing occurs because the thicker top Co layer exhibits the larger Kerr signal.

From the shift field H_{mls} of the minor loops (Figure 3. 13) we can estimate the interlayer coupling energy J using $J = M_{\mathrm{s}}\, d\, \mu_0\, (H^2_{\mathrm{mls}} - H^1_{\mathrm{mls}})/2$, where $M_{\mathrm{s}} = 1440$ kA/m is the saturation magnetization, and $d = 1.7$ and 2.6 nm for 10 ML and 15 ML top Co layer, respectively, is the thickness of the magnetically softer FM layer. We obtain a value of –33.8 μJ/m^2 for both 15 ML and 10 ML Co top layer samples at 8.1 ML Mn thickness. This confirms that the antiferromagnetic RKKY coupling strength is independent of the FM layer thickness. The coupling strength is nearly the same as in a Co/Cu/Co trilayer (≈ –0.05 mJ/m^2) at the second antiferromagnetic RKKY maximum at 11.5 ML Cu thickness.[35]

3.3.3 Discussion and Conclusions

Two antiferromagnetic RKKY-type couplings were observed in the Co/Mn/Co trilayer samples at around 2.5 ML and 8.1 ML Mn thickness. We first talk about the unexpected antiparallel interlayer coupling loop at around 2.5 ML Mn thickness. From previous results of Mn/Co/Cu(001), W. L. O'Brien *et al.* found that one monolayer Mn has FM order due to the enhanced magnetic moment of surface Mn atoms in direct contact with the ferromagnetic Co layer. Mn at the interface in thicker films has a smaller local magnetic moment and is not ferromagnetically aligned.[103] M. Caminale *et al*. also claim that Mn is FM up to 1 ML thickness, 2 ML-thick islands became AFM, thus implying an FM-AFM phase coexistence in the $1 < t_{\mathrm{Mn}} < 2$ ML thickness range.[102] Our bilayer data shows that the onset of AFM order is upward shifted compared to Refs. 102,103, so it is possible that also the Mn thickness for FM-AFM phase coexistence in our data is shifted upwards, even though we cannot confirm the FM phase in Mn from our MOKE data. We cannot exclude that at this thickness (around 2.5 ML Mn) a mixed phase of FM and AFM order exists, and by direct exchange coupling, also contributes to the antiparallel coupling at this Mn thickness. Secondly, for the second antiferromagnetic RKKY-type coupling the maximum coupling energy is ~-34 μJ/m^2 at 8.1 ML Mn thickness on the Co/Mn/Co sample, which is similar to ~-0.05 mJ/m^2 obtained at the second RKKY-type coupling maxima (11.5 ML Cu) in Co/Cu/Co sample.[35]

For the thickness of the onset of AFM order in Mn (t_{AFM}), the value obtained from Co/Mn/Co trilayers is larger than from Mn/Co bilayers. However, the t_{AFM} values for Ni/Mn/Ni and Mn/Ni samples are identical. This could be due to the different coupling between Mn and out-of-plane Ni and in-plane Co. We will discuss this later in sec. 4.3.

The coercivities of Mn/Co bilayers and Co/Mn/Co trilayers are enhanced at low temperatures. For example, H_{c} at 90 K is twice higher compared to RT at around 6 ML Mn thickness for both Mn/Co and Co/Mn/Co samples. As expected from finite-size scaling,[108,109] t_{AFM} is smaller at LT compared to RT for bilayer and trilayer samples, unfortunately, we cannot determine these values quantitatively due to the influence from the first antiferromagnetic RKKY-type coupling.

3.4 Co/wedged Mn/Co trilayers with intermediate thickness of Mn layer

In this section, we will talk about the temperature dependent interlayer coupling in Co/7-12 ML Mn/15.0 ML Co trilayer samples. We still don't discuss the exchange bias field in this section.

3.4.1 Magnetic properties in (Co/) wedged Mn/15.0 ML Co

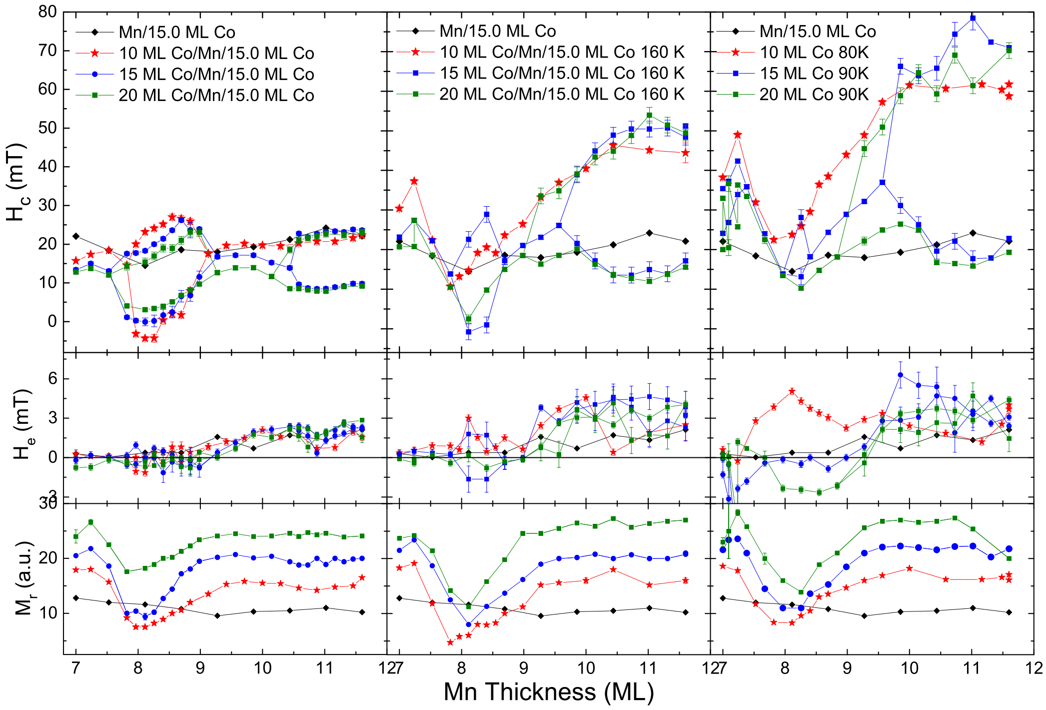

Figure 3. 15 Coercivity H_c (top), exchange bias field H_e (middle), and Kerr signal at remanence M_r (bottom) of 0 ML (black), 10 ML (red) , 15 ML (blue) and 20 ML (green) Co/Mn-wedge/15.0 ML Co trilayer (bilayer) samples as a function of Mn thickness. Two different switching fields (bottom Co layer with higher H_s^b, H_e^b, and top Co layer with lower H_s^t, H_e^t.) are presented for the trilayer samples.

Figure 3. 15 presents an overview of the MOKE results of trilayer samples with different top Co layer thicknesses at different temperatures. Let us shortly describe these data. The data for the Mn/Co bilayer are shown as a reference to compare to the trilayer data. First we look at the results at RT, two separated steps and a reduced remanence are observed in the loops for around 8 ML Mn thickness due to the antiferromagnetic RKKY-type coupling. The coupling strength is independent on top Co layer thicknesses. Decoupled magnetization switching are also found for trilayers with

15 ML (10.1 ML Mn thickness) and 20 ML (10.4 ML Mn thickness) thickness of the top Co layer. Compared to the RT results, only one step is observed in the loop at low temperature (LT) at around 8 ML Mn thickness. This could be due to the strong AF coupling and the limited field range. The observed loop could that be just the minor loop. The onset Mn thickness (t_{dec}) for the presence of two-step magnetization loops decreases with decreasing temperature.

The decoupled magnetization switching is also increasing with decreasing temperature. This is easily seen in Figure 3. 16.

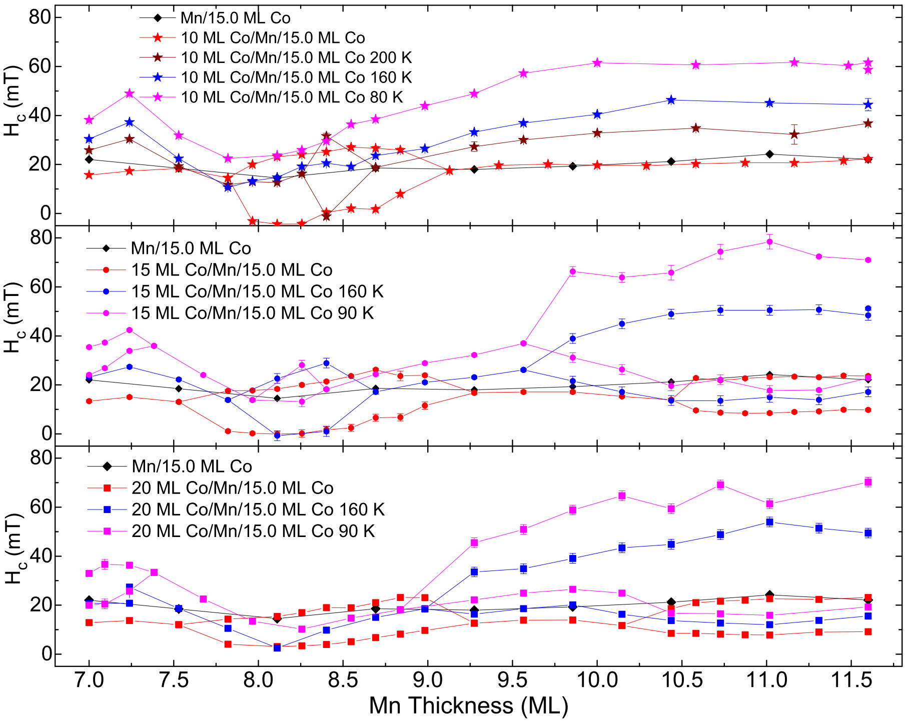

Figure 3. 16 Coercivity H_c of 0 ML (black), 10 ML (red), 15 ML (blue), and 20 ML (green) Co/Mn-wedge/15.0 ML Co trilayer (bilayer) samples as a function of Mn thickness. Two different switching fields (bottom Co with higher H_s^b, H_e^b, and top Co with lower H_s^t, H_e^t, respectively) are presented for the trilayer samples.

3.4.2 Interlayer coupling of different of top Co layers at different temperatures

In this part we mainly focus on the interlayer coupling at different top Co layer thicknesses and temperatures, extracted from minor loop measurements.

We combine the two LT data for discussion, i.e., trilayer samples with 15 and 20 ML top Co layer thickness in Figure 3. 17 and Figure 3. 18, respectively. From the different shift of the two minor loops, we can see clearly the maximum of the antiferromagnetic RKKY-type coupling at around 8.1 ML Mn thickness, and we can simply estimate the coupling energy at RT using: $J = M_s\, d\, \mu_0 (H^2_{mls} - H^1_{mls})/2$, where d = 2.6 and 3.4 nm for 15 ML and 20 ML top Co layer, respectively, is the thickness of the magnetically softer FM layer. We obtain a value of –23±1 μJ/m^2 for both 15 ML and 20 ML Co top layer samples at 8.1 ML Mn thickness. Here the resulting coupling energy is lower than for the trilayers with 10 ML bottom Co layer at the same Mn thickness (~ –34 μJ/m^2 see sec. 3.3.2). This can be attributed to the rougher interface at 15 ML bottom Co layer thickness compared to the 10 ML case.

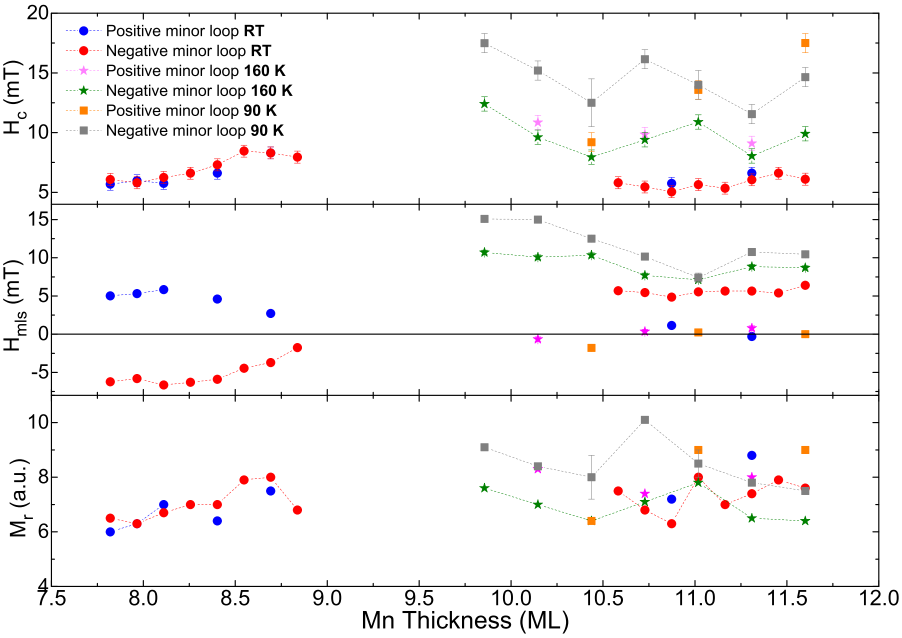

Figure 3. 17 Coercivity (H^1_c, H^2_c) (top), minor loop shift (H^1_{mls}, H^2_{mls}) (middle), and Kerr signal in remanence of the minor loops (bottom) of 15 ML Co/Mn/15.0 ML Co trilayers at different temperatures as a function of Mn thickness for positive and negative minor loops.

The coupling strength between the two Co layers above 9 ML Mn thickness, see from the difference between H^1_{mls} and H^2_{mls}, increases with decreasing temperature. The coupling strength seems to oscillate as a function of Mn thickness, with a maximum at around 10 ML and a minimum at around 11 ML Mn thickness. The period could be 2 ML, which would correspond to direct exchange coupling through the AFM layer. All the coupling values are offset to the positive, which can be attributed to an influence of Néel-type magnetostatic coupling between the two Co layers. At 10.1 ML Mn thickness, we estimate the coupling energy to –21.5±1 μJ/m^2 and –34±1 μJ/m^2 for 20 ML top Co layer samples at 160 K and 90 K, respectively.

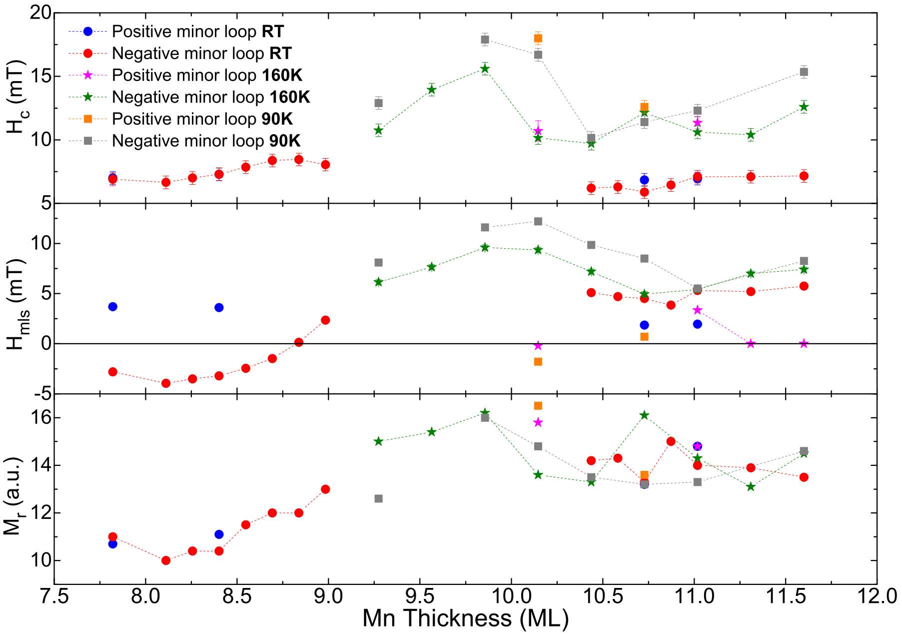

Figure 3. 18 Coercivity ($H^1{}_c$, $H^2{}_c$) (top), minor loop shift ($H^1{}_{mls}$, $H^2{}_{mls}$) (middle), and Kerr signal in remanence of the minor loops (bottom) of 20 ML Co/Mn/15.0 ML Co trilayers at different temperatures as a function of Mn thickness for positive and negative minor loops.

3.4.3 Conclusions

We studied the temperature and top Co layer thickness dependence of the interlayer coupling in Co/Mn/Co trilayers with 8…12 ML Mn thickness. We conclude the following results:

a) The Mn thickness for separate switching of the two Co layers is decreasing with increasing top Co layer thickness as well as for decreasing temperature.

b) The decoupled switching field increases with decreasing temperature.

c) The interlayer coupling above 9 ML Mn thickness is parallel, opposite to the AP coupling for the antiferromagnetic RKKY-type coupling at around 8.1 ML Mn thickness.

d) The maximum coupling energy for the antiferromagnetic RKKY-type coupling at around 8.1 ML Mn thickness is –23±1 $\mu J/m^2$. The maximum coupling energy for direct exchange coupling at 10.1 ML Mn thickness are –21.5±1 $\mu J/m^2$ and –34±1 $\mu J/m^2$ at 160 K and 90 K, respectively.

3.5 Co/wedged Mn/Co with thicker Mn layer

In this section, we will focus on the interlayer coupling between the two FM layers through the AFM layer in the higher Mn thickness range. In order to study the interface roughness dependence of the interlayer coupling, trilayer samples with three different thicknesses of the bottom Co layer are presented to study the interplay between direct exchange coupling through the AFM layer, RKKY-type coupling, and Néel-type magnetostatic coupling.

3.5.1 Co/wedged Mn/15.0 ML Co

0 ML and 20 ML Co/10-14.1 ML Mn/15.0 ML Co samples were prepared and are presented in this section. From the MEED oscillation of 15.0 ML Co/Cu(001), it shows that the oscillation amplitude decreases as the Co thickness increases (not shown here), which means a higher surface roughness.

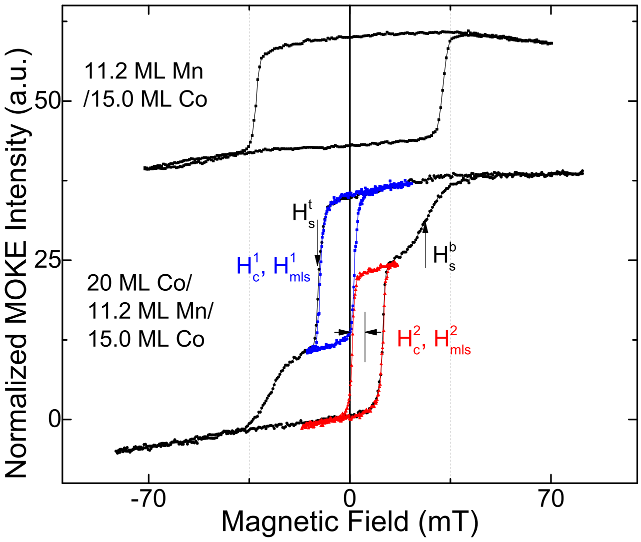

Figure 3. 19 Hysteresis loops measured with the magnetic field aligned parallel to the in-plane [100] crystal direction for 0 ML and 20 ML Co/11.2 ML Mn/15.0 ML Co samples. H_s^t and H_s^b label the switching field of the top and the bottom layer, H^1_c and H^2_c the coercivity of the top Co layer in the positive and negative field minor loop measurements (red, blue), respectively. $H^{1,2}_{mls}$ defines the shift of the minor loops with respect to zero field.

MOKE loops of bilayer and trilayer samples for 11.2 ML Mn thickness are presented in Figure 3. 19. It shows a quite squared loop for the bilayer and a loop with two separated magnetization reversals for the trilayer. Minor loops were measured to estimate the size of the interlayer coupling.

Coercivity, minor loop shift, and remanent Kerr signal are plotted in Figure 3. 20 as a function of Mn thickness. The data presented in sec. 3.2 show that the coercivities (H_s^t, H_s^b) of the major loop are independent from Mn thickness above ~ 9 ML Mn thickness. Here the coercivity fluctuates as a function of Mn thickness, see Figure 3. 20(a). However, this could come from the uncertainty of the bottom Co layer thickness. Even only 0.1 ML thickness difference in the bottom Co layer thickness will lead to a significant change in coercivity for both bilayers and trilayers. The remanent Kerr signal of the major and minor loops decreases with increasing Mn thickness [Figure 3. 20(c)]. The square loop observed at around 11 ML Mn thickness changes to a more tilted loop at thicker Mn thickness.

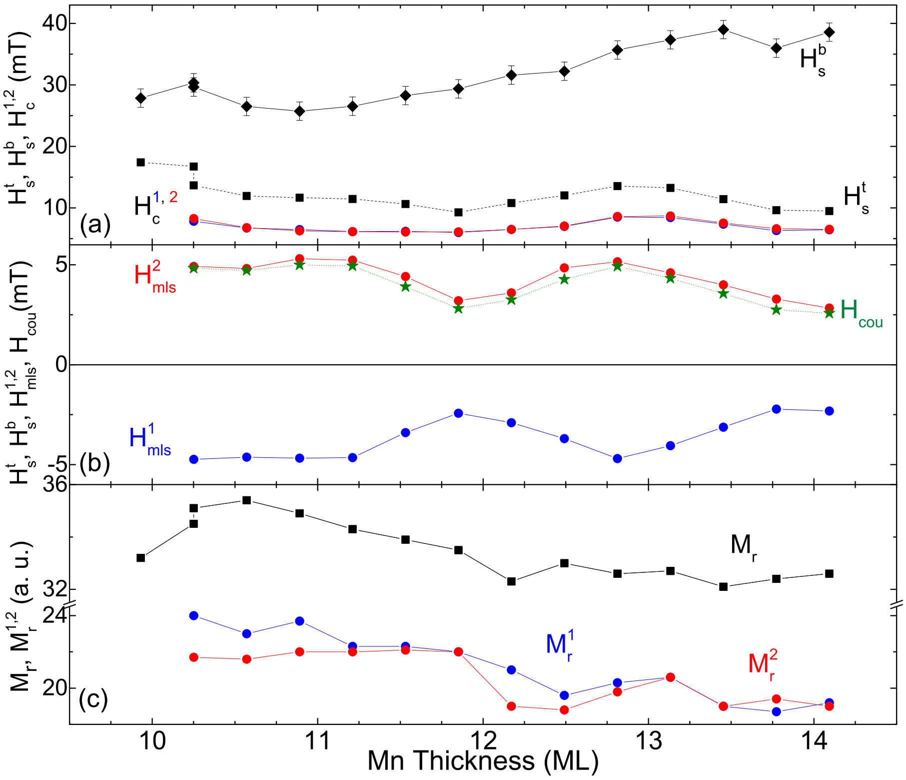

Figure 3. 20 (a) Coercivity $H^{1,2}_c$ ($H_s^{b,t}$), (b) shift field $H^{1,2}_{mls}$ (exchange bias $H_e^{b,t}$) and (c) $M^{1,2}_r$ (M_r) of minor (major) loops for a 20 ML Co/Mn wedge/15.0 ML Co trilayer as a function of Mn thickness. H_{cou} [green stars in (b)] indicates the exchange coupling field between the two Co layers [H_{cou}= (H^2_{mls} – H^1_{mls})/2]. Solid lines are intended to guide the eye.

Now let us turn to the data of the minor loop shift [Figure 3. 20(b)]. The positive and negative H^2_{mls} and H^1_{mls} show the same value with opposite sign. Both present an oscillation with about 2 ML period. Actually only from these data one could not claim a 2-ML-period oscillation, however, we deduce this behavior from data shown later and assign this to the direct exchange coupling between the two FM layers through the AFM layer. The green stars in Figure 3. 20(b) indicate the interlayer coupling field calculated from the minor loop shifts. Using equation $J = M_s\, d\, \mu_0\, (H^2_{\mathrm{mls}} - H^1_{\mathrm{mls}})/2$, $H_{\mathrm{cou}} = 2.6 - 5$ mT, and $d = 3.4$ nm, the interlayer coupling energy is calculated to be in the range of ~ 12.7-24.5 μJ/m^2.

3.5.2 Co/wedged Mn/10.0 ML Co

Bilayer and trilayer samples with an integer number of atomic layers in the bottom Co film (10.0 ML) were prepared and are examined in this section. Figure 3. 21 displays the loops for bilayer and trilayer samples at a Mn thickness of 13.5 ML. Tilted loops are observed at this Mn thickness. Two minor loops overlap in the trilayer with 15 ML top Co layer (also for 10 ML). Coercivity and remanence of the minor loop measurements of the top Co layer are presented in Figure 3. 22. Both show an oscillation with 1 ML period as a function of the Mn layer thickness. The coercivity reflects the AFM–FM exchange coupling strength. Its oscillation can be explained by the modulation of the atomic-scale interface roughness at the upper Co–Mn interface due to the layer-by-layer growth of Mn on Co [Fig. 1 (d)]. The atomic-scale roughness at the interface influences the coupling between the FM and the AFM layer, which manifests itself in the enhancement of the coercivity.[110] Since the minor loops are somewhat tilted and not fully saturated at remanence, their remanence follows the coercivity. We note that the oscillation amplitudes also depend on the thickness of the Mn layer. The amplitude decreases with increasing Mn thickness due to the rougher interface between the top Co and the Mn layer. Around 12.5 ML Mn thickness, the amplitude of the H_c oscillation is 12 mT and 4 mT for the 10 ML Co and 15 ML Co/Mn/10.0 ML Co trilayers, respectively. At the same time, the amplitude of the oscillation in the remanence is about around 50% and 20% of the saturation value for the 10 ML Co and 15 ML Co/Mn/10.0 ML Co trilayers, respectively. The smaller amplitude of the H_c or M_r oscillation for the thicker Co layer can be understood by the coupling to the AFM layer: $H_c \sim 1/t_{\mathrm{FM}}$.

The minor loops of the top Co layer also display some horizontal loop shift. This exchange bias of the top FM layer as extracted from the minor loops seems to oscillate with a 2 ML period like the minor loop shift field H_{mls} (H_{etop} in Figure 3. 22). However, this might be an artifact induced by the interlayer coupling. The bottom layer exhibits a small negative exchange bias, which manifests itself by a loop shift along the positive field axis, since the Co was saturated along the negative field direction during Mn deposition. Because the two steps of the two Co layers in the magnetization loops are a bit tilted and not completely separated, and the bottom layer switching fields are not symmetric around zero field due to the exchange bias, the difference between the switching fields of the two steps is smaller in the negative field side than in the positive. When the minor loop H^1 is measured, the top layer reverses when the switching field in the negative direction is reached. If the two steps partly overlap, some part of the bottom layer is also already reversed. So H^1_{mls} becomes larger if there is an antiparallel coupling between the two layers, and becomes smaller if the two layers are coupled parallel to each other. When the minor loop H^2 is measured, the switching fields of the two Co layers are more distinct on the positive field side, and H^2_{mls} is less influenced by the interlayer coupling. So by adding H^1_{mls} and H^2_{mls} to calculate the exchange bias, it will show a positive shift for parallel coupling and a negative shift for antiparallel coupling. This may fully explain why H_{etop} shows the same oscillation as H_{mls}.

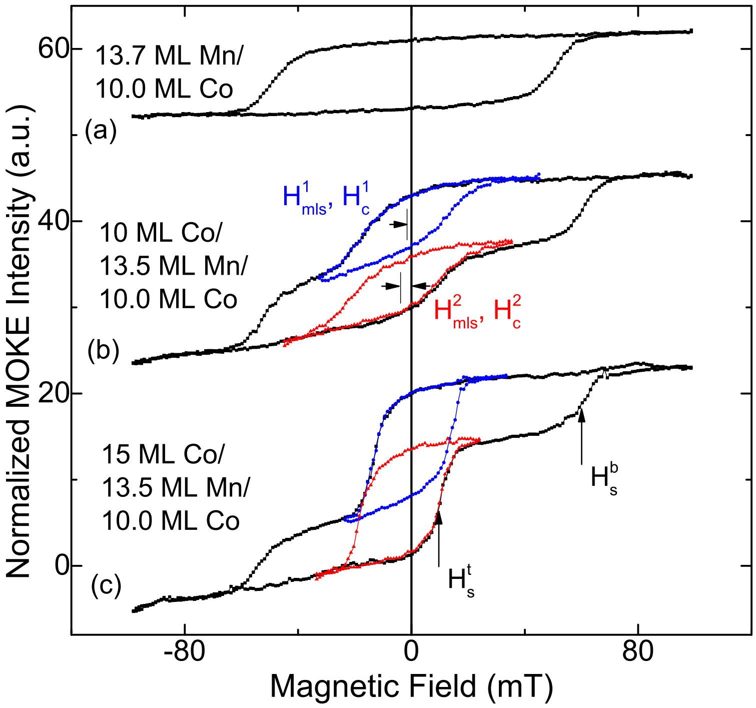

Figure 3. 21 Hysteresis loops measured with the magnetic field aligned parallel to the in-plane [100] crystal direction for 0 ML, 10 ML and 15 ML Co/13.5 (13.7) ML Mn/10.0 ML Co trilayer (bilayer) samples. H_s^t and H_s^b label the switching field of the top and the bottom layer, H^1_c and H^2_c the coercivity of the top Co layer in the positive and negative field minor loop measurements (red, blue), respectively. $H^{1,2}_{\mathrm{mls}}$ defines the shift of the minor loops with respect to zero field.

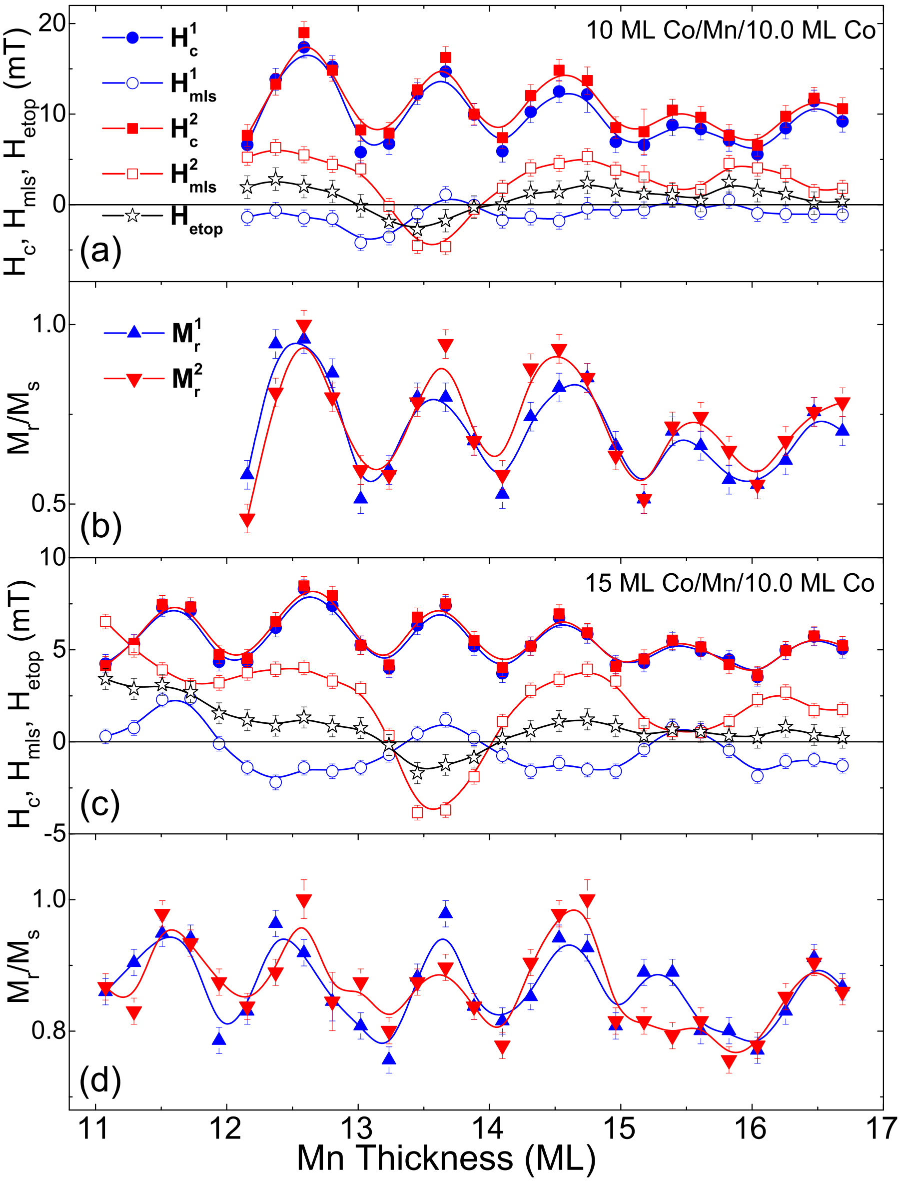

Figure 3. 22 (a) Coercivity H_c (solid symbols), shift field H_{mls} (open symbols) and (b) M_r of minor loops for a 10 ML Co/Mn wedge/10.0 ML Co and (c, d) of a 15 ML Co/Mn wedge/10.0 ML Co trilayer as a function of Mn thickness, red and blue data indicate in the positive and negative field minor loop measurements, respectively. H_{etop} [black stars in (a) and (c)] indicates the exchange bias field of the top Co layer [$H_{etop} = (H^1_{mls} + H^2_{mls})/2$]. Solid lines are intended to guide the eye.

The interlayer coupling energy evaluated from H^1_{mls} and H^2_{mls} is plotted in Figure 3. 23 as a function of Mn thickness. It exhibits an oscillation with a period of 2 ML Mn thickness above a thickness of 10 ML. Such an oscillation may be attributed to direct exchange interaction across the AFM layer. The amplitude of the observed oscillation is about five times smaller compared to the case of Fe/bct-Mn/Fe.[40,62] Another observation is that the oscillation is not around zero, but shifted to the positive side, corresponding to ferromagnetic coupling. This offset of the oscillation points towards an additional Néel-type magnetostatic coupling between the two Co layers.[47] The positive and negative maxima of the coupling strength coincide with the maxima of the coercivity, cf. Figure 3. 22 (a). We conclude that the strength of the interlayer coupling by direct exchange follows the AFM-FM exchange coupling at the interface, which is reflected by the coercivity of the FM layer.

The antiferromagnetic coupling around 13.7 ML Mn thickness is probably the superposition of the short-period interlayer coupling and the third antiferromagnetic maximum of the long-period RKKY coupling. We can thus estimate the relative weight of these two contributions to the coupling at this thickness comparing to the adjacent minima in Figure 3. 23. Both, the direct exchange coupling and the RKKY-type coupling, seem to contribute about equally to the antiferromagnetic coupling (≈ 10 mJ/m^2 each). This coupling strength is nearly the same as in Co/Cu/Co trilayers at the third antiferromagnetic RKKY maximum at 17 ML Cu thickness.[35] However, the amplitude of the oscillations of the coupling energy with 2 ML period is one order of magnitude smaller compared to the value obtained for about the same spacer layer thickness in Co/FeMn/Co sandwiches.[38] We note that the amplitude of the oscillations is slightly larger for 15 ML top Co layer thickness than in the 10 ML case. This could be an artifact from an error in the Co thickness determination, or the manifestation of an effective thickness of the top Co layer smaller than the actual thickness.

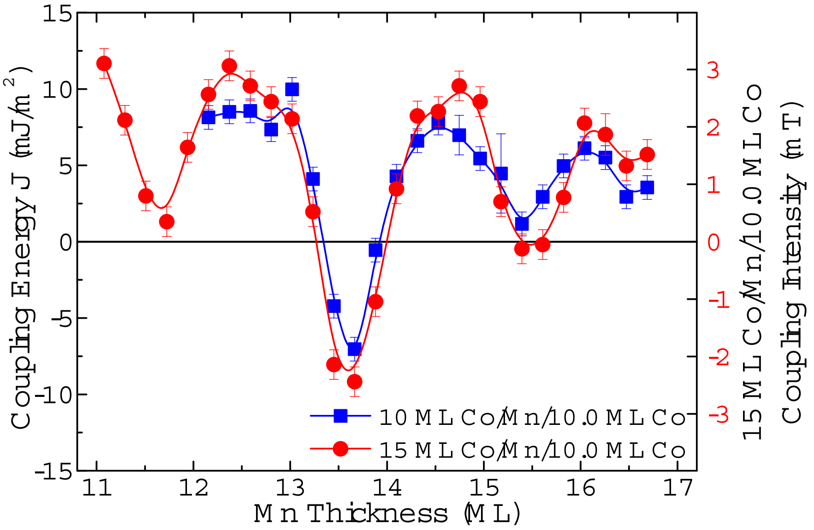

Figure 3. 23 Interlayer coupling field (right) and energy (left) extracted from the shift of minor loops as a function of Mn thickness. Solid lines are intended to guide the eye.

3.5.3 Co/wedged Mn/9.6 ML Co

Trilayer samples with 9.6±0.1 ML bottom Co layer were prepared in order to compare to the case of bottom Co layer with integer number of atomic layers. From the data shown in the previous chapters we know that the decoupling magnetization field became less and less when the thickness of the bottom Co layer changes from integer to half-integer atomic filling. In agreement with that, the difference between H_s^t and H_s^b is smaller in trilayers with 9.6 ML bottom Co layer as shown in Figure 3. 24 than in the 10.0 ML Co case in Figure 3. 21.

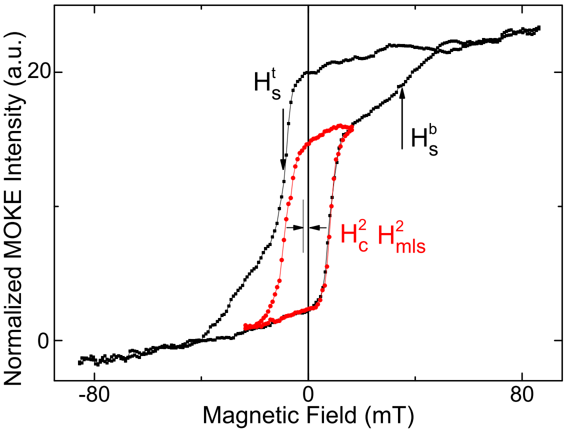

Figure 3. 24 Hysteresis loops measured with the magnetic field aligned parallel to the in-plane [100] crystal direction of a 15 ML Co/19.8 ML Mn/9.6 ML Co trilayer. H_s^t and H_s^b label the switching field of the top and the bottom layer, H_c^2 the coercivity of the top Co layer in the negative field minor loop measurement, respectively. H_{mls}^2 defines the shift of the minor loops with respect to zero field.

Coercivity, shift field, and remanent Kerr signal of minor and major loops are plotted in Figure 3. 25. H_s^b shows a nearly constant value, whereas the H_s^t presents an oscillation with 2 ML period. H_c^2 of the minor loops shows an oscillation with 1 ML period, which is the same behavior as the one observed with a layer of 10.0 ML thickness, and can be attributed to the layer-by-layer growth of Mn on Co. The absence of 1-ML-period oscillation in H_s^t could be due to the combined effect of exchange bias and interlayer coupling, as discussed for the last sample. This can also induce an oscillatory behavior in the exchange bias of the top layer (H_e^b in Figure 3. 25) due to the overlap of the two steps in the magnetization curve. The H_{mls}^2 exhibits an oscillation with a period of 2 ML thickness due to direct exchange interaction across the AFM layer. A deeper trough at around 19.3 ML is probably the superposition of the direct interlayer coupling and the fourth antiferromagnetic maximum of the RKKY-type coupling. From the minor loop shift values in Figure 3. 25 and Figure 3. 22(c), which decrease with increasing Mn thickness, we can deduce that a), the interlayer coupling energy is about the same for bottom Co layers of 9.6 and 10.0 ML thickness; b), at around 19.3 ML Mn thickness in the trilayer with 9.6 ML bottom Co layer, the contribution from the fourth antiferromagnetic maximum of the RKKY-type coupling and the direct exchange coupling are about equal to each other.

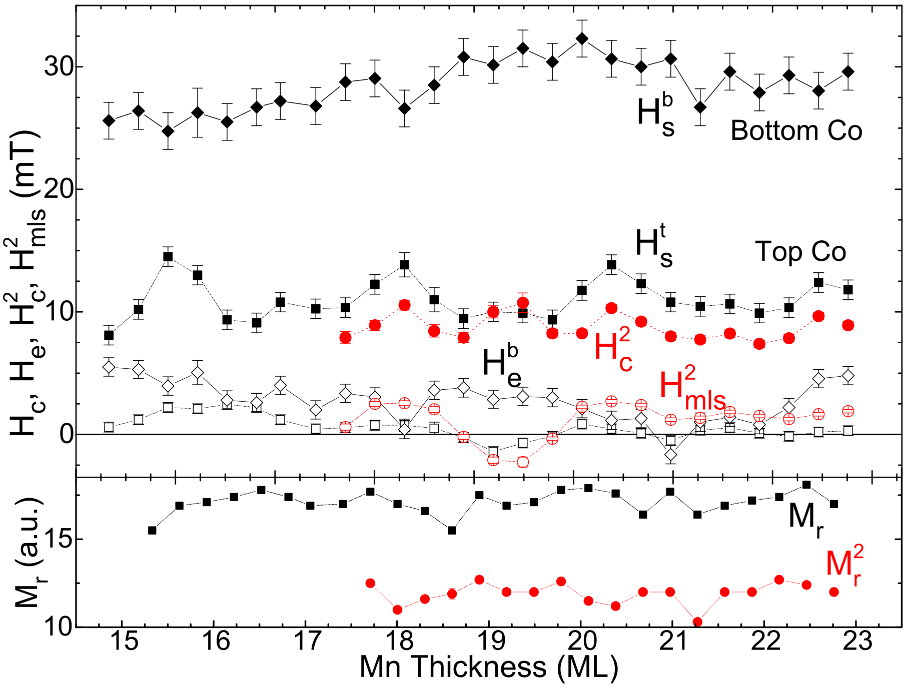

Figure 3. 25 (a) Top: Coercivity H^2_c ($H_s^{b,t}$), shift field H^2_{mls} (exchange bias $H_e^{b,t}$) and M^2_r (M_r) of minor (major) loops for a 15 ML Co/Mn wedge/9.6 ML Co trilayer as a function of Mn thickness. Bottom: Kerr signal in remanence of the same samples.

3.5.4 Discussion and conclusions

Combining these three Co/Mn/Co samples with different interface roughnesses, we discuss now the behavior of the following parameters:

Coercivity H_c: The coercivity of the top Co layer shows an oscillation with 1 ML period as a function of the Mn layer thickness for trilayer samples with bottom Co layer of 10.0 ML as well as

9.6 ML thickness, which is attributed to roughness oscillations at the upper Co-Mn interface induced by the layer-by-layer growth of Mn on Co. These observations demonstrate the influence of the interface structure on the magnetism of the Co/Mn/Co system, and that atomic-scale steps at the interface play an important role in the interlayer interaction and thus for the magnetic properties of the coupled system. And also the oscillation amplitude of the 1-ML-period oscillation of H_c becomes weaker with increasing bottom Co layer thickness. It is absent in the trilayer sample with 15.0 ML bottom Co layer. This could be due to the hither roughness of the thicker Co layer.

Remanence M_r: From the comparison of loops of trilayer samples with bottom Co layer of 15.0 ML, 10.0 ML and 9.6 ML thickness, one can see that more strongly tilted loops are observed for the bottom Co layer of 10.0 ML, i.e., for the smoother lower interface. It similar behavior of bilayers was been reported previously, where the loop of a 25 ML Mn/10.5 ML Co bilayer showed slightly less slanting than the one of 25 ML Mn/10.0 ML Co.[60] Furthermore, the oscillation of M_r with 1 ML period of Mn thickness was only observed in the Co/Mn/10.0 ML trilayer, which also confirms that the more tilted loops exist in Co/Mn/10.0 ML trilayer: If the loops are tilted and not fully saturated at remanence, their remanence follows the coercivity, and thus exhibit such an oscillatory behavior.

Direct exchange coupling: The direct interlayer coupling between the two Co layers in the three samples exhibits an oscillation with a period of 2 ML Mn thickness. From the minor loop shift we can estimate the exchange coupling energy, J, and obtain values in the range of ~12.7-24.5 $\mu J/m^2$ and ~0-15 $\mu J/m^2$ for bottom Co layers of 15.0 ML and 10.0 ML. For Co/Mn/9.6 ML Co, only minor loops of one side have been measured, such that we could only compare these data to the results of the other two samples. From the comparison of these data, we conclude that the coupling energy of the direct exchange coupling is the same for the three different Co/Mn/Co samples.

Néel-type coupling: As discussed in the last paragraph, shifts the coupling oscillations to the positive side, corresponding to ferromagnetic coupling. Such an offset thus points towards an additional Néel-type magnetostatic coupling between the two Co layers.

RKKY-type coupling: The third and fourth antiferromagnetic maximum of RKKY-type coupling were found in Co/Mn/10.0 ML Co (at 13.7 ML Mn thickness) and Co/Mn/9.6 ML Co (at 19.2 ML Mn thickness), respectively, due to the different Mn thickness range. From estimating the relative weight of RKKY-type and direct exchange coupling contributions to the antiferromagnetic coupling, it seems that both contribute about equally to each other.

The interplay between direct exchange coupling through the AFM layer, RKKY-type coupling, and Néel-type magnetostatic coupling determines the overall magnetic interlayer coupling in this system. The detailed atomic and magnetic structure at the AFM/FM interface, i.e., lattice mismatch, uncompensated spins, or strain relaxation can also have an influence on the coupling behavior. For applications in nanotechnology, controlling the magnetic properties of coupled systems by atomic-scale manipulation is an interesting possibility. Here, we have shown that it can be used as an independent parameter in addition to the AFM layer thickness to tune the magnetic properties of an FM layer coupled by interlayer coupling to another FM layer.

3.6 Co/Mn/Co trilayer with Co wedge

In order to study the contribution of the Mn/bottom Co interface on the interlayer coupling, bilayers and trilayers with wedged Co, as well as with half-filled and fully filled topmost atomic layer of the bottom Co film are presented in this section.

3.6.1 Co/Mn/wedged Co

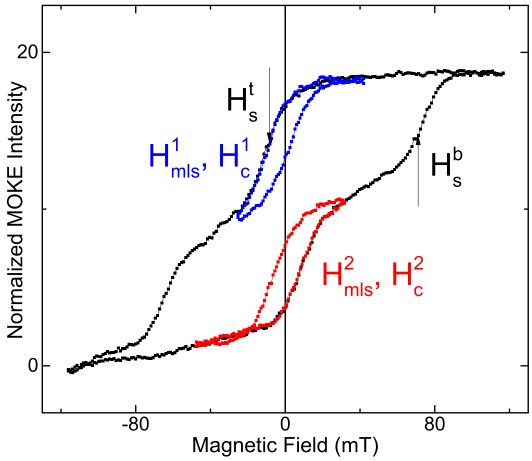

Figure 3. 26 Major and minor hysteresis loops measured with the magnetic field aligned parallel to the in-plane [100] crystal direction for 10 ML Co/15 ML Mn/8.9 ML Co.

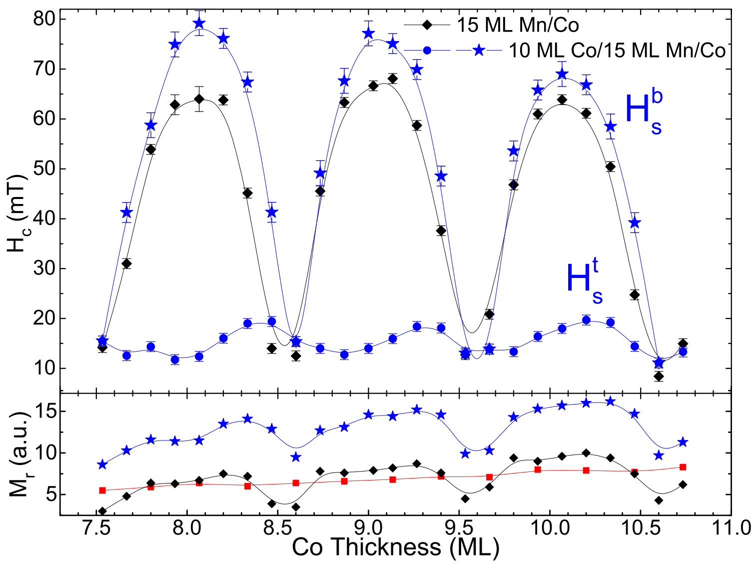

Figure 3. 27 Top: Co thickness dependence of H_c of [100]-MOKE loops for 15 ML Mn/Co wedge bilayer (black color) and 10 ML Co/15 ML Mn/Co wedge trilayer (blue color) samples. Bottom: Kerr signal in remanence of the same samples, the red squares indicate only Co-wedge sample as reference. Solid lines are intended to guide the eye.

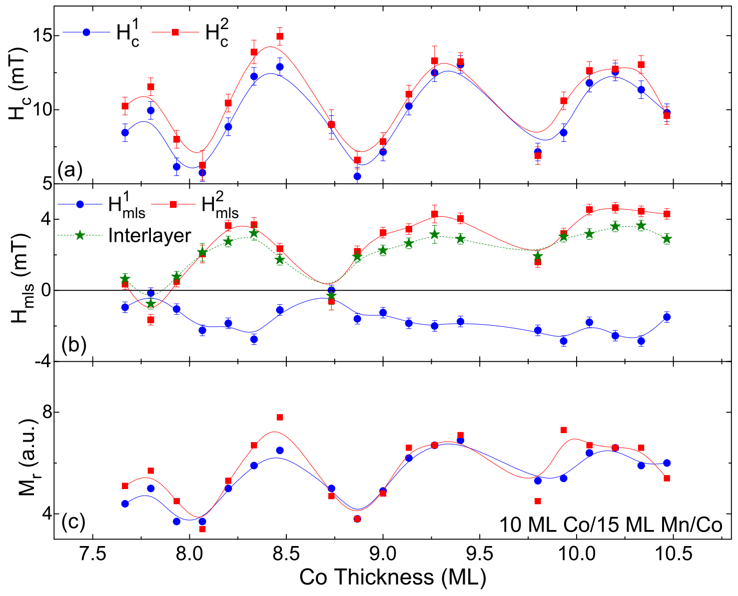

Figure 3. 28 (a) Coercivity H_c, (b) shift field H_{mls}, and (c) M_r of minor loops for a 10 ML Co/15 ML Mn/Co wedge trilayer sample as a function of Co thickness. Green stars in (b) denote the interlayer coupling field. Solid lines are intended to guide the eye.

15 ML Mn/Co wedge bilayers and 10 ML Co/15 ML Mn/Co wedge trilayers were prepared and are discussed in this section. Their H_c and M_r are plotted as a function of the bottom Co layer thickness in Figure 3. 27. Figure 3. 26 shows the minor and major magnetization loops for 10 ML Co/15 ML Mn/8.9 ML Co. First, we talk about the results for the bilayer. Both H_c and M_r of 15 ML

Mn/Co wedge present an oscillation with 1 ML period as a function of the Co thickness. The maxima of H_c are at the integer numbers of atomic layers in the bottom Co film, whereas the minima are at the half-filled terminating atomic layer of the bottom Co film. This is consistent with our results on Mn wedge/half-filled and filled topmost atomic layer Co film bilayers. Similar results have been also reported by J. T. Kohlhepp *et al*[59,60] for a Mn/Co wedge bilayer. They explained the big difference of H_c for different interface roughness at 16 ML Mn thickness by a biquadratic exchange interaction at the interface, in such a way that the interface of Mn/integer number of atomic layers of Co has a stronger orthogonal coupling compared to the Mn/half-integer number of layers Co case. The amplitude of the oscillation should be reduced with increasing Co layer thickness, however, from our results we cannot confirm this behavior because of the large error due to the limited field range. M_r also follows the same oscillation as H_c. This can be ascribed to the tilted loops, as was discussed before.

Now we turn to the 10 ML Co/15 ML Mn/ Co wedge trilayer. Two separate steps show up in the loops as presented in Figure 3. 26. The bottom Co layer has a higher coercivity H_s^t, and the top Co layer has a lower coercivity H_s^b. However, only one step was observed for half-filled topmost atomic layer of the Co film. Figure 3. 27 presents H_c and M_r as a function of the bottom Co layer thickness. Both H_s^t and H_s^b show an oscillation with 1 ML period as a function of the Co thickness, however, the phase is different. H_s^b follows the behavior of the bilayer, i.e., the maxima of H_s^b are on integer numbers of atomic layers in the bottom Co film. Compared to H_s^b, the phase of H_s^t is shifted upward by around 0.3-0.4 ML Co layer thickness. Oscillates H_s^b between 20 and about 80 mT, while the maximum field value decreases as the bottom Co layer thickness increases. In contrast, oscillation of H_s^b is between 12 and 20 mT. The oscillation of M_r follows the one of H_s^b.

Coercivity, loop shift, and remanent Kerr signal of the minor loops are plotted in Figure 3. 28 as a function of bottom Co layer thickness. Both the $H^1{}_c$, $H^2{}_c$ as well as $H^1{}_{mls}$, $H^2{}_{mls}$ follow the behavior of the coercivity of the top Co layer. The interlayer coupling also seems to oscillate with a 1 ML period of bottom Co layer thickness.

3.6.2 Wedged Co/15 ML Mn/10.0 ML and 10.5 ML Co

In the last section, we showed that the H_c of the two FM layers and the interlayer coupling can be modulated by the interface roughness of the Mn/bottom Co layer interface. Two separated steps disappeared for the bottom Co film with half-filled topmost atomic layer. In order to investigate more details, we prepared two samples: wedged Co/15 ML Mn/10.0 ML and wedged Co/15 ML Mn/10.5 ML Co trilayers. The Mn spacer layer with 15 ML thickness was chosen due to two results: a), this thickness is thick enough to decouple the two Co layers; b), this thickness is not at maximum of the RKKY coupling.

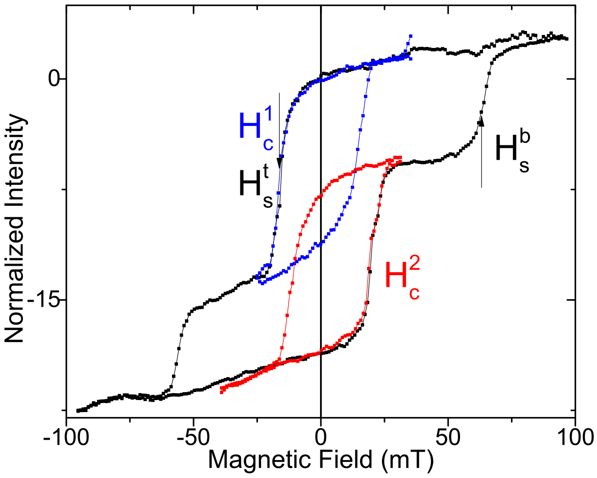

Figure 3. 29 Hysteresis loops measured with the magnetic field aligned parallel to the in-plane [100] crystal direction for 13.5 ML Co/15 ML Mn/10.0 ML Co. Blue and red loops are the positive and negative field minor loop, respectively.

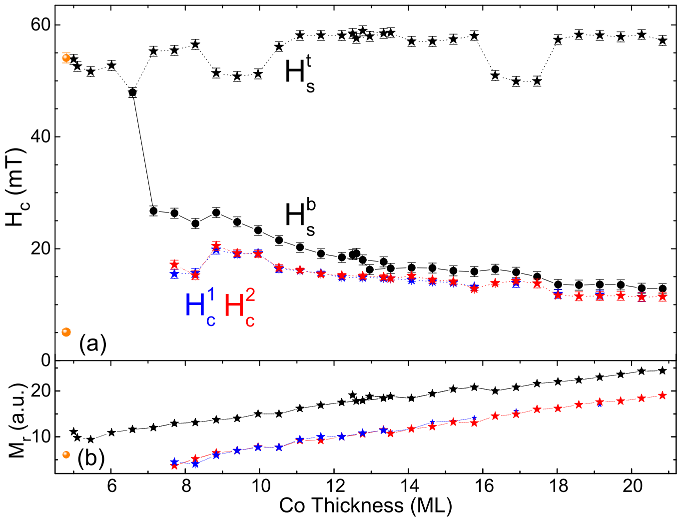

Figure 3. 30 (a) Coercivity (H_s^t top Co layer, H_s^b bottom Co layer) and (b) M_r of 15 ML Mn/10.0 ML Co bilayers (orange) and Co wedge/15 ML Mn/10.0 ML Co trilayer (black) samples as a function of top Co layer thickness. Blue and red stars in (a) and (b) indicate coercivity (H^1_c, H^2_c) and M_r of positive and negative minor loops for the same sample, respectively.

Figure 3. 29 shows the major and minor loops for 13.5 ML Co/15 ML Mn/10.0 ML Co. Coercivity and remanent Kerr signal of major and minor loops are presented in Figure 3. 30 as a function of top Co layer thickness. Two separate steps are observed for top Co layer thickness greater than 7 ML. The step at higher coercivity H_s^b corresponds to the bottom Co layer, this value should be independent of the top Co layer thickness. Two ranges of lower values of H_s^b could come from the defects of like scratches the substrate. The top Co layer was a lower coercivity H_s^b, which shows a decrease with increasing top Co layer. This is expected if the coercivity is dominated by contributions from the interface. The coercivity of the minor loops follow the data of the top Co layer, without showing any oscillation. Furthermore, the M_r of major and minor loops show a linear increase with increasing FM layer thickness.

Now we turn to the Co wedge/15 ML Mn/10.5 Co trilayer sample. Its H_c and M_r as a function of top Co layer thickness and one representative magnetization loop results are plotted in Figure 3. 31. The change of the bottom Co layer thickness by only 0.5 ML leads already to significant changes in the magnetization loops. One-step magnetization reversal is observed for all Mn thicknesses under study, with a low coercivity. This is probably due to the similar coercivity of the two Co layers, such that the two layers couple by domain wall interaction during magnetization reversal, leading to a one-step loop.

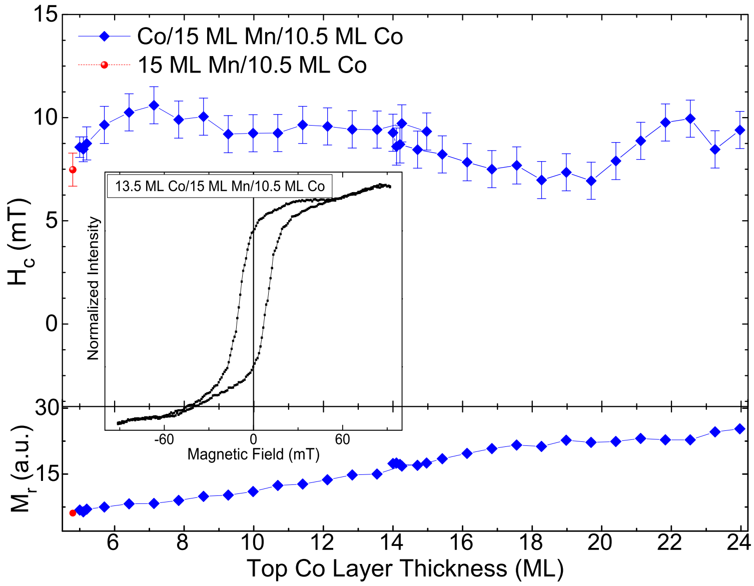

Figure 3. 31 Top: Coercivity H_c of Co wedge /15 ML Mn/10.5 ML Co trilayer as a function of top Co layer thickness. The red dot indicates the result for the 15 ML Mn/10.5 ML Co bilayer. Bottom: Kerr signal in remanence of the same samples. Inset: Magnetization loop of the 13.5 ML Co/15 ML Mn/10.5 ML Co trilayer.

3.6.3 Discussion and conclusions

In the last two sections, we discussed the interlayer coupling and coercivity in Mn/Co and Co/Mn/Co samples dependent on the Mn/bottom Co interface roughness. The coercivity of major and minor loops as well as the remanent Kerr signal show an oscillation with 1 ML period as a function of the bottom Co layer thickness. In the bilayer, the value of the coercivity can be tuned between 65 mT and 20 mT with the help of the Mn/Co interface roughness. The maximum coercivity is at integer numbers of atomic layers in the bottom Co film. The magnetic properties of trilayers are also influenced by the interface between Mn and bottom Co layer. In the trilayer samples, the coercivity of the bottom Co layer shows a similar behavior as in the bilayer case, which means a higher coercivity at integer numbers of atomic layers at the bottom Co layer. The coercivity of the top Co layer inherits the 1-ML-period oscillation as a function of the bottom Co layer thickness, but the phase is shifted by 0.3-0.4 ML. The interlayer coupling strength between the two FM layers also follows this phase-shifted oscillation.

Something also to notice is that only one step is found in the magnetization loops of Co/Mn/Co trilayers when the bottom Co layer thickness is a half-integer number of atomic layers. One possible explanation was already offered, that this could be due to the similarity of the coercivities of the bottom and the Co layers, which could lead to a merging of the magnetization reversals, possibly also mediated by stray fields from propagating domain walls. Another possible explanation is that the two Co layers couple to each other. Figure 3. 31 shows that the coercivity of the trilayer doesn’t change so much when the top Co layer thickness changes from 5 ML to 24 ML. Another, higher coercivity step should be observed if they were separated from each other.

Our results demonstrate that the atomic-scale roughness of the Mn/bottom Co layer interface can be used to tailor the magnetic interlayer coupling as well as the coercivities of the FM layers in such FM/AFM/FM trilayers.

Chapter 4 Structure and magnetic properties of Co(Ni)/Mn/Co(Ni)

In this chapter, we will talk about the (Co/)Ni/Mn/10.0 ML Co and (Co/)Ni/Mn/15 ML Ni samples, compare the results of different ferromagnetic films adjacent films to the Mn layer. In sec. 4.1, the MEED curves and the magnetic domain structures, measured by PEEM, for Ni/Mn/Co trilayers are presented. MOKE data for (Co/)Ni/Mn/10.0 ML Co and (Co/)Ni/Mn/15 ML Ni will be discussed in the sections 4.2 and 4.3.

4.1 Growth and structure

4.1.1 MEED curves of Co(Ni)/Mn/Co(Ni)

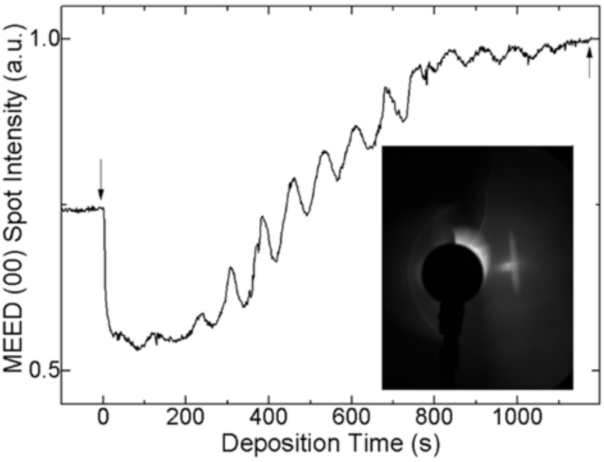

Figure 4. 1 MEED intensity of the (00) spot recorded during the deposition of 15 ML Ni on 6.3 ML Mn/10.0 ML Co at RT. The inset shows the MEED pattern of 6.3 ML Mn/10.0 ML Co before deposition of Ni. Arrows indicate shutter opening and closing, for example by down arrows and up arrows, respectively.

MEED oscillation curves for the growth of Co on Cu(001) and of Mn on Co/Cu(001) have been presented in sec. 3.1. Both show clear periodic oscillations, indicative of layer-by-layer growth. Figure 4. 1 shows a MEED intensity curve for the growth of Ni on 6.3 ML Mn/10.0 ML Co at RT. The oscillation is still clearly seen up to 15 ML Ni thickness. The MEED curve recorded during the growth of Ni on 15.1 ML Mn/10.0 ML Co is presented in Figure 4. 2. Here the amplitude of the oscillation is really weak. This could be due to the higher roughness of the 15.1 ML Mn film compared to the 6.3 ML Mn layer. The inset shows the p(1×1) LEED pattern of 15 ML Ni/15.1 ML

Mn/10.0 ML Co/Cu(001), which indicates a coherent growth of Ni/Mn/Co on Cu(001). These spots are less sharp than the ones of 10.2 ML Co/Cu(001) in Figure 3. 2.

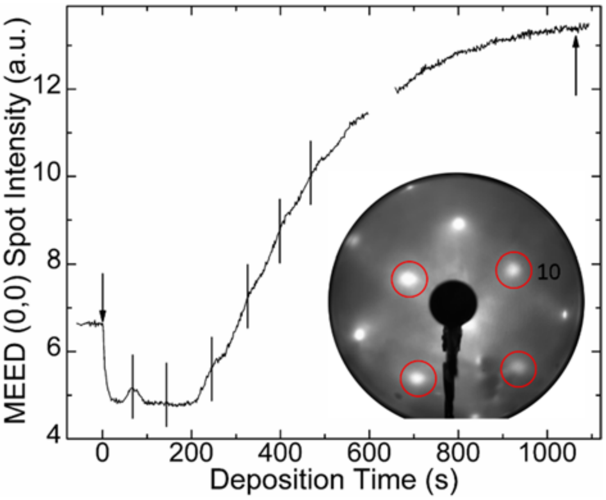

Figure 4. 2 MEED intensity of the (00) spot recorded during the deposition of 15 ML Ni on 15.1 ML Mn/10.0 ML Co at RT. The inset shows the LEED pattern of 15 ML Ni on 15.1 ML Mn/10.0 ML Co (135.8 eV). Data missing around 650s is due to crash of recording software. Red circles indicate the (01) spots. Down and up arrows indicate shutter opening and closing, respectively.

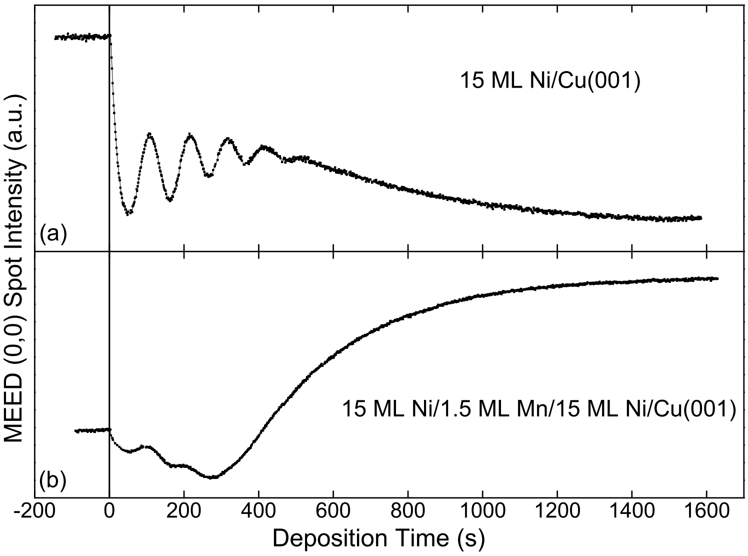

Figure 4. 3 MEED intensity of the (0 0) spot recorded during the deposition of 15 ML Ni on Cu(001) and of 15 ML Ni on 1.5 ML Mn/15 ML Ni/Cu(001) at RT.

Figure 4. 3 (a) shows the MEED curve for deposition of 15 ML Ni on Cu(001) at RT. The amplitude of the oscillation decreases with increasing Ni thickness, and above 5 ML Ni thickness the oscillation is not visible any more, indicating a rougher interface. This results is similar to pervious reflection high-energy electron diffraction data, i.e. around 6 visible oscillations for Ni

deposition on Cu(001).[111] After deposition of 1.5 ML Mn on top of 15 ML Ni/Cu(001), two periods of oscillation are observed for deposition of Ni on 1.5 ML Mn/15 ML Ni/Cu(001), which indicates that the interface roughness is reduced by the 1.5 ML Mn layer on 15 ML Ni/Cu(001). For the thick Ni film, the variation of the background dominates the MEED curve.

4.1.2 Magnetic domain structure of Ni/Mn/Co

15 ML Ni/0-25 ML Mn/0-15 ML Co crossed-wedge films have been prepared on Cu(001) and investigated by PEEM in detail. Figure 4. 4 shows PEEM images for different thicknesses of that sample, using the X-ray magnetic circular dichroism (XMCD) contrast at the Co L_3 and Ni L_3 edges, respectively. An accuracy of about 20% for the Mn and Co layer thicknesses may be involved in the thickness determination for a certain position. The Mn thickness from (d) to (i) is decreasing or constant. Domains with four different directions of magnetization are found in the 15 ML Ni/15 ML Co bilayer sample (i, i'), which is attributed to a four-fold anisotropy along the <110> azimuth directions.[112,113] Comparing the asymmetry value of Ni XMCD, the data from (e), (f), (g), (h) show the same level as the one in (i) between the two maxima. The value of asymmetry in (d) is 1/2.5 compared to others, as shown by the line scans in (a-c). The value of asymmetry is normalized to the same signal-to-background ratio by the following steps: i) scan the XAS data for Ni, Co, and Mn elements in each position of obtained XMCD results. ii) find the absorption intensity for each elements at L_3 edge (I_e) and pre-edge energy (I_p). iii) XMCD contrast image multiply by $[1 + I_p/(I_e – I_p)]$ for corresponding element.

Let us see these XMCD results one by one. (d) and (d') are the domain structures of Ni and Co, respectively, of 15 ML Ni/25 ML Mn/5 ML Co. Smaller rounded domains in Ni are indicative for the typical stripe domain pattern, the magnetization is probably perpendicular to the film plane ("out-of-plane"). No domain wall was found in the Co image, it could be a big domain. The size of the Ni domains becomes bigger with decreasing Mn spacer layer thickness (15 ML Ni/5 ML Mn/5 ML Co), as shown in (b, c). This could be due to the weak coupling to the bottom Co layer, the magnetization in Ni layer is probably still out-of-plane. Even though the asymmetry is larger than in (d), the smaller value in (d) could be due to the lateral resolution. Comparing the domain pattern of Ni and Co in (f) and (f'), both show some common domain boundary and partly antiferromagnetically (AF) -coupled domain structures. These AF-coupled domains probably are the result of the competition between the coupling energy and the anisotropy energy.

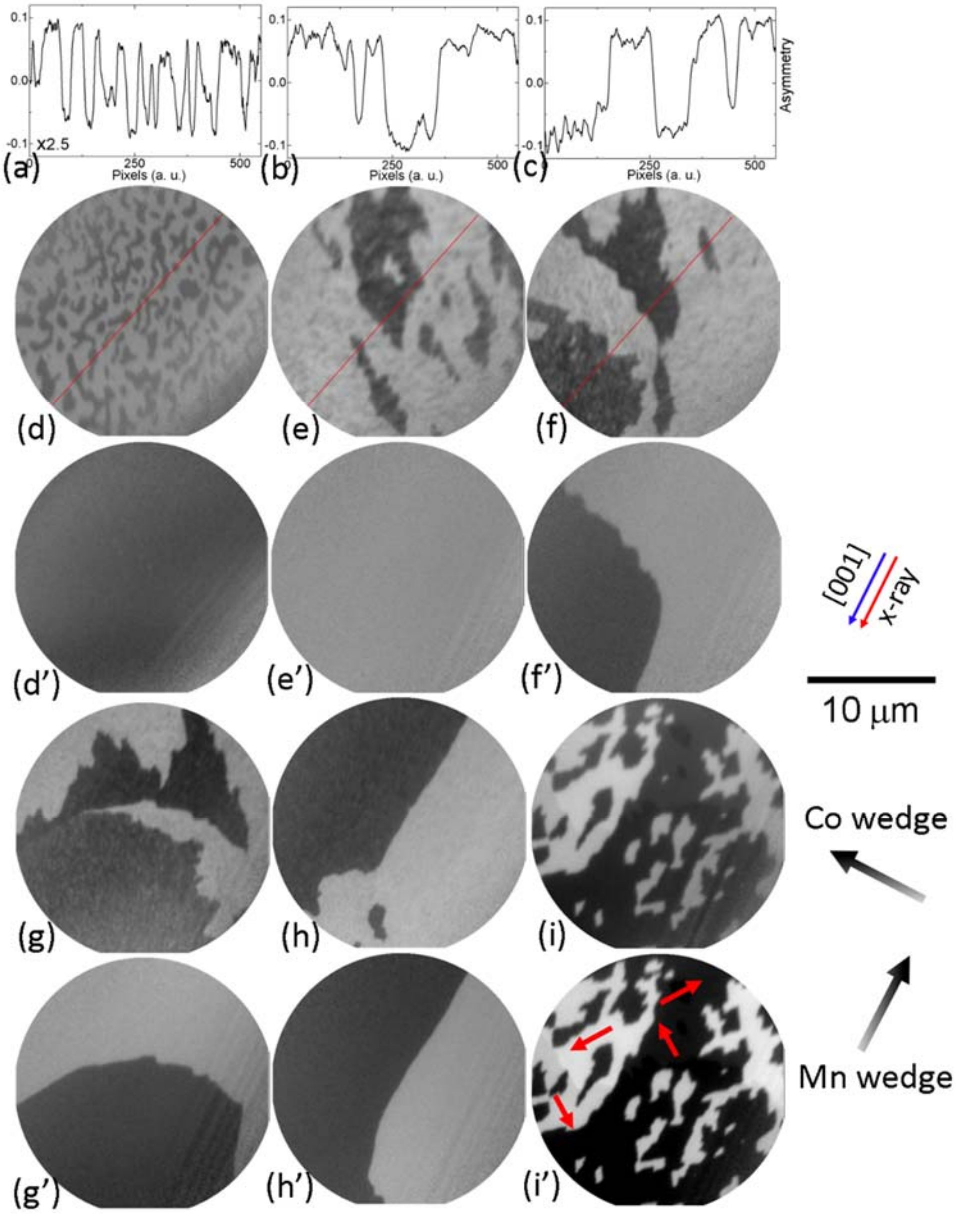

Figure 4. 4 (d-g) and (d'-g') are the XMCD-PEEM images at the Ni and Co L_3 edge of 15 ML Ni/Mn wedge/Co wedge/Cu(001), respectively. (d, d') 15 ML Ni/25 ML Mn/5 ML Co, (e, e', f, f') 15 ML Ni/5ML Mn/5 ML Co, (g, g', h, h') 15 ML Ni/4 ML Mn/5 ML Co, (i, i') 15 ML Ni/15 ML Co. (a), (b), and (c) are the line scans along the red lines printed in each XMCD image (d), (e), and (f) after normalization to the same signal-to-background ratio. Red arrows inside (i') show local magnetization directions.

15 ML Ni on Mn prefer the out-of-plane magnetization with smaller domain size as shown in (d), while the coupling from the Co layer through the Mn spacer layer would like to make spin in Ni layer in-plane. During deposition of the Ni film on top, the anisotropy energy in the Ni layer becomes stronger with more Ni being present, and then the spins like to rotate in order to reduce the anisotropy energy. In this case, the domains in Ni change from bigger structures like Co layer to smaller domains and some antiferromagnetic domains are formed probably due to the lower energy during the domain reconstruction. Compared to the results of Co/Cu/Ni/Cu(001),[114,115] in these samples the stronger coupling from the top Co film restructures and changes the magnetization in the Ni film from out-of-plane to in-plane with increasing Co layer thickness. One of the results is that the Ni layer shows more domains than the Co layer. One thing to notice in (e) and (f) is that some fine domains with less contrast are observed, this could be due to the magnetic ripple, which the in-plane component of the Mn spins is laterally statistically fluctuating, leading to small domains after capping the top Ni layer.[116] In the samples with thinner Mn layer (g, g') and (h, h'), the domains in the Ni film present more similar structures as the Co domains, i.e., more sharp edges of the domains, due to the stronger coupling. At the end, in the 15 ML Ni/15 ML Co bilayer sample, the Ni layer is completely totally coupled to the Co layer, and domains with four different directions of magnetization are found in (i, i').

4.2 Co/Ni/wedged Mn/10.0 ML Co

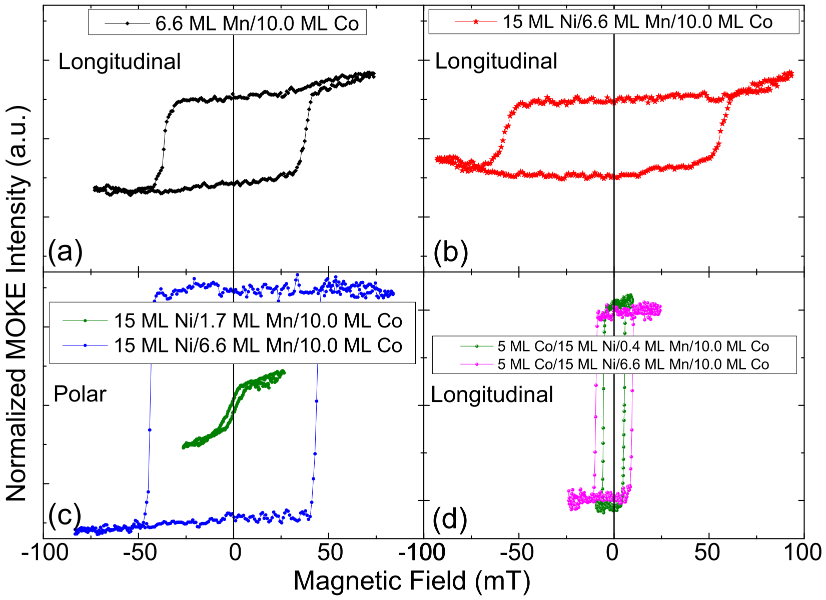

Figure 4. 5 Hysteresis loops measured by polar and longitudinal MOKE for a Mn/Co bilayer, Ni/Mn/Co trilayers and Co/Ni/Mn/Co four-layers at RT. The magnetic field is aligned parallel to the in-plane [100] crystal direction.

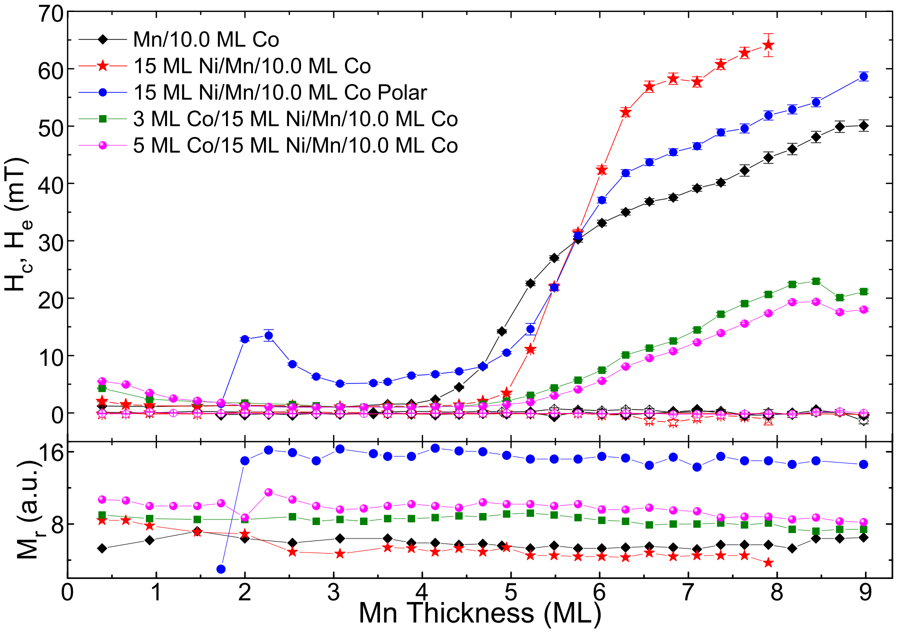

Figure 4. 6 Top: Coercivity H_c (solid symbols) and exchange bias field H_e (open symbols) of Mn/Co bilayer, Ni/Mn/Co trilayers and Co/Ni/Mn/Co four-layers as a function of Mn thickness. Bottom: Kerr signal in remanence of the same samples. Only 15 ML Ni/Mn/10.0 ML Co measured by polar (P, blue) and longitudinal (L, red) MOKE, others are the data from longitudinal MOKE.

15 ML Ni, 3 ML Co/15 ML Ni and 5 ML Co/15ML Ni on Mn wedge/10.0 ML Co and bare Mn

wedge/10.0 ML Co samples were prepared and measured by longitudinal (L) and polar (P) MOKE at RT. If not mentioned, otherwise data are for longitudinal MOKE. Typical hysteresis loops and coercivity H_c and exchange bias field H_e as a function of Mn thickness are shown in Figure 4. 5 and Figure 4. 6, respectively. Wide square loops indicative of AFM order of Mn are observed in 6.6 ML Mn/10.0 ML Co, while additional 15 ML Ni on top trilayer enhance the coercivity. A strikingly decreased coercivity is observed for another 5 ML Co layer on top.

Now we turn to the Mn thickness dependent MOKE data for these samples. The Mn/10.0 ML Co bilayer was already discussed in the previous sections. Here one notices that H_c increases slightly just before the onset of AFM order in Mn, i.e. from 3 to 4.1 ML Mn thickness. Caminale *et al.* reported a coexistence of FM and AF phases of Mn in the $1 < t_{Mn} < 2$ ML thickness range in Mn/Co/Cu(001) at 250 K, and the H_c in this thickness looks slightly higher than FM of Mn.[102] So we cannot exclude that the slight increased H_c for Mn thicknesses between 3 and 4 ML should be due to the coexistence of FM and AFM phases in the Mn layer.

After deposition of 15 ML Ni on top, first we measure the longitudinal MOKE in order to see how the top Ni layer influences the behavior of the bottom Co layer through the Mn layer. The coercivity H_c starts at a little higher value than for bare Mn/Co below 0.8 ML Mn thickness, and at a higher remanent Kerr signal, which comes from the coupling of Co and Ni layers through the thin Mn layer. This will be clearly seen in the polar MOKE results later. H_c stays at the same value as for bare Mn/Co until at around 3 ML Mn thickness, which means that the top Ni layer doesn't influence the bottom Co or Mn layer in this thickness range. A higher t_{AFM} of around 5.0 ML Mn thickness is found, which is similar to the case of Co/Mn/Co trilayers, where also another top FM layer shifted t_{AFM} upwards compared to bare Mn/Co bilayers. The H_c of Ni/Mn/Co displays two slopes of increase with Mn thickness. The first increase of H_c brings the coercivity over the value of the bilayer after about 5.8 ML Mn thickness. This behavior of a higher coercivity in Ni/Mn/Co compared to Mn/Co is similar to 4 ML Co/Mn/8.0 ML Co versus Mn/8.0 ML. From the slightly reduced M_r from 15 ML Ni/Mn/10 ML Co to Mn/10 ML Co as well as the enhanced coercivity, we can explain that this could be due to a change of the Mn spin structure by the top Ni layer.

Now we see the 15 ML Ni/Mn/10.0 ML Co results measured by polar MOKE. There is no out-of-plane signal until 1.7 ML Mn thickness, which indicates that the Ni magnetization is strongly coupled along the in-plane direction due to the bottom Co layer. With increasing Mn thickness, the coupling between Ni and Co layers becomes less, such that the out-of-plane component can be measured by polar MOKE. The H_c data show an influence of the coupling up to 3 ML Mn thickness. The tilted polar MOKE loop of the trilayer with 1.7 ML Mn thickness is shown in Figure 4. 5(c).

The slightly higher H_c in polar MOKE between 3.3 ML and 4.5 ML Mn thickness compared to that of 3 ML Mn thickness is probably due to the FM-AFM phase coexistence in the Mn layer, which upward shift the transition range due to the additional top layer. t_{AFM} is similar to the longitudinal result, i.e., 4.7 ML of Mn thickness. We note that the H_c for the polar MOKE data of 15 ML Ni/Mn/10.0 ML Co is around 5 mT before the onset of AFM order of Mn, which is much higher than 0 ML Ni, 15 ML Ni/Mn/10.0 ML Co of longitudinal data (~1 mT). We will talk about this in the next section. Above t_{AFM}, H_c increases over the value of the Mn/10.0 ML Co bilayer at around 5.4 ML, and assumes an intermediate value between the bilayer and trilayer (longitudinal) up to 9 ML Mn thickness.

At last we deposit Co on top in order to make the Ni top layer magnetization in-plane to know the coupling between the bottom in-plane Co layer and the top Co-Ni ferromagnetic layer. First we deposit 3 ML Co. Tilted loops like the one shown in Figure 4. 5(c) are observed by polar MOKE, indicating a hard axis. We therefore measure over the complete Mn thickness range by longitudinal MOKE. Then we deposit 2 ML Co more and obtain results similar to the 3 ML Co case, which means the magnetization of the Ni layer is already saturated along the in-plane direction due to the Co. From the M_r data, we could deduce that 5 ML Co and 15 ML Ni are about equivalent to the signal of 8 ML Co, such that we can imagine this sample as an 8 ML Co/Mn/10.0 ML Co trilayer. However, the coercivity of 5 ML Co/15 ML Ni/Mn/10.0 ML Co above t_{AFM} is much smaller than that of ~ 8 ML Co/Mn/8.0 ML Co or 10 ML Co/Mn/10.0 ML Co. So the in-plane Ni plays a role that decreases H_c, which is opposite to the fact that out-of-plane Ni increases H_c in the Ni/Mn/10.0 Co sample.

4.3 Co/Ni/wedged Mn/15 ML Ni

In this section, the bottom Co layer is replaced by an out-of-plane magnetized Ni layer in order to study the magnetic coupling between Mn and Ni, as well as in Ni/Mn/Ni. Two different Mn thickness wedge ranges are used in order to cover the coupling range from coupled to decoupled. Polar MOKE is the default measuring configuration in this section.

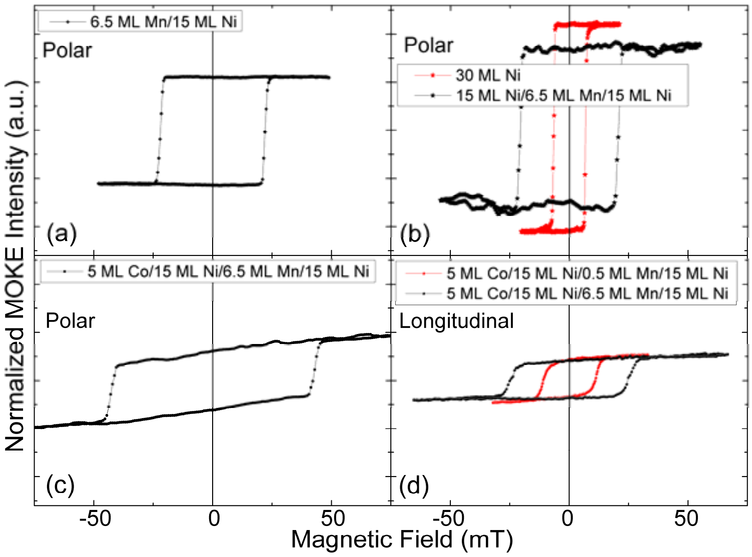

Figure 4. 7 Hysteresis loops measured by polar (a, b, c) and longitudinal (d) (magnetic field aligned parallel to the in-plane [100] crystal direction) MOKE for bilayer, trilayer, and four-layer at RT. (a), 6.5 ML Mn/15 ML Ni, (b), 30 ML Ni (red) and 15 ML Ni/6.5 ML Mn/15 ML Ni (black), (c) 5 ML Co/15 ML Ni/6.5 ML Mn/15 ML Ni, (d) 5 ML Co/15 ML Ni/0.5 ML Mn/15 ML Ni (red), 5 ML Co/15 ML Ni/6.5 ML Mn/15 ML Ni (black).

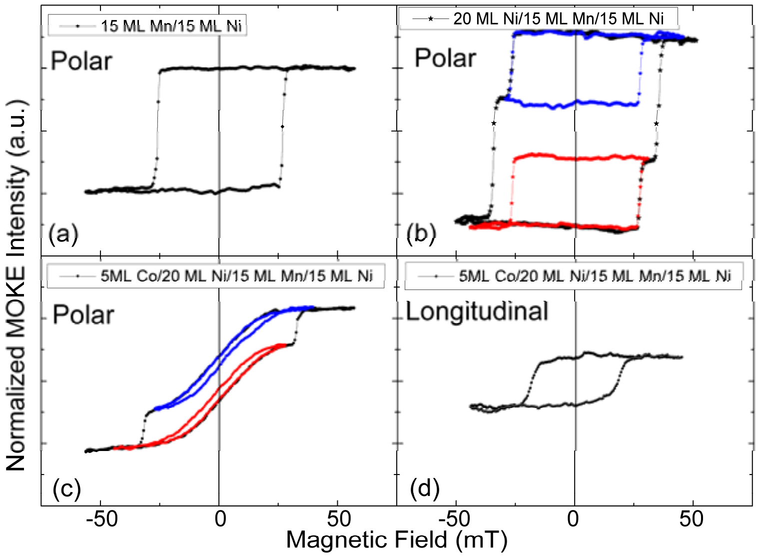

Figure 4. 8 Hysteresis loops measured by polar (a, b, c) and longitudinal (d) (magnetic field aligned parallel to the in-plane [100] crystal direction) MOKE for bilayer, trilayer and four-layer at RT. Blue and red loops are the positive and negative field minor loop, respectively. (a), 15 ML Mn/15 ML Ni, (b) 20 ML Ni/15 ML Mn/15 ML Ni, (c-d), 5 ML Co/20 ML Ni/15 ML Mn/15 ML Ni.

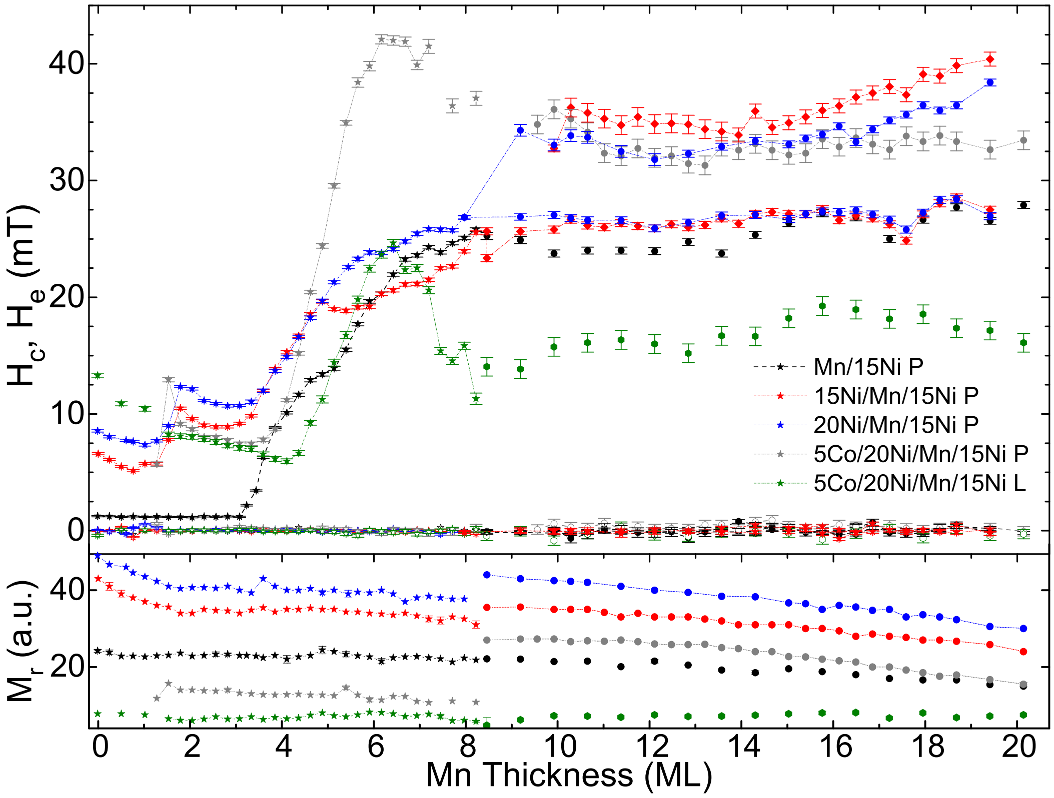

Figure 4. 9 Top: Coercivity H_c (solid symbols) and exchange bias field H_e (open symbols) of bilayer, trilayer, and four-layer samples as a function of Mn thickness (note here the longitudinal data for 5 ML Co/20 ML Ni/Mn/15 ML Ni in green color). Bottom: Kerr signal in remanence of the same samples.

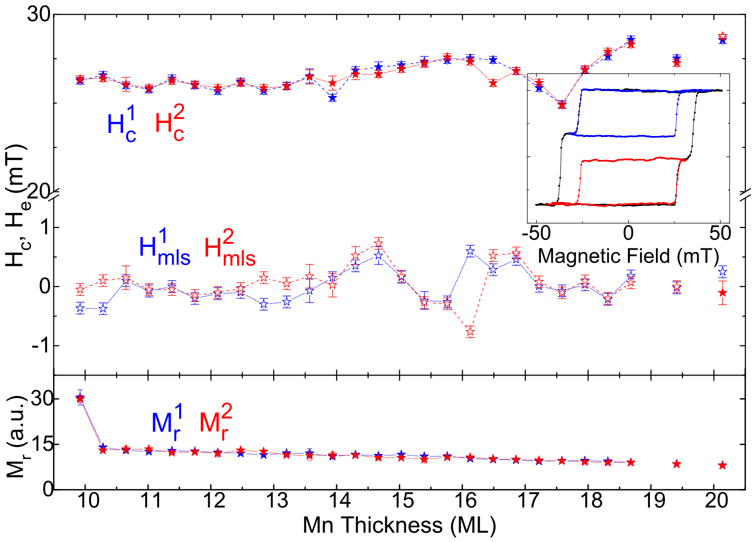

Figure 4. 10 Coercivity ($H^1{}_c$, $H^2{}_c$) and minor loop shift ($H^1{}_{mls}$, $H^2{}_{mls}$) for positive and negative minor loops for 15 ML Ni/Mn/15 ML Ni trilayers as a function of Mn thickness. Bottom: Kerr signal in remanence of the minor loops. The inset shows the loop for 15 ML Ni/10.3 ML Mn/15 ML Ni.

On bilayers with a Mn wedge (0-20 ML)/15 ML Ni/Cu(001), subsequently 15 (20, 25) ML Ni is deposited on top to form trilayers, finally by deposition of 5 ML Co four-layers have been prepared.

Multilayer films were prepared and measured layer-by-layer in order to study the interaction between the layers. Results are shown in this section. Selected magnetization loops are presented in Figure 4. 7 and Figure 4. 8. Coercivity H_c, exchange bias field H_e, and remanent Kerr signal versus Mn thickness are shown in Figure 4. 9.

First we talk about the Mn/15 ML Ni bilayer sample. Square loops are observed up to 20 ML Mn thickness, with H_c around 1.2 mT up to 3.2 ML Mn thickness. Then H_c sharply increases up to 25 mT at 8.5 ML Mn thickenss, after this H_c stays constant. Compared to the Mn/Co bilayer, there are two things we should point out. First, the t_{AFM} here (~ 3.2 ML) is smaller than in the Mn/Co case (~ 4.1 ML). Second, 15 ML Ni/Cu(001) should be very rough from the MEED data, so its H_c behavior should be similar to Mn/Co bilayers with half-integer number of atomic layers in the bottom Co layer. In these Mn/Co bilayers, the H_c of rougher bottom Co layer (8.5 or 10.5 ML) decreased rapidly after the maximum at around 6 ML Mn thickness. Here the H_c of Mn/15 ML Ni is nearly the same as in Mn/10.0 ML or 8.0 ML Co bilayers.

15 ML Ni were deposited on top of the Mn/Ni bilayer in order to investigate the interlayer coupling of two out-of-plane-magnetized Ni layers through the AFM Mn space layer. Below 2 ML Mn thickness, the Ni/Mn/Ni trilayers show a low H_c and higher M_r compared to the data above 2 ML Mn thickness. This could be due to the structural relaxation of the strained Ni layer by the appearance of misfit dislocations at the higher total Ni thickness. The jump of H_c starts from 1 ML Mn thickness, which could come from the two interface surfaces between the top Ni and Mn, bottom Ni and Mn layers induced by the Mn spacer layer. Another possibility of higher H_c could come from the coherent Mn atoms when the Mn layer reaches 1 ML thickness. H_c increases from 3.2 ML Mn thickness, and shows three steps of increment at around 5 ML and 6.2 ML Mn thickness. Two separate steps in the loops are observed above 10 ML Mn thickness. The bottom Ni layer shows the lower H_c, which is the same as in Mn/Ni data, whereas the upper Ni layer has a higher H_c. Both of them stay more or less constant at higher Mn thicknesses in our sample. Putting 5 ML more Ni on top gives the similar results, except for two differences. One is that the first and second increase of H_c with Mn thickness are the same as for the 15 ML top layer. Another is that the separate step in the magnetization loops related to the top Ni layer shows a low H_c due to thicker FM layer.

Let us now compare the results of bilayer Mn/Ni, trilayer Ni/Mn/Ni, and four-layer Co/Ni/Mn/Ni.

First, Mn/Ni bilayer shows the lowest H_c in these samples in the Mn thickness range between 2 and 3 ML, which can be explained by two results. a) the top out-of-plane Ni layer has a higher H_c in Ni/Mn/Ni, this is confirmed later by the separated steps in loops in which the top Ni layer shows a higher H_c than the bottom one due to the smoother bottom interface between Ni/Mn layers. b) the H_c of the top layer of trilayer samples with 20 ML Ni is higher than for a 15 ML Ni layer, this can be attributed to the influenced more misfit dislocations in the thicker Ni layer.

Second, both 15 ML and 20 ML Ni/Mn/Ni show the similar t_{AFM} at about 3.3 ML Mn thicknessas compared to the Mn/Ni bilayer (3.2 ML). This is different to the bottom Co layer case, in which the t_{AFM} of the trilayers (Co/Mn/Co and Ni/Mn/Co) is higher than in the bilayer (Mn/Co).

Finally, 5 ML Co were deposited on top to study the interaction between the in-plane-magnetized top layer and the out-of-plane-magnetized bottom layer. The polar signal starting from 1.3 ML Mn thickness indicates that at this Mn thickness the two FM layers are sufficiently decoupled to enable the out-of-plane magnetization of the bottom Ni layer independently from the in-plane top layer. H_c is around 8 mT before the onset of AFM order in Mn, a slightly higher value for t_{AFM} of around 3.8 ML is observed, after which the coercivity increases abruptly. After passing the maximum peak (42 mT at 6.5 ML), H_c reduces slowly and keeps a constant value of around 32 mT between 10 and 20 ML Mn thickness. This coercivity is higher than that of Mn/15 ML Ni as well as that of the bottom layer of 15 ML Ni/Mn/15 ML Ni. This higher H_c could be attributed to canted spins in Mn or in the bottom Ni layer induced by the coupling to the in-plane Co layer.

Longitudinal MOKE was used to measure the in-plane signal in 5 ML Co/20 ML Ni/Mn/15 ML Ni. A higher t_{AFM} of about 4.4 ML is observed, after which H_c increases up to 25 mT at 6.5 ML Mn thickness, then decreases to around 15 mT at 10 ML Mn thickness. This behavior of H_c is similar to Co/Mn/Co trilayers with half-integer number of atomic layers in the bottom Co layer.

Figure 4. 10 presents the results from minor loop measurements of a 15 ML Ni/Mn/15 ML Ni trilayer as a function of Mn thickness. It shows that H_c, H_{mls}, and M_r are nearly constant, independently of the Mn thickness. Compared to the oscillatory behavior of H_c, H_{mls}, and M_r in Co/Mn/Co samples, for example Figure 3. 22, RKKY-type or direct exchange coupling is not observed in this Ni/Mn/Ni trilayer sample.

4.4 Summary

We now compare the results from the last two sections, i.e., Co/Ni/Mn wedge/10 ML Co and Co/Ni/Mn wedge/15 ML Ni, while the Co/Mn wedge/10.0 ML Co trilayer serves as a reference. In the following, P and L mean polar MOKE and longitudinal MOKE, respectively.

We divide the discussion into three parts with respect to the thickness of Mn. 1) $0 < t_{\mathrm{Mn}} < {\sim}4$ ML, the Mn is in FM and FM-AF phase; 2) $\sim 4 < t_{\mathrm{Mn}} < {\sim}9$ ML, the coercivity starts to increase in this thickness range due to the AFM order of Mn; 3) $\sim 9 < t_{\mathrm{Mn}} < {\sim}20$ ML; the coercivity stays constant independent from the Mn thickness, independent switching of the two FM layers is observed in this thickness range.

1. $0 < t_{\mathrm{Mn}} < {\sim}4$ ML

a) Bilayer, Mn/15 ML Ni (P) and Mn/10.0 ML Co (L):

The coercivity is constant in this Mn thickness range for Mn/15 ML Ni (~ 1.2 mT) and Mn/10.0 ML Co (~ 1.2 mT) bilayers. A slightly higher H_c around 1.5 mT is found at Mn thicknesses between 3 ML and 3.5 ML, probably due to the FM-AF phase coexistence in the Mn layer, as described for Mn/Co bilayers by Caminale' group.[102]

b) Trilayer, 20, 15 ML Ni/Mn/15 ML Ni (P), 15 ML Ni/Mn/10.0 ML Co (P and L), 10 ML Co/Mn/10.0 (10.5) ML Co (L):

The 15 (20) ML Ni/Mn/15 ML Ni trilayer shows a higher H_c in 0 - 1.5 ML [5.6 (7.6) mT] and 1.5 - 3 ML [9 (10.8) mT] Mn thickness range. The loop of 15 ML Ni/Mn/10.0 ML Co (P) starts from 2 ML Mn thickness with a coercivity of around 5.5 mT. A slightly higher H_c is found between 3.5 ML and 4 ML Mn thickness, probably due to the FM-AF phase coexistence in the Mn layer. Below 2 ML Mn thickness no out-of-plane signal is observed because the Ni layer is strongly coupled along the in-plane direction by the Co bottom layer. 15 ML Ni/Mn/10.0 ML Co (L) and 10 ML Co/Mn/10.0 (10.5) ML Co (L) show similar loops as the respective bilayers. From the above results, for the out-of-plane direction (MOKE results), the top Ni layer increases H_c in the trilayers compared to the bilayers in (Ni/)Mn/Ni. This could be due to misfit dislocations or to the smoother interface between the top Ni and the Mn layers; for in-plane (MOKE results), the top Ni (Co) layer doesn't obviously change H_c in the trilayer compared to the Mn/10.0 ML Co bilayer, the slightly higher H_c in Co/Mn/Co could be attributed to misfit dislocations.

c) Four-layer, 5 ML Co/20 Ni/Mn/15 ML Ni (P and L), 3 ML Co/15 ML Ni/Mn/10.0 ML Co (L):

The polar signal in 5 ML Co/20 Ni/Mn/15 ML Ni starts from 1.5 ML Mn thickness with an H_c around 8 mT. This coercivity is much higher than in the Mn/15 ML Ni bilayer (~ 1.2 mT), but a bit smaller than in 15 (20) ML Ni/Mn/15 ML Ni [9 (10.8) mT]. We explain this assuming that the top 5 ML Co layer couples to the top 20 ML Ni and also the Mn layer, and this will change the spin configuration in the Mn layer, leading also to a change of the coupling between the Mn and the bottom Ni layer. Or the spins in the bottom Ni layer present a canted state, which would also change the coupling between the Mn and the bottom Ni layer and thus affect the coercivity. H_c decreases from 13 to 6 mT in the Mn thickness range from 0 to 4 ML in 5 ML Co/20 Ni/Mn/15 ML Ni in the longitudinal geometry, which is a similar H_c as in the polar measurements. 5 ML Co/15 Ni/Mn/10.0 ML Co shows nearly the same H_c (1 mT) as the corresponding bilayer or trilayer.

2. 4 ML < t_{Mn} < ~9 ML

a) Bilayer, Mn/15 ML Ni (P) and Mn/10.0 ML Co (L):

In the Mn/15 ML Ni bilayer, H_c starts to increase at around 3.2 ML Mn thickness indicating the onset of AFM order in Mn, via three shoulders (13.8 mT at 5 ML, 20 mT at 6.2 ML), to reach a maximum of 25.5 mT at 8.5 ML Mn thickness. Mn/10.0 ML Co shows a larger t_{AFM} of about 4.1 ML, and two shoulders (40.5 mT at 7 ML), then reaches a maximum of 50 mT at 8.5 ML Mn thickness.

b) Trilayer, 20, 15 ML Ni/Mn/15 ML Ni (P), 15 ML Ni/Mn/10.0 ML Co (P and L), 10 ML Co/Mn/10.0 (10.5) ML Co (L):

The Ni/Mn/Ni trilayer shows the same t_{AFM} of about 3.3 ML Mn thickness as the Mn/Ni bilayer. For the 15 ML Ni/Mn/10.0 ML Co, both the in-plane and the out-of-plane components show a larger t_{AFM} of about 4.7 ML compared to the corresponding bilayers (4.2 ML). This is also observed in the Co/Mn/Co system. It could be due to the interaction between the in-plane Co spin, out-of-plane Ni spin and in-plane Mn spin. Although J. T. Kohlhepp *et al.* showed that the 2D AFM ordered state of Mn does not depend on the spin direction of the FM films,[20] this point still needs more experiments and theoretical work in the future.

c) Four-layer, 5 ML Co/20 ML Ni/Mn/15 ML Ni (P and L), 3 ML Co/15 ML Ni/Mn/10.0 ML Co

(L):

After depositing 5 ML Co on 20 ML Ni/Mn/15 ML Ni, we would expected the polar MOKE signal only from the Mn/15 ML Ni bottom part of the sample and shown the same behavior to Mn/15 ML Ni bilayer. However, the H_c strikingly increases at Mn thicknesses above 3.8 ML to the maximum (42 mT) at 6.4 ML Mn thickness. The H_c from the in-plane component presents a similar behavior as that of the out-of-plane component, where H_c reaches a maximum (24 mT) at 6.4 ML Mn thickness before decreasing for further increasing Mn thickness. A bit larger t_{AFM} is found of about 3.8 ML Mn thickness compared to bilayer or trilayer. For the 3 ML Co/15 ML Ni/Mn/10.0 ML Co sample, a larger t_{AFM} and an even lower H_c are observed compared to top 10 ML or 15 ML Co layer on Mn/10.0 ML Co. This indicates that the presence of the Ni layer decreases the H_c in the Co/Ni/Mn/Co sample.

Let us now talk about t_{AFM} in the above samples:

In the bilayer case, Mn/15 ML Ni shows a smaller t_{AFM} (~ 3.2 ML) than Mn/10.0 ML Co (~ 4.1 ML), but has a similar value to Mn/10.5 ML Co bilayer (~ 3.4 ML), as shown in Table 4. 1. In previous experiments on Mn/20 ML Co/Cu(001) and Mn/2 ML Co/14 ML Ni/Cu(001),[97] it has been reported that t_{AFM} of Mn is 2.5-2.6 ML for both systems at RT. From this result, it is shown that the critical thickness for the formation of AFM order in Mn does not change if the magnetization direction of the FM layer is changed from in-plane to out-of-plane. The authors of Ref. 97 state that the 2 ML Co in Mn/2 ML Co/14 ML Ni/Cu(001) prevent direct contact of Mn with Ni and thus the possible formation of unwanted NiMn alloys and ill-defined growth. Compared to our results, Mn/15 ML Ni has a similar t_{AFM} to Mn/10.5 ML Co, which is consistent to Mn/20 ML Co/Cu(001) and Mn/2 ML Co/14 ML Ni/Cu(001) in Ref. 97. As we discussed in the sec. 3.2.3, both Mn/10.5 ML Co and Mn/20 ML Co bilayers show a similar coercivity behavior with increasing Mn thickness, and explained by assuming a similar interface roughness of our 10.5 ML and the 20 ML Co layers in Ref. 97. However, the Mn/10.0 ML Co shows a higher t_{AFM}, this could be related to the interface roughness, i.e., the smoother interface will change more the effective Mn thickness, leading to a higher t_{AFM}.

Compared to the results of FeMn with a 3D spin structure, a shift of 3-4 ML of t_{AFM} value of FeMn layer by changing the Ni FM layer from out-of-plane to Co in-plane magnetization was found.[105] The explanation is that both the spins in Ni and Co layer couple to the spins in the FeMn layer with different exchange coupling. For our results, one explanation is similar to FeMn's results, that the spin structure in Mn/FM is changed by intermixing at the interface, dependent on the magnetization direction in the FM layer, i.e., in the Ni and Co layer. And this effect strength dependents on the interface roughness, i.e., the Mn/10.0 ML Co has a higher t_{AFM} than Mn/10.5 ML Co bilayers, which means that the effective Mn thickness is reduced more by the coupling to the filled topmost atomic layer of Co layer. Another possibility is that a NiMn alloy is formed at the Ni/Mn interface, and that this leads to a shift of t_{AFM} of the Mn layer.

Samples	t_{AFM} (ML)
Mn/10.5 ML Co/Cu(001)	3.4 (L)
10 ML Co/Mn/10.5 ML Co/Cu(001)	4.1 (L)
Mn/10.0 ML Co/Cu(001)	4.1 (L)
10 ML Co/Mn/10.0 ML Co/Cu(001)	4.8 (L)
15 ML Ni/Mn/10.0 ML Co/Cu(001)	4.7 (P), 5.0 (L)
Mn/15 ML Ni/Cu(001)	3.2 (P)
15 ML Ni/Mn/15 ML Ni/Cu(001)	3.3 (P)
5 ML Co/20 ML Ni/Mn/15 ML Ni/Cu(001)	3.8 (P), 4.4 (L)

Table 4. 1 The obtained onset of antiferromagnetic order in the Mn layer (t_{AFM}) for the different systems in this thesis at RT

If the bilayer is Mn/10.0 ML Co, a top Co layer will increase t_{AFM} for the trilayer in-plane component, and a top Ni layer will also increase t_{AFM} of the trilayer for both the in-plane and the out-of-plane component. If the bilayer is Mn/15 ML Ni, the top Ni does not shift t_{AFM} of the trilayer, whereas t_{AFM} is upshifted in 5 ML Co/20 ML Ni/Mn/15 ML Ni both in longitudinal and polar MOKE. Table 4. 1 presents different t_{AFM} from the studied systems.

In the trilayer Co/Mn/Co case, the higher t_{AFM} is found than their bilayer case, this can be explained by that two side of Mn surfaces coupled by Co layer. However, in the Ni/Mn/Ni sample, the similar t_{AFM} is observed compared to Mn/Ni bilayer. And we know that the top Ni and Mn interface is smoother than Mn and bottom Ni case from the MEED results (Figure 3. 1). Even in this case, the t_{AFM} doesn't upshift in the Ni/Mn/Ni trilayer. We can conclude that the Mn and adjacent Ni layer has less coupling than that of Co layer, and this coupling is independent on the surface roughness of the Mn and Ni interface.

From the above discussion about t_{AFM}, a) The coupling between the Mn and adjacent FM film is dependent on the in-plane or the out-of-plane magnetization in the FM layer. The higher t_{AFM} is found in Mn/Co than the Mn/Ni bilayer, this could be due to the in-plane spins in Co layer is more efficient to reduce the effective Mn thickness by alloying or proximity effects at the interface. b) This interface effect is more obviously in the smoother surface between Mn and Co layers, i.e., the onset of antiferromagnetic order of Mn starts later in filled topmost atomic layer of bottom Co film.

3. 9 ML < t_{Mn} < 20 ML

a) Bilayer, Mn/15 ML Ni (P) and Mn/10.0 ML Co (L):

Above 9 ML Mn thickness, H_c is independent of the Mn thicknes.

b) Trilayer, 20, 15 ML Ni/Mn/15 ML Ni (P), 10 ML Co/Mn/10.0 ML Co (L):

Two separate steps are observed in the loops of 20 (15) ML Ni/Mn/15 ML Ni. The one with lower switching field, with the same H_c as in Mn/Ni, is corresponding to the bottom Ni layer, the higher H_c comes from the top Ni layer. However, this is opposite for 10 ML Co/Mn/10.0 ML Co, where the lower H_c arises from the top Co layer. This is attributed to the interface roughness between the FM and Mn layers. The MEED [Figure 3. 1: Co/Cu(001) and Mn/Co/Cu(001), Figure 4. 3: Ni/Cu(001) and Ni/Mn/Ni/Cu(001)] and LEED [Figure 3. 2: Mn/Co/Cu(001)] results show that the interface roughness between bottom Co and Mn layers is smoother than that of the top Co/Mn interface, whereas this is opposite for the Ni/Mn/Ni trilayers. The above results confirm that in the FM/Mn/FM system, the FM layer with smoother interface between FM and Mn shows the higher coercivity than the FM layer with the rougher interface.

c) Four-layer, 5 ML Co/20 ML Ni/Mn/15 ML Ni (P and L):

In the polar MOKE loops, the H_c of 5 ML Co/20 ML Ni/Mn/15 ML Ni is higher than that of the Mn/15 ML Ni bilayer. This could be due to a change of the Mn spin direction induced by the coupling to the in-plane-magnetized Ni/Co layer. This could lead to the changed coercivity of the bottom Ni layer in the Co/Ni/Mn/Ni sample compared to the Mn/15 ML Ni bilayer. In the longitudinal MOKE measurement, H_c is low, which is similar to the Co/Mn/Co or Co/Ni/Mn/Co data.

Chapter 5 Magnetic characterization of Co/Ni and Co/Fe_xMn_{1-x} bilayers

Control of fast magnetization reversal dynamics on microscopic lengthscales is an important topic for many technological applications. The basic mechanisms governing the precessional dynamics in coupled bilayers after optical excitation are only partly understood. As the effective is changed, the system will start to precess. For the Co wedge/Ni bilayers on Cu(001) as we used, the magnetization direction of FM layer depends on the competing magnetic anisotropies, namely perpendicular anisotropy in the Ni layer, and in-plane anisotropy in the Co layer.[117] The spin-reorientation transition (SRT) region from out-of-plane to in-plane magnetization will be formed with Co thickness increasing. The effective field is sensitive close to the SRT due to the metastable. The excitation by a fs laser pulse leads to changes in the magnetic properties of the sample such as magnetization, magnetic anisotropy, or interlayer coupling,[118-120] which will change the effective field within the system.

In this chapter, experiments done at BESSYⅡ with the Elmitec PEEM installed on beamline UE49-PGM-A will be presented. They cover the static and dynamic magnetic properties of Co/Ni and Co/Fe_xMn_{1-x} bilayers. Using the XMCD-PEEM, domain images from the FM layers were obtained, while magnetization dynamics was studied using PEEM with time-delayed pump (fs laser) –probe (X-ray) measurements. In particular, the effect of laser excitation close to a SRT is investigated, with the aim to explore the precessional motion of the magnetization. Domain structures, effect of laser irradiation, and laser-induced dynamics close to the SRT in the Co/Ni bilayer are presented in sec. 5.1, along with the result of micromagnetic simulations. In sec. 5.2, we focus on the static magnetic properties and the consequences of thermal treatments on Co/Fe_xMn_{1-x} bilayers.

5.1 Co wedge/15 ML Ni/Cu(001) bilayers

5.1.1 Magnetic domain configuration

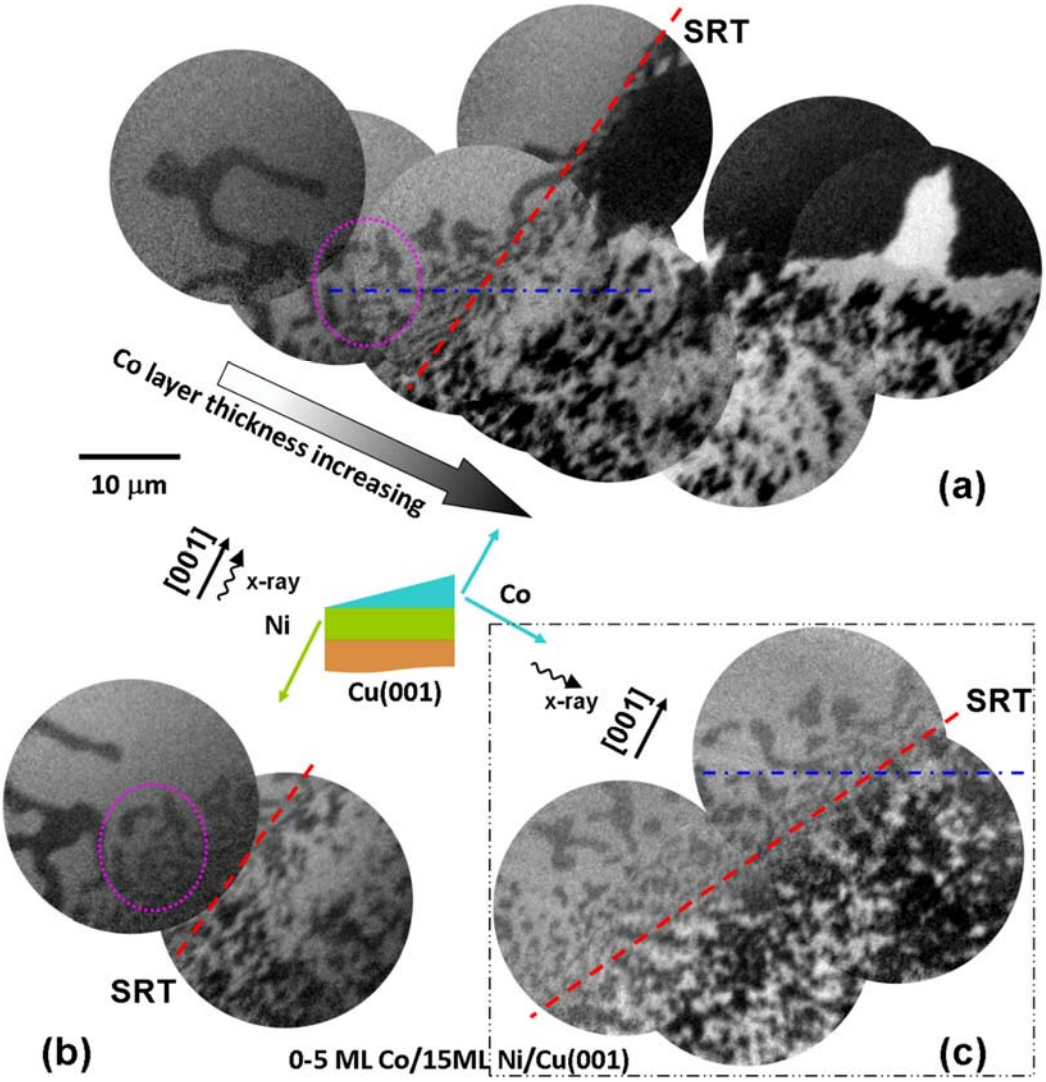

Figure 5. 1 Domain pattern close to the SRT in Co/Ni/Cu(001). (a) Magnetic domain image at the Co L_3 edge, (b) at the Ni L_3 edge, (c) at the Co L_3 edge for 90° different incidence azimuth. Red dashes lines indicate the SRT, pink ellipses in (a), (b) and blue lines in (a), (c) indicate the same region. The big arrow shows the direction of the Co layer thickness wedge.

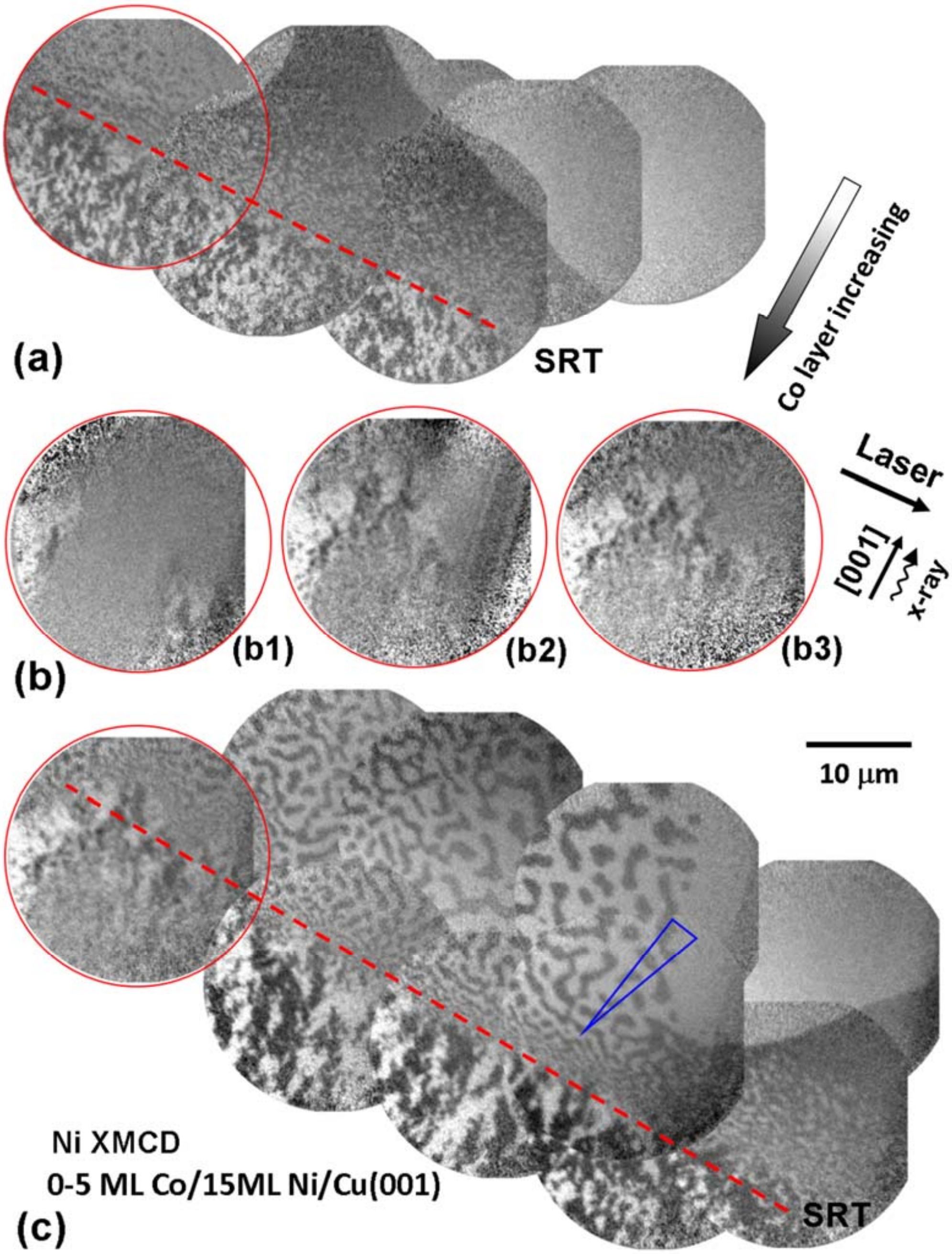

Figure 5. 2 Effect of laser irradiation on the magnetization of the Co/Ni bilayer imaged at the Ni L_3 edge. (a) no laser, (b) domain pattern is erased by strong laser irradiation, b1: 0.85 W, b1: 0.85 W only right side, b1: 0.45 W only right side, (c) magnetization pattern recovery after laser irradiation. Red circles mean the same region, red dashes lines indicate the SRT, and the blue triangle presents the direction of shrinking domain size near to the SRT.

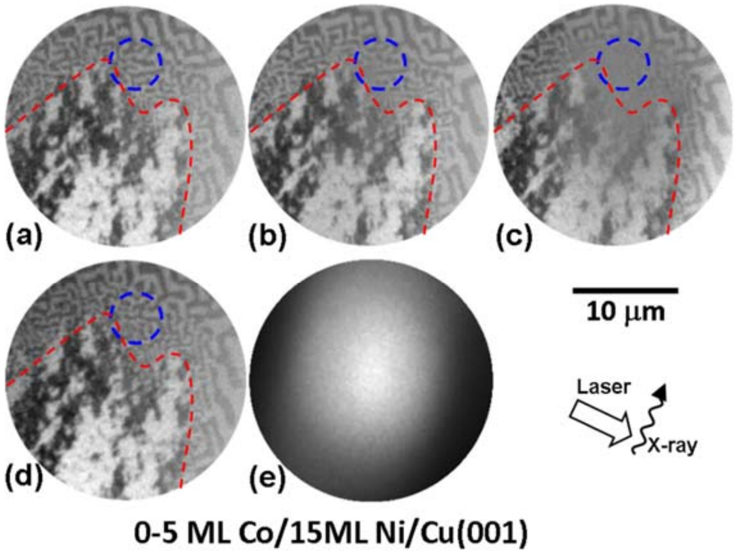

Figure 5. 3 Effect of laser irradiation on the magnetization of the Co/Ni layer close to the SRT imaged at the Co L_3 edge. (a) image before exposure to the laser pulses, (b) with laser power of 0.30 W, (c) laser power 0.35 W, (d) after removing the laser spot from the sample, (e) image of electrons emitted by laser for 0.35 W. Red line means the SRT, magnetization in left bottom part is in-plane while is out-of-plane in the rest part, and blue circles indicate the same region.

A Co wedge/15 ML Ni/Cu(001) bilayer sample was prepared at RT and then transferred to the PEEM. The domain configuration of the as-grown state at a Co thickness of 0-5 ML is shown in Figure 5. 1. Figure 5. 1 (a) shows the XMCD images at the Co L_3 absorption edge. In the imaged area the Co thickness increases from left top to right bottom as indicated. Domain structures at the Ni L_3 edge were also obtained at the same region, see Figure 5. 1 (b). The pink ellipses in Figure 5. 1 (a) and (b) point out the same position in the Co/Ni bilayer, as imaged for Co and Ni domains. The Co and Ni images show the same domain structures, which means the two FM layers are strongly magnetically coupled to each other. The XMCD contrast change along the Co wedge near to the red lines [clearly seen in Figure 5. 1 (a)], which indicates the spin reorientation transition. 加 The sample was then rotated by 90º (in-plane) to image the same region at Co L_3 edge as shown in Figure 5. 1 (c). Compared to the blue lines in Figure 5. 1 (a) and (c), it shows that the domain contrast is the same on the left side of the red line, while it is different on the other side. This confirms that the magnetization to the left of the red line is perpendicular to the film plane ("out-of-plane"), while on the other side the magnetization is in the film plane ("in-plane"). Because the XMCD asymmetry depends on the angle between the incident X rays and the magnetization direction, the contrast of the in-plane magnetization changes while the out-of-plane magnetization is not changed during sample rotation, so the changed domain contrast confirms in-plane magnetization.

When the Co layer thickness is increased, the coupled magnetization of the Co/Ni bilayer changes from out-of-plane to in-plane. This can be easily understood by the competition of the anisotropies of the Co and Ni layers. 15 ML Ni have an out-of-plane magnetization on Cu(001), while Co prefers the in-plane magnetization. Co has also a larger magnetic moment than Ni, such that the contribution of Co will increase the shape anisotropy with increasing Co layer thickness, and the magnetization will start to rotate from out-of-plane to in-plane at a critical Co layer thickness, shown as red lines in Figure 5. 1. The XMCD contrast of the in-plane domains is stronger than that of the out-of-plane domains. This is because the X rays hit the sample under a 17^{o} grazing angle, which make the XMCD contrast more sensitive to the in-plane magnetization. This also helps to distinguish the magnetization direction in domain structures. On the right bottom side of Figure 5. 1 (a), there are small size of domains this could be due to the roughness of substrate.

5.1.2 Effect of laser irradiation

Now we see how the domain structures are influenced by the heating by the laser. Figure 5. 2 (a) shows domain structures of the Co/Ni bilayer imaged at the Ni L_3 edge. A sharp change of the domain pattern at the critical Co layer thickness for the SRT is marked by red lines in the picture. Smaller in-plane and bigger out-of-plane domains lay on each side of the SRT. Then the laser spot with size of a 20 μm × 40 μm was moved to sample, centered in the region as labeled by the red circle. Figure 5. 2 (b1) was obtained during exposure to the laser with power of 0.85 W. Strong laser irradiation erases the magnetic domain pattern. When the laser is shifted such as to leave the left half of the field of view without laser irradiation, the domain structure in the left hand side comes back, while no domains are seen in the right hand side in Figure 5. 2 (b2). Then the laser power was reduced to 0.45 W. In this case also at the right hand side domains are recognized [Figure 5. 2 (b3)]. After turning off the laser, the domain structure around the laser exposure region was imaged again and is shown in Figure 5. 2 (c). Compared to the as-grown domain structure in Figure 5. 2 (a), for the in-plane region, the domains became bigger after laser heating. For out-of-plane, the previous bigger domains divide into smaller domains, and the size of domains is larger when their position is more far away from the laser irradiation position, in other words smaller domains are formed along the increasing temperature gradient.

We focus now on the effect of laser irradiation in the region close to the SRT. In Figure 5. 3 (a), the as-grown Co wedge/15 ML Ni bilayer was imaged at the Co L_3 edge. Red lines indicate the SRT. The stripe domain pattern with out-of-plane magnetization changes to big domains with in-plane magnetization with increasing thickness of the Co layer. Now the laser is put on the sample. An image of the electrons emitted by the laser for 0.35 W is shown in Figure 5. 3 (e), where the laser spot is at the center of the field of view. Figure 5. 3 (b) presents the Co L_3 XMCD image with a laser power of 0.3 W. Comparing the same region marked by a blue circle in Figure 5. 3 (a) and (b), a few domains have disappeared in the lower part of the blue circle, while some domains became dim in the upper part. When the laser power is increased to 0.35 W, the magnetic domain pattern in the center is totally erased due to the heating by the laser. After removing the laser, the domain pattern reappears as shown in Figure 5. 3 (d).

5.1.3 Laser-induced magnetization dynamics

We now turn to the time-resolved investigation of the magnetization dynamics close to the SRT in the Co/Ni films on Cu(001). The position of interest is shown in Figure 5. 4 (d). The two magnetic layers are rigidly coupled to each other by direct exchange. The thickness of the Co layer increases from right top to left bottom, leading to a change of the easy axis of magnetization of the bilayer from out-of-plane to in-plane. Red lines indicate the SRT. Figure 5. 4 (d) shows a static domain image at the Co L_3 edge of 1-3 ML Co/15 ML Ni/Cu(001). After locating the SRT, the laser spot is moved on this area. From the image of the electrons emitted by the laser in Figure 5. 4 (c) it is seen that most of this area is covered by the laser spot. The next task is to find the suitable laser power. The domains are erased if the power is too high, as shown in Figure 5. 4. On the other hand, the power should be above a critical value, otherwise no dynamics will be detected. Once all these things are prepared, the experiment can be started.

Figure 5. 4 (d), (e), and (f) present domain images at delay times -0.13, 0.0, and 1.0 ns, respectively. The reduction of the magnetic contrast at delay zero shows the ultrafast demagnetization of the Co/Ni films by the laser pulses. At delay zero the laser and the X-ray pulses

hit the sample at the same time. The domain structure recovers at later delay times. As an example the image at 1.0 ns is shown in Figure 5. 4 (f).

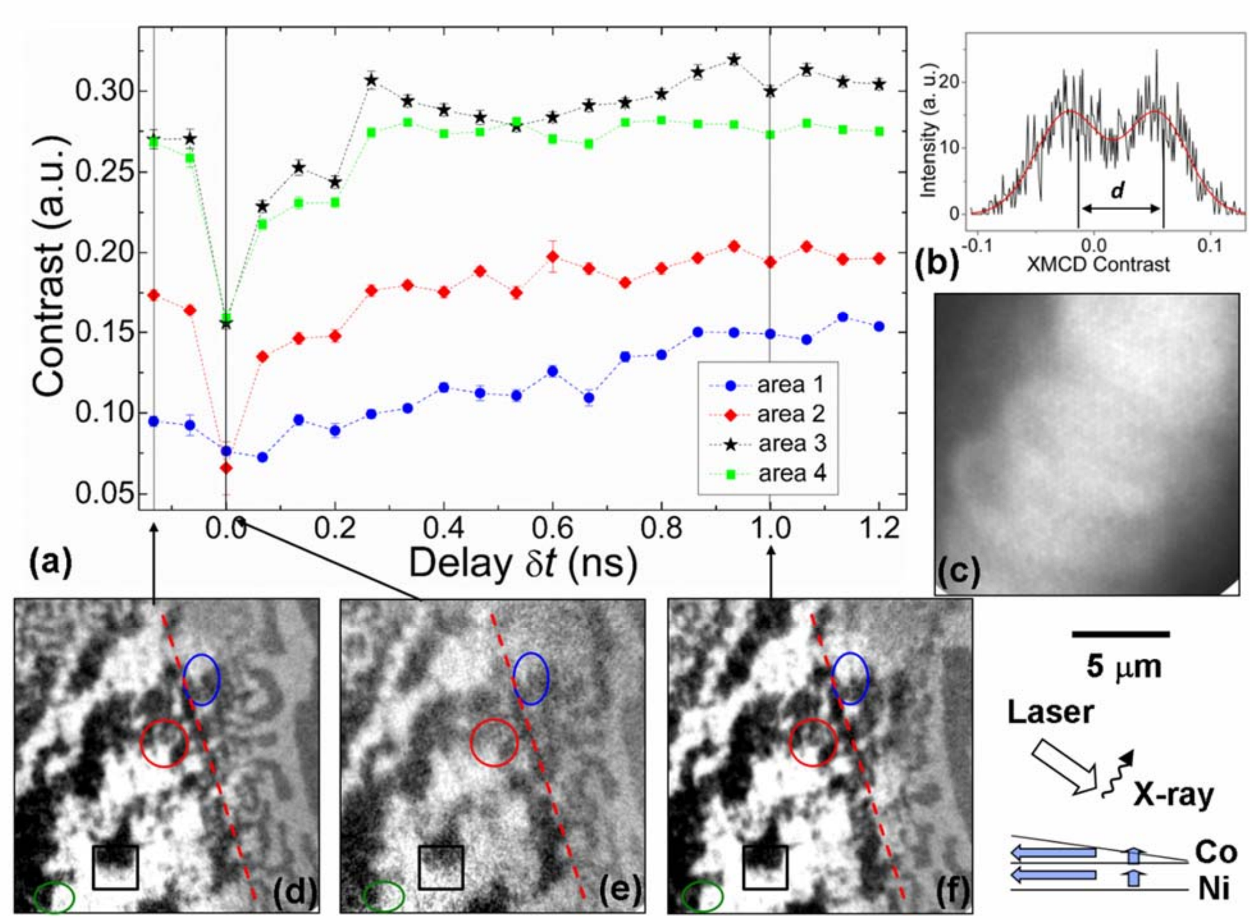

Figure 5. 4 Time-resolved magnetization dynamics close to the SRT in Co/Ni/Cu(001). (a) XMCD contrast of four areas as a function of delay time for a laser power of 0.38 W. Area 1, canted magnetization at the SRT; area 2, in-plane magnetization close to the SRT; areas 3 and 4, far from the SRT, in the in-plane region. (b) Example of histogram data from a given area, (c) image of electrons emitted by the laser at 0.38 W power, (d-f) Co XMCD magnetic domain images at delay times -0.13, 0.0, and 1.0 ns. Red lines in the XMCD images indicate the SRT, the magnetization in the left part is in-plane, while it is out-of-plane in the rest of the image.

We chose four different areas to analyze the time-resolved data. The temporal response to the fs laser of the local magnetization in the marked areas is shown in Figure 5. 4 (a). The data points represent the XMCD contrast between the two oppositely magnetized domains, extracted from histogram plots like the one shown in Figure 5. 4 (b). The magnetization in area 1 is canted as the XMCD contrast is lower than in the in-plane case. The blue data points for area 1 show that the contrast does not changed much at delay zero, and the magnetization recovers slowly as a function of time [Figure 5. 4 (a)]. Area 2 near to the SRT presents an obvious demagnetization at delay zero, and then the magnetization recovers slowly, as in area 1. Areas 3 and 4 are in the in-plane region and far away from the SRT. Also here a demagnetization is found at delay zero, but then a faster recovery is present in these data. The contrast from the out-of-plane areas mainly show a steady change with delay time.

5.1.4 Micromagnetic simulations

In order to understand the experimented results, micromagnetic simulations using the OOMMF code[121] with two-dimensional periodic boundary conditions[122] were performed. These consist of time-dependent micromagnetic simulations using the Landau-Lifshitz-Gilbert equation with a two-temperature model, following the procedure described in Ref. 78, to simulate the laser-induced magnetization dynamics.

First, we assume a Gaussian shape of 50 fs duration and different fluences for the laser pulse. During the laser-induced demagnetization, the external excitation is transferred into several subsystems. We assume a single channel in which the photon energy is transferred to the electrons and from there to the lattice. The magnetization is assumed to be coupled to the electron temperature T_e within a two-temperature model,[123]

$$C_e \frac{dT_e}{dt} = -G_{el}(T_e - T_l) + P(t),$$

$$C_l \frac{dT_l}{dt} = G_{el}(T_e - T_l)$$

where C_e and C_l are the electron and lattice specific heat constants, G_{el} is a coupling constant, and $P(t)$ is the laser fluency. Here we assume as a simplification $C_e = \gamma T_e$ and $\gamma = 3.8\times10^3$ J m^{-3} K^{-1}, $C_l = 2.8\times10^6$ J m^{-3} K^{-1}, $G_{el} = 1.8\times10^6$ W m^{-3} K^{-1}.[124] The $T_e(t)$ and $T_l(t)$ can then be determined from the above rate equations for given laser fluencies.

Second, the magnetization $M(t)$ can calculated in a mean-field approximation corresponding to the Curie temperature depending on the thickness of the film.

Third, the different magnetization leads to changes in the exchange stiffness A and the magnetic anisotropy K, modeled by approximate relations $K(t)\sim M(t)^3$ and $A(t)\sim M(t)^2$.[78]

The above values are all the input parameters used in the dynamic simulations. Here we show two examples. The first system is a 3 ML Co/15 ML Ni bilayer with a Curie temperature of 600 K[111] for both layers. The simulation size is 100×500×4 nm^3 (*x, y, z*) with cell size 2×2×1 nm^3, with 2D periodic boundary conditions in *x* and *y* directions. Material parameters used for Co and Ni are: saturation magnetization $M_s = 1.38\times10^6$ and 4.9×10^5 A/m,[125,126] exchange stiffness constant $A = 3\times10^{-11}$ and 9×10^{-12} J/m, and magnetocrystalline anisotropy constants $K_{\mathrm{cubic}} = 6.5\times10^4$ and $K_u = 2.9\times10^5$ $\mathrm{J/m}^3$,[125,127] $A = 1.95\times10^{-11}$ J/m for Co and Ni interface, respectively.

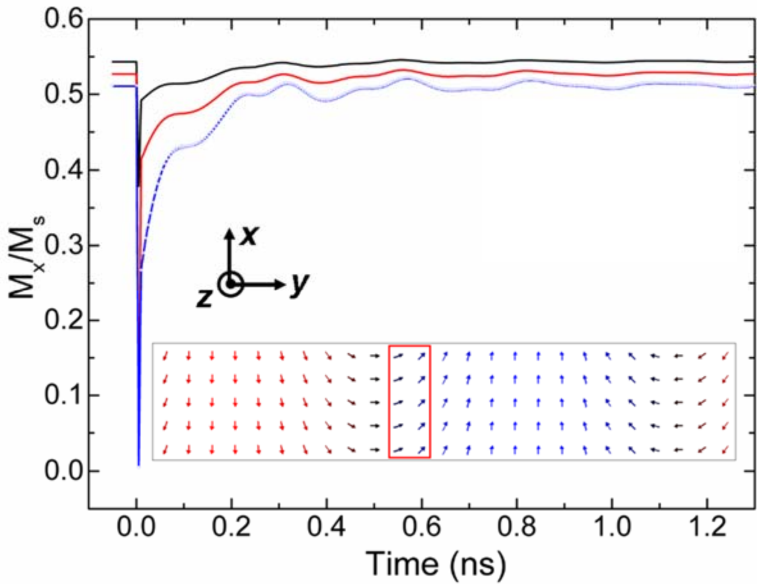

Figure 5. 5 Simulated magnetization dynamics of 3 ML Co/15 ML Ni/Cu(001) with two-dimensional periodic boundary conditions (*x*, *y*) for different maximum electron temperatures. Black and red curves are the data for the Co magnetization obtained for maximum electron temperatures of 500 K and 615 K, respectively. The blue and white curves present the results of both Ni and Co magnetization obtained for a maximum electron temperature of 750 K, respectively. The simulated curves are slightly vertically offset for clarity. The inset is the top view of the static spin state, red and blue colors indicate spins along the +*x* and –*x* direction.

The static magnetization of the system is shown in the inset of Figure 5. 5. The stripe domain direction is along the *x* direction, the size of the domain wall is about 100 nm, and the stripe width around 300 nm. The colored continuous lines in Figure 5. 5 show the results for the magnetization component along *x* integrated over the marked by a red rectangle in the inset. Different curves correspond to three different maximum electron temperatures reached during the laser excitation. From these simulation results, an oscillatory behavior becomes evident starting at about 200 ps after the laser pulse, which increases in amplitude for increasing laser power. For the highest laser power shown here, corresponding to a maximum electron temperature of 750 K, the simulation shows a similar behavior as the experimental result in area 4 [green curve in Figure 5. 4(a)]. Note that the simulations still need to be convoluted with the experimental time resolution determined by the synchrotron bunch width (about 50 ps) to compare to the experimental data close to time zero. Another thing is that the magnetization of Ni and Co layer show the same behavior, which indicate, that the two FM layers strongly couple to each other.

However, when comparing to the experiment, one has to keep in mind that the oscillation arises from the domain wall area, as marked in Figure 5. 5, while the areas of uniform magnetization do not show any oscillation, only the demagnetization at time zero (not shown here). In the experimental results, on the other hand, mainly the contribution from the magnetic domains is detected. So we can not compare these two results directly.

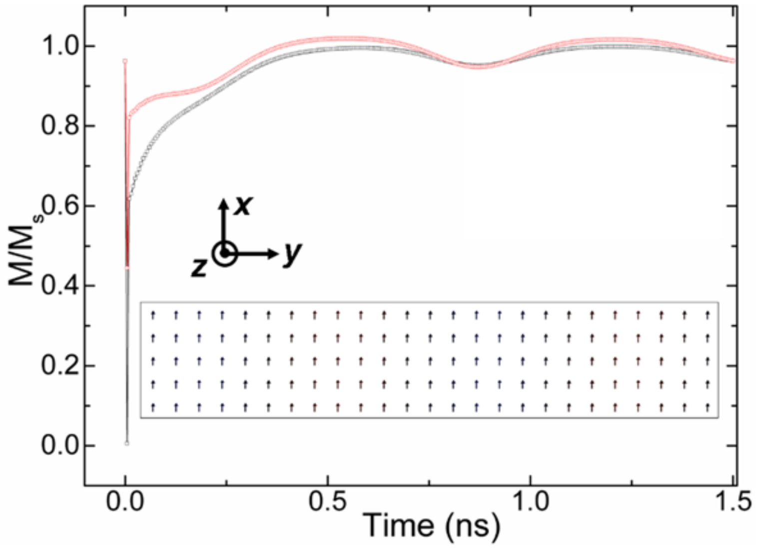

Figure 5. 6 Simulated magnetization dynamics with a maximum electron temperature of 508 K of 2.5 ML Co/15 ML Ni/Cu(001) with two-dimensional periodic boundary conditions in x and y directions for different Curie temperatures of the two layers (Co, 450 K; Ni, 540 K). Black and red curves are the data of Co and Ni magnetization obtained for the maximum electron temperature of 508 K, respectively. The inset shows a top view of the static spin state.

So what could be improved in the simulation? There is no external field during the measurement. One possibility is that the Ni and Co layers show a different response to the laser pulse. Therefore, we simulated a second system, in which the Co and Ni layers have different Curie temperatures. This leads to a different parameter gradient at the same temperature induced by the laser. The simulation process is the same like for the first one, only the parameters are different. The simulation size is 100×500×7 nm^3 (x, y, z) with cell size 2×2×1 nm^3, with 2D periodic boundary conditions in x and y directions. Material parameters used for Co and Ni are: saturation magnetization $M_\mathrm{s} = 1.38\times10^6$ and 4.9×10^5 A/m, exchange stiffness constant $A = 3\times10^{-11}$ and 9×10^{-12} J/m, and magnetocrystalline anisotropy constants $K_\mathrm{cubic} = 6.5\times10^4$ and $K_\mathrm{u} = 2.9\times10^5$ J/m^3, Curie temperature T_c = 450 and 540 K,[111] respectively. The inset in Figure 5. 6 shows the static magnetization of the bilayer. The magnetization dynamics of the Co and Ni layers is plotted as the magnetization as a function of time after the laser irradiation. The Co layer with the lower Curie temperature presents a slower magnetization recovery than Ni for the same maximum electron temperature. With decreasing influence of the demagnetization with time, the two layers became more strongly coupled to each other and show the same oscillation.

Now we talk about a possible origin of the oscillations. For the first simulated system as shown in Figure 5. 5, the parameters (M, A, K) are changed after the laser pulse. Their changes do not balance each other in the area around the SRT, the width of the domain wall will be changed. This region then starts a precession. For the second case, the two FM layers with different Curie temperatures as shown in Figure 5. 6, the spins in the two layers will reach the same temperature (between the two Curie temperatures) after the laser illumination. The spins in the layer with lower Curie temperature try to align randomly, while the magnetization in the layer with higher Curie temperatures tries to keep the previous state. By the coupling between these two layers they affect each other, such that the system starts a precession before eventually they will come back to the state before the laser illumination.

5.2 Co/Fe_xMn_{1-x} bilayers

Fe_xMn_{1-x} film was obtained by using the mixed $Fe_{50}Mn_{50}$ rod, the concentration of material can be checked by XAS. Co film deposits on the top of the Fe_xMn_{1-x}/Cu(001) in order to reduce the oxidation. Section 5.2.1 will discuss the Co, Fe, and Mn XMCD images for 8 ML Co/22 ML $Fe_{36}Mn_{64}$/Cu(001) in, and angle dependence of the Co XMCD in the 8 ML Co/28 ML $Fe_{40}Mn_{60}$/Cu(001) film. While sec. 5.2.2 will presents thermal treatments of 5 ML Co/25 ML $Fe_{54}Mn_{46}$/Cu(001) bilayer.

5.2.1 Magnetic domain configuration

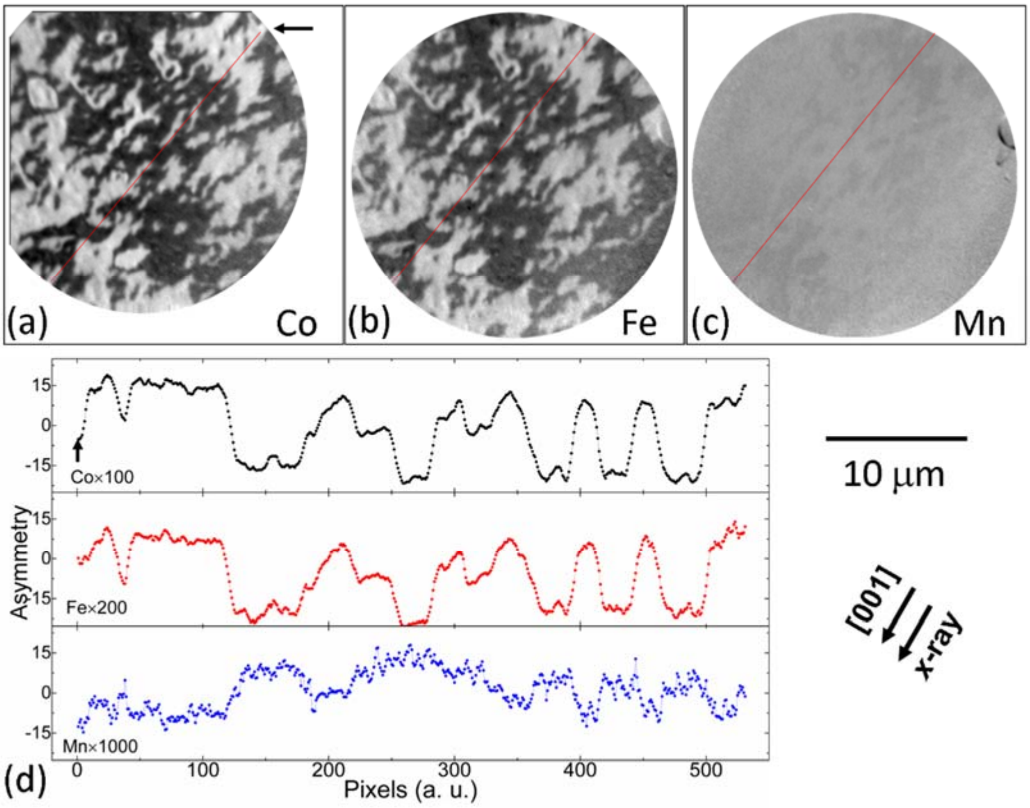

Figure 5. 7 (a-c) Co, Fe, and Mn XMCD domain patterns obtained at the respective L_3 edges of the same area of a 8 ML Co/22 ML $Fe_{36}Mn_{64}$/Cu(001) sample. (d) Line scans along the red line printed in each XMCD image after normalization to the same signal-to-background ratio as described in sec 4.1.2. The arrows in (a) indicates the beginning of the scans (note the different scales of the asymmetry data).

8 ML Co/22 ML $Fe_{36}Mn_{64}$ are prepared on Cu(001) and imaged by PEEM. The exposure time for all of the images was around 10 mins. Figure 5. 7 (a) shows the Co XMCD domain image. Small

domains are obtained in the as-grown bilayer due to the magnetic interaction between Co and $Fe_{36}Mn_{64}$. A ferromagnetic signal is also found for Fe and Mn, as shown in the Fe and Mn XMCD images in Figure 5. 7 (b) and (c). The Fe domain structures are the same as for Co, indicating that the uncompensated Fe moments are coupled to the Co layer. A comparison of line scans along a certain line in the Co and Fe images, is presented in Figure 5. 7 (d). The pixel scale is the same as for the corresponding domain image, the asymmetry of Fe is half value to Co data. Both Fe and Co asymmetry data shows three levels, indicating the three magnetization direction in the scanned position. The Mn XMCD image is shown in Figure 5. 7 (c), the contrast is really less compare to Co or Fe. The domain structures in Mn looks the same to Co but has the opposite magnetization direction. Blue data in Figure 5. 7 (d) presents the asymmetry scan in the same position to Co and Fe. The line shows the different sign compare to Fe and Co, indicating the antiferromagnetic couple to Fe and Co. Furthermore, the intensity is much less, which is 10 times smaller than Co case.

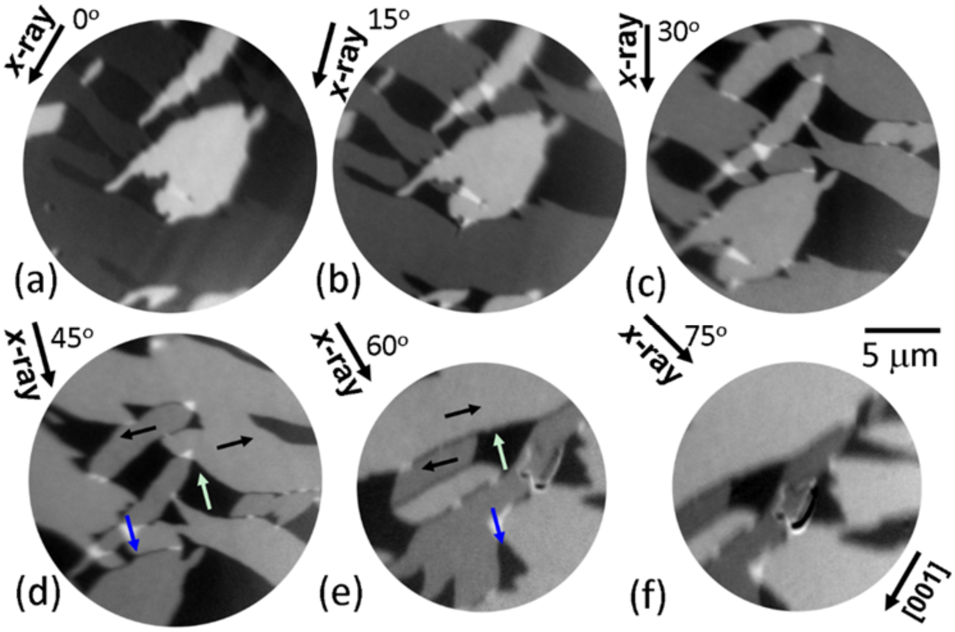

Figure 5. 8 Angle dependence of the Co L_3 XMCD images in 8 ML Co/28 ML $Fe_{40}Mn_{60}$/Cu(001) film. Arrows labelled X-ray show the direction of incoming X rays, arrows inside (d) and (e) indicate local magnetization directions. (a-d) shows the same position, while the (e) and (f) present the same position.

The angle dependence of the Co L_3 XMCD of the Co/Fe_xMn_{1-x} bilayer is measured in order to determine the magnetization directions of the domains of the Co layer. The 8 ML Co/28 ML $Fe_{40}Mn_{60}$/Cu(001) sample is used for this task. The direction of the crystallographic orientation of the Cu(001) substrate and the direction at the incoming X rays are shown in Figure 5. 8, in panel (a), the X-ray incidence is parallel to the [001] direction of the substrate, then the sample is rotated and an XMCD image is recorded each 15°. In these Co images, domains of four different magnetization directions are identified. The arrows in Figure 5. 8 (d) indicate the directions. The maximum XMCD contrast for domains marked by white and blue arrows is between Figure 5. 8 (c) and Figure 5. 8 (d), for which the angles between the X-ray incidence and the [001] direction of the substrate are 30° and 45°, respectively. This means the easy axis of magnetization of Co is along the [110] direction of Cu(001), which is the same as for Co on Cu(001). Here either the Co layer doesn’t couple sufficiently to $Fe_{40}Mn_{60}$, or the $Fe_{40}Mn_{60}$ is not in the AFM state in this sample.

5.2.2 Thermal treatments

As shown in Figure 5. 7 (a), a Co layer that grows on the thicker $Fe_{36}Mn_{64}$ film presents small domains due to the magnetic interaction. These small domains are a metastable states and will rearrange to larger domains to minimize the energy at a higher temperature. Here is an example for thermal treatments of Co/$Fe_{54}Mn_{46}$ bilayers. Co images are recorded during different temperatures on a 5 ML Co/25 ML $Fe_{54}Mn_{46}$/Cu(001) sample. Figure 5. 9 (a) shows the small domain structure of Co at RT. (b-h) are the images obtained at different temperatures during heating the sample. Each XMCD image needs around 5 mins, the sample position is somehow moving during the image acquisition due to the temperature increase. The sequence of images in Figure 5. 9 (a-h) shows that the small magnetic domains with white color become smaller and subsequently disappear. The number of small domains consequently decreases with increasing sample temperature. Images (i), (j), and (k) show difference images between the XMCD images presented in panels (a-b), (c-d), and (g-h), respectively. The white color indicates the disappearance of part of a white domain between the two images. It is clearly seen that small domains shrink at their edges. The size of small domains becomes smaller in this way with increasing temperature. In the end the smaller domains disappear completely, like the white dots in Figure 5. 9 (j), which correspond to disappearing domains between Figure 5. 9 (c) and (d). At a sample temperature of 430 K, as shown in Figure 5. 9 (h), there are only a few white domains left. After this thermal treatment, no domain structures on the whole sample were left at which the dynamic measurement could have been performed.

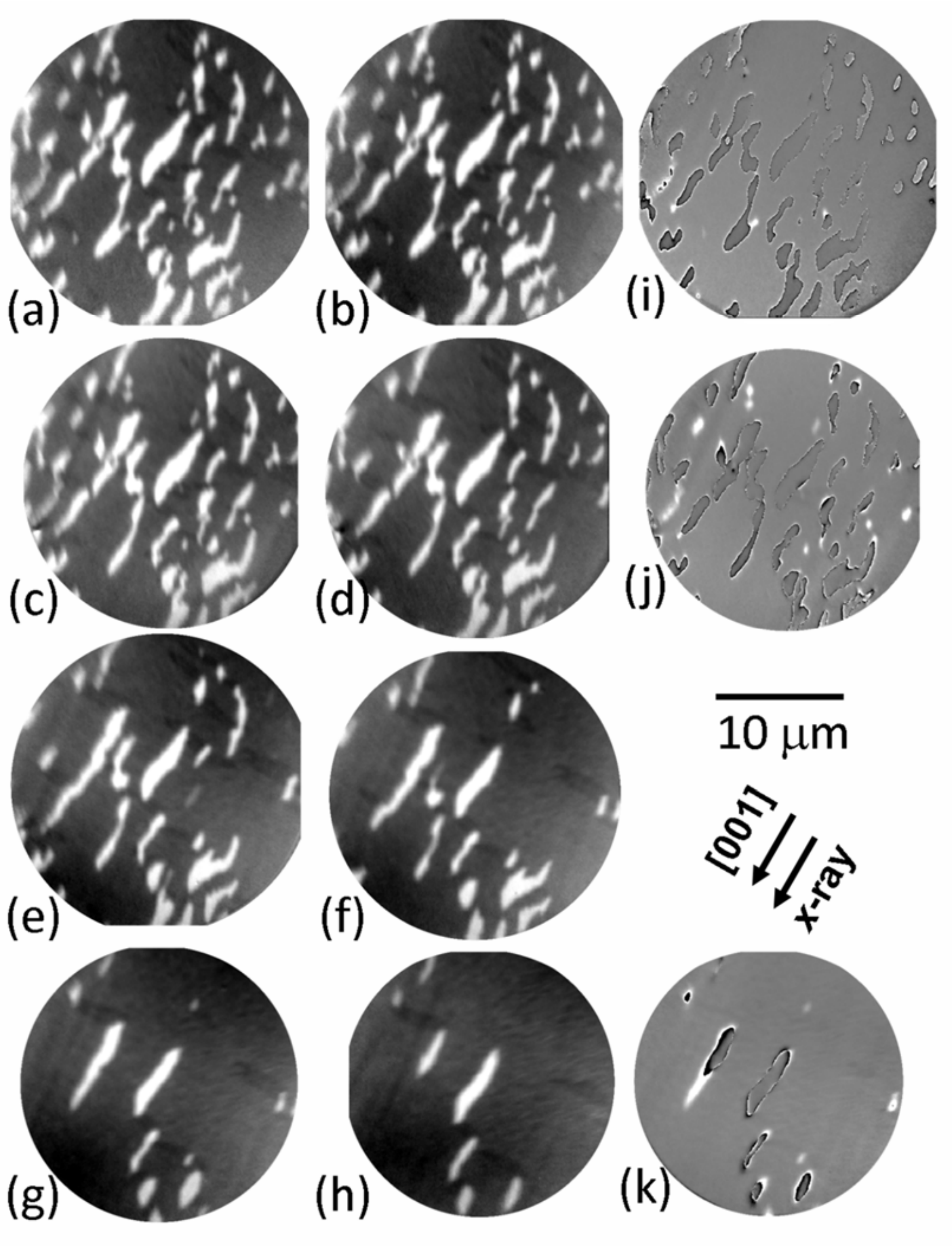

Figure 5. 9 Co L_3 XMCD images in 5 ML Co/25 ML $Fe_{54}Mn_{46}$/Cu(001) at different times during heating of the sample, (a) RT, (b) 305 K, (c) 315 K, (d) 330 K, (e) 370 K, (f) 386 K, (d) 408 K, and (e) 430 K. Images (i), (j), and (k) show the difference between the images presented in panels (a-b), (c-d), and (g-h), respectively.

5.3 Discussions and conclusion

The static Co and Ni XMCD domain images of a Co wedge/15 ML Ni/Cu(001) bilayer show the same magnetic domain structures, indicating strong exchange coupling between the two FM layers (Figure 5. 1). The spin-reorientation transition of the bilayer from out-of-plane to in-plane is obtained with increasing Co layer thickness. After heating this area by a strong laser beam as shown in Figure 5. 2, the domain structures become big in the in-plane region, while smaller stripe domains are formed in the out-of-plane area. The width of the stripe domains is narrow near to the laser irradiation position, which could mean that the narrow domains are the stable state in this bilayer thickness range. Narrow domains are also found close to the SRT, as has been found in previous results of Co/Ni/Cu(001)[128] and Fe/Ni/Cu(001).[129,130] The domain density of the perpendicular magnetization increases towards the SRT line in the Co/Ni/Cu(001) sample. In Fe/Ni/Cu(001) bilayers, it has been found that the stripe domain width decreases exponentially as the system approaches the SRT point.[130] The formation of perpendicularly magnetized domains with decreasing size upon approaching the spin reorientation transition can be explained by magnetostatic stray field energy minimization for decreasing domain wall energy.[128]

For a certain power of the laser beam on the SRT region as shown in Figure 5. 3, it is found that the domains near to the SRT changed more easily than other areas in the same temperature range, which could be either due to a lower Curie temperature or to a fast movement of domains. Here we can not distinguish between a conventional paramagnetic phase and a dynamical stripe phase. After the laser is stopped, the domains start to recover and reconstruct, but in detail are different compared to the previous ones. A similar result was reported on Fe/Ni/Cu(001) samples, where the stripe domains start to melt in some regions near to the SRT with increasing sample temperature, and these region is further expanding at higher temperatures.[129]

In order to investigate the magnetization dynamics in the canted magnetization range after the excitation by the laser, pump-probe experiments has been performed in the region of the SRT on the Co wedge/15 ML Ni/Cu(001) sample. The dynamic results are presented in Figure 5. 4. Four marked areas show the demagnetization around zero delay, two areas near to the SRT indicate a slower magnetization recovery, which could be due to the lower Curie temperature in these areas.

Another two in-plane areas more far away from the SRT show a fast magnetization recovery. Due to the small signal-to-noise ratio in these data, we cannot reveal the precession in this sample. The precession frequency of the magnetization with in-plane areas seems to be higher than in out-of-plane regions. The dynamic results from out-of-plane areas main show a steady change with delay time.

We also did the simulation to explain the experiment results. The first simulated system is 3 ML Co/15 ML Ni with identical Curie temperature of both layers (600 K). From the results in Figure 5. 5, it shows that the Ni and Co layers are coupled to each other, and that after the demagnetization the magnetization at the position of domain walls starts to precess, while the amplitude of the precession increases with increasing maximum electron temperature. The simulation data for a maximum electron temperature of 750 K (Figure 5. 4) would fit to the experimental data of area 4 in Figure 5. 5. However, since this temperature is higher than the Curie temperature of the sample, in this case the domain structures might be different after every pulse. Furthermore, the simulation data arise from an area inside a domain wall, while the experimental results mainly stem from inside the domains.

For the second simulated system, 2.5 ML Co with a T_c of 450 K and 15 ML Ni with a T_c of 540 K (Figure 5. 6), a large domain with uniform magnetization was assumed for the simulation. Here the Co data show a slower recovery after demagnetization than the Ni ones due to the lower T_c. Subsequently both the Ni and Co magnetizations start to precess with the same frequency. In the experiment only results for Co are obtained, such that it is not possible to prove this assumption.

Combining the experiment and the simulation results, we conclude a full demagnetization of the Co layer at delay zero. The regions near to SRT show a slower recovery process than the areas which are more far away from the SRT. This difference could be due to a lower Curie temperature of the regions near the SRT. Similar results have been observed for different laser fluencies, i.e., the magnetization recovery time slows down as the laser pump fluence is increased.[119,131] After the magnetization has recovered, the system seems to precess, unfortunately, we cannot confirm this from our experimental results because of the small signal-to-noise ratio. The simulation data present precession with a frequency in the GHz range.

The small magnetic domains seen in the Co, Fe and Mn XMCD images in Figure 5. 7 from a 8 ML Co/22 ML $Fe_{36}Mn_{64}$/Cu(001) sample, indicate a magnetic interaction between the two layers.

Ferromagnetic Fe and Mn are induced by the Co layer. The ferromagnetic Fe moments and the Co magnetization are ferromagnetically coupled to each other, while the ferromagnetic Mn moments with the weaker XMCD contrast is antiferromagnetic ally aligned to both Fe and Co. Offi *et al.*[132] had reported this phenomenon, i.e., a net magnetic moment is induced in Fe and Mn when the Co film is in contact with $Fe_{50}Mn_{50}$, independently of the paramagnetic or antiferromagnetic state of the $Fe_{50}Mn_{50}$ thin films. In their experimental results, the direction of the net magnetic moment of Mn is either parallel in Co/$Fe_{50}Mn_{50}$/Cu(001) or antiparallel to Co and Fe in $Fe_{50}Mn_{50}$/ Co/Cu(001). The explanation was that this is related to the sensitivity of the magnetic state of the Mn atoms to the structural and magnetic environment in which they are embedded.

From the thermal treatment experiment of 5 ML Co/25 ML $Fe_{54}Mn_{46}$ on Cu(001) in Figure 5. 9, it was found that overall the size of in-plane domains is getting larger with increasing sample temperature. The main changes of the domain pattern arise from the boundaries of the domains. The temperature dependence of stripe domains in out-of-plane Ni films on Cu(001) has been reported, it shows a thermal melting of the magnetic stripe domain pattern when approaching the Curie temperature.[133] It has been observed that the mobility of the domains follows an exponential behavior. This has been attributed to thermally activated processes.[133]

From the large domains observed for Co in 8 ML Co/28 ML $Fe_{40}Mn_{60}$/Cu(001), as shown in Figure 5. 8, by an angle-dependent measurement of the XMCD contrast the magnetization direction has been determined as <110>, and not along [001], as expected for Co coupled to an AFM $Fe_{40}Mn_{60}$ layer.

We investigated several Co/Fe_xMn_{1-x}/Cu(001) samples, however in, all of these the Co layer was magnetized along <110>. The problem of sample could be due to the bad pressure during deposition.

Summary and outlook

The static magnetic properties of FM/Mn/FM (FM: Ni, Co) trilayers epitaxially grown on a Cu(001) single crystal have been investigated in detail. The bottom FM film as well as the Mn film exhibit a layer-by-layer growth mode deduced from the oscillations in the medium energy electron diffraction intensity recorded during deposition. The AFM γ phase of expanded-fct Mn is demonstrated by low energy electron diffraction I(V) curves after deposition of Mn on Co/Cu(001). The magnetic behavior of the trilayers has been studied by magneto-optical Kerr effect (MOKE) measurements and photoelectron emission microscope (PEEM) experiments with x-ray magnetic circular dichroism (XMCD) as magnetic contrast mechanism. Laser-induced dynamic magnetic properties of Co/Ni/Cu(001) have been studied using PEEM with time-delayed pump (fs laser) – probe (X-ray) measurements. The following main results have been obtained:

For the Co/Mn/Co system: i), it was found that trilayer samples, and particularly those with filled last atomic layer of the bottom Co layer, show a higher onset thickness of Mn for AFM order (t_{AFM}) at RT compared to Mn/Co bilayer samples, for example, t_{AFM} is 3.4 (4.0) and 4.1 (4.8) ML for 10.0 (10.5) ML bottom Co film thickness in Mn/Co bilayers and Co/Mn/Co trilayers, respectively. At a Mn thickness above t_{AFM}, H_c of bilayers with filled bottom Co layer increases as a function of Mn thickness until 8-10 ML Mn thickness, after which it then stays about constant until 14 ML Mn thickness, for example, 60 mT for 11 ML Mn/10.0 ML Co. H_c of bilayer samples with half-filled bottom Co layer in contrast, shows a sharp maximum at around 5-6 ML Mn thickness and then strikingly decreases up to 14 ML Mn thickness, for example, 10 mT for 11 ML Mn/10.5 ML Co. We conclude that the FM/AFM coupling is stronger for integer atomic layer filling at the interface. All samples with Mn thicknesses above 6-7 ML showed a small exchange bias of <10 mT with a relatively larger error. ii), Above 8-10 ML Mn thickness, magnetization loops with two separate steps have been observed in trilayers with bottom Co layer thicknesses of 8.0, 9.6, 10.0, 15.0, and 20 ML. These decoupled loops start at lower Mn thickness for higher top Co layer thickness as well as for lower sample temperature. For the decoupled loops, the step with lower coercivity corresponds to the top Co layer, the one with higher coercivity to the bottom Co layer. This could be related to the interface roughness. The interface between Mn and bottom Co layer is smoother than that between the top Co and the Mn layer, such that the bottom Co layer shows a higher coercivity due to stronger FM/AFM coupling. However, magnetization loops with only one step were observed in Co/Mn/10.5 ML Co trilayers. This could be due to similar coercivities of the bottom and top Co layers, which could lead to a merging of the magnetizations reversals. iii), the coercivity and remanence of the top Co layer show an oscillation with 1 ML period as a function of the Mn layer thickness, which we attribute to roughness oscillations at the upper Co-Mn interface induced by the layer-by-layer growth of Mn on Co. The strength of the direct exchange coupling between the two Co layers, by the AFM Mn layer deduced from minor-loop measurements, exhibits an oscillation with a period of 2 ML Mn thickness in the range of 0-15 $\mu J/m^2$. Comparing three different bottom Co layer thicknesses (9.6, 10.0, 15.0), the interlayer exchange coupling energy is independent on the interface roughness and the thickness of the top Co layer. iv), a long-period RKKY-type oscillatory coupling was observed with a periodicity of ~5.6 ML of Mn thickness with antiferromagnetic maxima at 2.5, 8.2, 13.7, 19.2 ML Mn thickness. The first AFM coupling maximam at unexpectedly low Mn thickness could be also linked to an FM-AFM phase coexistence in the Mn layer. The RKKY coupling energy at the second maximum is -33.8 $\mu J/m^2$ for both 15 ML and 10 ML Co top layer on Mn/10.0 ML bottom Co layer. From estimating the relative weight of RKKY and direct exchange coupling contributions to the antiferromagnetic coupling at the third and fourth antiferromagnetic maximum, it seems that both contribute about equally.

For the Ni/Mn/Co system: i), The Ni layer shows layer-by-layer growth on the Mn/Co film, the p(1×1) LEED pattern of 15 ML Ni/15.1 ML Mn/10.0 ML Co presents a lower contrast than that of Cu(001), indicating a rougher surface roughness. From the PEEM data of 15 ML Ni/Mn/Co/Cu(001), big domains with in-plane magnetization were found in the Co layer for all the samples. Stripe domains with out-of-plane magnetization were observed in the Ni layer for thicker spacer layer (15 ML Ni/25 ML Mn/Co). With decreasing spacer layer thickness (4-5 ML), the domain size in the Ni layer is getting bigger, similar as the Co domains. Some regions with antiparallel coupling between Ni and Co layers are found. In the 15 ML Ni/15 ML Co bilayer, identical domains with four different grayscale contrasts were observed in both the Ni and Co layers due to the strong direct coupling. ii), the longitudinal MOKE results showed that t_{AFM} is increased by the deposition of 15 ML Ni on Mn/10.0 ML Co from 4.0 ML to 4.6 ML Mn thickness. Above

t_{AFM}, the H_c is higher in the trilayer than in the bilayer, which is similar to the case of 5 ML Co on Mn/10.0 ML Co. Considering the coercivity, it seems that the top 15 ML Ni layer acts like another 5 ML Co layer on the bilayer. t_{AFM} of the trilayer in polar MOKE shows a nearly the same value (4.7 ML). Combing the t_{AFM} results of Co/Mn/Co/Cu(001) and Ni/Mn/Co/Cu(001), the top Co or Ni FM layer will upshift the valued t_{AFM}, for example, from 4.1 to 4.7 ML Mn thickness in 10 ML Co/Mn/ 10.0 ML Co and 15 ML Ni/Mn/10.0 ML Co samples. This shifted t_{AFM} is independent of whether there is an in-plane or out-of-plane magnetization configuration.

For the (Co/)Ni/Mn/15 ML Ni system: i), the top Ni layer shows two MEED oscillations during deposition on a Mn/15 ML Ni bilayer. This indicates that the top Ni/Mn interface is smoother than the Mn/bottom Ni one. ii), for polar MOKE, the Mn/15 ML Ni and 20 ML Ni/Mn/15 ML Ni samples show the same t_{AFM} of 3.2 ML, while t_{AFM} for 5 ML Co/20 ML Ni/Mn/15 ML Ni is increased to 3.8 ML. Combining the data from Co/Mn/Co and Ni/Mn/Co, a), if the bottom FM layer has in-plane magnetization, the presence of the top FM layer increases t_{AFM}. b), if the bottom FM layer has out-of-plane magnetization, t_{AFM} of trilayer and bilayer are the same only if the top layer has also out-of-plane magnetization. This could be related to a 2D spin configuration in Mn with in-plane direction. The coupling between the Mn spin structure and the adjacent FM layer could then be different for different magnetization directions of the FM layers, i.e., the Mn/FM interface spin structure is influenced by the spin direction of the FM layer. The coupling or interaction across the interface is stronger with an adjacent FM layer with in-plane magnetization. iii), above 8 ML Mn thickness, two steps are observed in the magnetization loops, where the step with the lower coercivity corresponds to the bottom Co layer, and the one with higher coercivity to the top Co layer. As discussed before, the interface roughness between Mn and the bottom Ni layer is higher than that of the top Ni/Mn interface. Here the rougher interface roughness shows the lower coercivity, which indicates a weaker coupling at the rougher interface. This result is consistent to Co/Mn/Co trilayer data as well as the Mn/filled Co and Mn/half-filled Co layer bilayer result. iv), after deposition of 5 ML Co on 20 ML Ni/Mn/15 ML Ni, the coercivity of polar MOKE measurement is higher than that of Mn/15 ML Ni as well as that of the bottom layer of 15 ML Ni/Mn/15 ML Ni. This higher H_c could be attributed to canted spins in Mn or in the bottom Ni layer induced by the coupling to the in-plane Co layer. For the longitudinal MOKE results, the behavior of H_c is similar to Co/Mn/Co trilayers with half-integer number of atomic layers in the bottom Co layer. v), in our Ni/Mn/15 ML Ni trilayers, neither the direct coupling nor the RKKY-type coupling were found in these samples.

Combining the MOKE results of the FM/Mn/FM samples, 1) FM layers with smoother interfaces with Mn show a higher coercivity than FM layers with rougher interfaces. 2) The coupling between the Mn and adjacent FM film is dependent on the in-plane or the out-of-plane magnetization in the FM layer. The higher t_{AFM} is found in Mn/Co than the Mn/Ni bilayer, this could be due to the in-plane spins in Co layer is more efficient to reduce the effective Mn thickness by alloying or proximity effects at the interface. This interface effect is more obviously in the smoother surface between Mn and Co layers, i.e., the onset of antiferromagnetic order of Mn starts later in filled topmost atomic layer of bottom Co film.

0-5 ML Co/15 ML Ni bilayers on Cu(001) have been investigated in detail. The spin-reorientation transition (SRT) between out-of-plane and in-plane magnetization was imaged by PEEM. The domain structures near to the SRT were more easily changed by the laser irradiation than in other regions. These change were irreversible. The response of the magnetization in the Co layer to the laser pulse excitation shows a slower recovery close to the SRT after demagnetization, probably due to a lower Curie temperature.

The FM/wedged Mn/FM can be future studied by PEEM in detail, from the XMCD contrast we can estimate the coupling angle between the two FM layers. The surface roughness of the Mn/FM could be investigated by scanning tunneling microscope. Combining with the MOKE data, we can get a full understanding of the coupling of these system. For the magnetic dynamic studying, Ni/Co system for example, both the Ni and Co signals should be recorded in the PEEM experiment. The system with simple domain structures should be an alternative choice to study laser-induced dynamic, which will increase the signal-to-noise ratio. This precession results should be compared to other data from high-frequency measurements, like ferromagnetic resonance, time-resolved MOKE.

Bibliography

[1] J. Stöhr and H. C. Siegmann, *Magnetism: from fundamentals to nanoscale dynamics*, Vol. 152 (Springer, 2007).

[2] F. Jorgensen, *The Complete Handbook of Magnetic Recording* (TAB Books, Mc-Graw Hill, New York, 1995).

[3] S. X. Wang and A. M. Taratorin, *Magnetic Information Storage Technology: A Volume in the Electromagnetism Series*, (Academic New York, 1999).

[4] http://en.wikipedia.org/wiki/Magnetic_recording (05.08.2014)

[5] M. N. Baibich, J. M. Broto, A. Fert, F. N. Vandau, F. Petroff, P. Eitenne, G. Creuzet, A. Friederich, and J. Chazelas, *Giant magnetoresistance of (001)Fe/(001) Cr magnetic superlattices*, Phys. Rev. Lett. **61**, 2472 (1988).

[6] G. Binasch, P. Grunberg, F. Saurenbach, and W. Zinn, *Enhanced magnetoresistance in layered magnetic-structures with antiferromagnetic interlayer exchange*, Phys. Rev. B **39**, 4828 (1989).

[7] W. H. Meiklejohn and C. P. Bean, *New magnetic anisotropy*, Phys. Rev. **102**, 1413 (1956).

[8] W. H. Meiklejohn, *Exchange anisotropy - a review*, J. Appl. Phys. **33**, 1328 (1962).

[9] W. H. Meiklejohn and C. P. Bean, *New magnetic anisotropy*, Phys. Rev. **105**, 904 (1957).

[10] J. Nogués and I. K. Schuller, *Exchange bias*, J. Magn. Magn. Mater. **192**, 203 (1999).

[11] Z. Shi, J. Du, and S. M. Zhou, *Exchange bias in ferromagnet/antiferromagnet bilayers*, Chin. Phys. B **23**, 13 (2014).

[12] F. B. Hagedorn, *Exchange anisotropy in oxidized permalloy thin films at low temperatures*, J. Appl. Phys. **38**, 3641 (1967).

[13] M. Takahashi, A. Yanai, S. Taguchi, and T. Suzuki, *A study of exchange-anisotropy in Co-CoO evaporated thin-films*, Jpn. J. Appl. Phys. **19**, 1093 (1980).

[14] J. Nogues, D. Lederman, T. J. Moran, I. K. Schuller, and K. V. Rao, *Large exchange bias and its connection to interface structure in FeF_2-Fe bilayers*, Appl. Phys. Lett. **68**, 3186 (1996).

[15] Y. J. Chen, D. K. Lottis, E. D. Dahlberg, J. N. Kuznia, A. M. Wowchak, and P. I. Cohen, *Exchange effects in molecular-beam-epitaxy grown iron films*, J. Appl. Phys. **69**, 4523 (1991).

[16] Y. Hamakawa, H. Hoshiya, T. Kawabe, Y. Suzuki, R. Arai, K. Nakamoto, M. Fuyama, and Y. Sugita, *Spin-valve heads utilizing antiferromagnetic NiO layers*, IEEE Trans. Magn. **32**, 149 (1996).

[17] S.S.P Parkin, V.S Speriosu, L.M Falicov, and F. Mejía-Lira, J.L Morán-López (Eds.), Magnetic Properties of Low-Dimensional Systems II, (Springer, Berlin 1990), p. 110.

[18] D. Mauri, E. Kay, D. Scholl, and J. K. Howard, *Novel method for determining the anisotropy constant of MnFe in a NiFe/MnFe sandwich*, J. Appl. Phys. **62**, 2929 (1987).

[19] S. M. Zhou, K. Liu, and C. L. Chien, *Dependence of exchange coupling in permalloy/$Cr_{82}Al_{18}$ bilayers on the constituent layer thickness*, J. Appl. Phys. **87**, 6659 (2000).

[20] J. T. Kohlhepp and W. J. M. de Jonge, *Stabilization of metastable expanded face-centered-tetragonal manganese*, Phys. Rev. Lett. **96**, 237201 (2006).

[21] R. Jungblut, R. Coehoorn, M. T. Johnson, C. Sauer, P. J. Vanderzaag, A. R. Ball, T. Rijks, J. Destegge, and A. Reinders, *Exchange biasing in MBE-grown $Ni_{80}Fe_{20}/Fe_{50}Mn_{50}$ bilayers*, J. Magn. Magn. Mater. **148**, 300 (1995).

[22] O. Allegranza and M. M. Chen, *Effect of substrate and antiferromagnetic films thickness on exchange-bias field (invited)*, J. Appl. Phys. **73**, 6218 (1993).

[23] Y. Ijiri, J. A. Borchers, R. W. Erwin, S. H. Lee, P. J. van der Zaag, and R. M. Wolf, *Perpendicular coupling in exchange-biased Fe_3O_4/CoO superlattices*, Phys. Rev. Lett. **80**, 608 (1998).

[24] S. S. Lee, D. G. Hwang, C. M. Park, K. A. Lee, and J. R. Rhee, *Effects of crystal texture on exchange anisotropy in NiO spin valves*, J. Appl. Phys. **81**, 5298 (1997).

[25] C. M. Park, K. I. Min, and K. H. Shin, *Effects of surface topology and texture on exchange anisotropy in NiFe/Cu/NiFe/FeMn spin valves*, J. Appl. Phys. **79**, 6228 (1996).

[26] S. L. Burkett, S. Kora, J. C. Lusth, and M. R. Parker, *Annealing of spin valves with high exchange pinning fields*, IEEE Trans. Magn. **33**, 3544 (1997).

[27] A. P. Malozemoff, *Random-field model of exchange-anisotropy at rough ferromagnetic-antiferromagnetic interfaces*, Phys. Rev. B **35**, 3679 (1987).

[28] N. C. Koon, *Calculations of exchange bias in thin films with ferromagnetic/antiferromagnetic interfaces*, Phys. Rev. Lett. **78**, 4865 (1997).

[29] W. F. Egelhoff, P. J. Chen, C. J. Powell, M. D. Stiles, and R. D. McMichael, *Growth of giant magnetoresistance spin valves using indium as a surfactant*, J. Appl. Phys. **79**, 2491 (1996).

[30] D. H. Han, J. G. Zhu, and J. H. Judy, *NiFe/NiO bilayers with high exchange coupling and low coercive fields*, J. Appl. Phys. **81**, 4996 (1997).

[31] C. Binek, A. Hochstrat, and W. Kleemann, *Exchange bias in a generalized Meiklejohn-Bean approach*, J. Magn. Magn. Mater. **234**, 353 (2001).

[32] D. Mauri, H. C. Siegmann, P. S. Bagus, and E. Kay, *Simple-model for thin ferromagnetic-films exchange coupled to an antiferromagnetic substrate*, J. Appl. Phys. **62**, 3047 (1987).

[33] L. Néel, Ann. Phys. (France) **1**, 61 (1967).

[34] A. P. Malozemoff, *Heisenberg-to-Ising crossover in a random-field model with uniaxial anisotropy*, Phys. Rev. B **37**, 7673 (1988).

[35] Z. Q. Qiu, J. Pearson, and S. D. Bader, *Oscillatory interlayer magnetic coupling of wedged*

Co/Cu/Co sandwiches grown on Cu(100) by molecular-beam epitaxy, Phys. Rev. B **46**, 8659 (1992).

[36] R. Coehoorn, *Period of oscillatory exchange interactions in Co/Cu and Fe/Cu multilayer systems*, Phys. Rev. B **44**, 9331 (1991).

[37] M. Matczak, B. Szymanski, M. Urbaniak, M. Nowicki, H. Glowinski, P. Kuswik, M. Schmidt, J. Aleksiejew, J. Dubowik, and F. Stobiecki, *Antiferromagnetic magnetostatic coupling in Co/Au/Co films with perpendicular anisotropy*, J. Appl. Phys. **114** (2013).

[38] W. Kuch, L. I. Chelaru, F. Offi, J. Wang, M. Kotsugi, and J. Kirschner, *Tuning the magnetic coupling across ultrathin antiferromagnetic films by controlling atomic-scale roughness*, Nat. Mater. **5**, 128 (2006).

[39] T. Kai, *Interlayer exchange coupling and electronic structure of Co/Mn multilayers*, J. Magn. Magn. Mater. **214**, 167 (2000).

[40] S. T. Purcell, M. T. Johnson, N. W. E. McGee, R. Coehoorn, and W. Hoving, *2-monolayer oscillations in the antiferromagnetic exchange coupling through Mn in Fe/Mn/Fe sandwich structures*, Phys. Rev. B **45**, 13064 (1992).

[41] J. Unguris, R. J. Celotta, and D. T. Pierce, *Observation of 2 different oscillation periods in the exchange coupling of Fe/Cr/Fe(100)*, Phys. Rev. Lett. **67**, 140 (1991).

[42] Y. Wang, P. M. Levy, and J. L. Fry, *Interlayer magnetic coupling in Fe/Cr multilayered structures*, Phys. Rev. Lett. **65**, 2732 (1990).

[43] S. S. P. Parkin, N. More, and K. P. Roche, *Oscillations in exchange coupling and magnetoresistance in metallic superlattice structures: Co/Ru, Co/Cr, and Fe/Cr*, Phys. Rev. Lett. **64**, 2304 (1990).

[44] J. Moritz, P. Bacher, S. Auffret, and B. Dieny, *Interlayer coupling between out-of-plane magnetized multilayers across a thin antiferromagnetic spacer*, J. Magn. Magn. Mater. **323**, 2391 (2011).

[45] Z. Y. Liu and S. Adenwalla, *Oscillatory interlayer exchange coupling and its temperature dependence in $[Pt/Co]_3/NiO/[Co/Pt]_3$ multilayers with perpendicular anisotropy*, Phys. Rev. Lett. **91**, 037207 (2003).

[46] L. E. Nistor, B. Rodmacq, S. Auffret, A. Schuhl, M. Chshiev, and B. Dieny, *Oscillatory interlayer exchange coupling in MgO tunnel junctions with perpendicular magnetic anisotropy*, Phys. Rev. B **81**, 4 (2010).

[47] L. Néel, *Magnetisme - sur un nouveau mode de couplage entre les animantations de deux couches minces ferromagnetiques*, C. R. Hebd. Acad. Sci. **255**, 1676 (1962).

[48] L. Thomas, M. G. Samant, and S. S. P. Parkin, *Domain-wall induced coupling between ferromagnetic layers*, Phys. Rev. Lett. **84**, 1816 (2000).

[49] V. Baltz, B. Rodmacq, A. Bollero, J. Ferre, S. Landis, and B. Dieny, *Balancing interlayer dipolar interactions in multilevel patterned media with out-of-plane magnetic anisotropy*,

Appl. Phys. Lett. **94**, 3 (2009).

[50] M. A. Ruderman and C. Kittel, *Indirect exchange coupling of nuclear magnetic moments by conduction electrons*, Phys. Rev. **96**, 99 (1954).

[51] T. Kasuya, *A Theory of Metallic Ferro- and Antiferromagnetism on Zener's Model*, Prog. Theor. Phys. **16**, 45 (1956).

[52] K. Yosida, *Magnetic properties of Cu-Mn alloys*, Phys. Rev. **106**, 893 (1957).

[53] P. Grünberg, R. Schreiber, Y. Pang, M. B. Brodsky, and H. Sowers, *Layered magnetic-structures: evidence for antiferromagnetic coupling of Fe layers across Cr interlayers*, Phys. Rev. Lett. **57**, 2442 (1986).

[54] C. Carbone and S. F. Alvarado, *Antiparallel coupling between Fe layers separated by a Cr interlayer: dependence of the magnetization on the film thickness*, Phys. Rev. B **36**, 2433 (1987).

[55] S. T. Purcell, W. Folkerts, M. T. Johnson, N. W. E. McGee, K. Jager, J. A. Destegge, W. B. Zeper, and W. Hoving, *Oscillations with a period of 2 Cr monolayers in the antiferromagnetic exchange coupling in a (001) Fe/Cr/Fe sandwich structure*, Phys. Rev. Lett. **67**, 903 (1991).

[56] M. Y. Zhuravlev, E. Y. Tsymbal, and S. S. Jaswal, *Exchange model for oscillatory interlayer coupling and induced unidirectional anisotropy in [Pt/Co]$_3$/NiO/[Co/Pt]$_3$ multilayers*, Phys. Rev. Lett. **92**, 219703 (2004).

[57] X. H. Liu, W. Liu, F. Yang, X. K. Lv, W. B. Cui, S. Guo, W. J. Gong, and Z. D. Zhang, *Temperature dependence of competition between interlayer and interfacial exchange couplings in ferromagnetic/antiferromagnetic/ferromagnetic trilayers*, Appl. Phys. Lett. **95**, 222505 (2009).

[58] M. Rührig, R. Schafer, A. Hubert, R. Mosler, J. A. Wolf, S. Demokritov, and P. Grünberg, *Domain observations on Fe-Cr-Fe layered structures - evidence for a biquadratic coupling effect*, Phys. Status Solidi A-Appl. Mat. **125**, 635 (1991).

[59] J. T. Kohlhepp, O. Kurnosikov, and W. J. M. de Jonge, *Oscillatory biquadratic antiferromagnet/ferromagnet interface exchange coupling*, J. Magn. Magn. Mater. **286**, 220 (2005).

[60] J. T. Kohlhepp and W. J. M. de Jonge, *Influence of the FM/AFM interface morphology on the exchange coupling in epitaxial Co(001)/fct-Mn(001)*, J. Appl. Phys. **95**, 6840 (2004).

[61] D. A. Young, *Phase Diagrams of the Elements* (Academic, Berkeley, 1991).

[62] S.-S. Yan, R. Schreiber, F. Voges, C. Osthöver, and P. Grünberg, *Oscillatory interlayer coupling in Fe/Mn/Fe trilayers*, Phys. Rev. B **59**, R11641 (1999).

[63] Y. Henry, V. Pierron-Bohnes, P. Vennégues, and K. Ounadjela, *Lattice-relaxation and 3-dimensional reflection high-energy electron-diffraction analysis of strained epitaxial Co/Mn superlattices*, J. Appl. Phys. **76**, 2817 (1994).

[64] Q. Wang, N. Metoki, C. Morawe, T. Zeidler, and H. Zabel, *Structural and magnetic-properties*

of Co face-centered-cubic Mn(001) multilayers, J. Appl. Phys. **78**, 1689 (1995).

[65] Y. Z. Wu, G. S. Dong, and X. F. Jin, *Negative magnetic remanence in Co/Mn/Co grown on GaAs(001)*, Phys. Rev. B **64**, 214406 (2001).

[66] E. Beaurepaire, J. C. Merle, A. Daunois, and J. Y. Bigot, *Ultrafast spin dynamics in ferromagnetic nickel*, Phys. Rev. Lett. **76**, 4250 (1996).

[67] J. Hohlfeld, E. Matthias, R. Knorren, and K. H. Bennemann, *Nonequilibrium magnetization dynamics of nickel*, Phys. Rev. Lett. **78**, 4861 (1997).

[68] A. Scholl, L. Baumgarten, R. Jacquemin, and W. Eberhardt, *Ultrafast spin dynamics of ferromagnetic thin films observed by fs spin-resolved two-photon photoemission*, Phys. Rev. Lett. **79**, 5146 (1997).

[69] J. Gudde, U. Conrad, V. Jahnke, J. Hohlfeld, and E. Matthias, *Magnetization dynamics of Ni and Co films on Cu(001) and of bulk nickel surfaces*, Phys. Rev. B **59**, R6608 (1999).

[70] B. Koopmans, M. van Kampen, J. T. Kohlhepp, and W. J. M. de Jonge, *Ultrafast magneto-optics in nickel: Magnetism or optics?*, Phys. Rev. Lett. **85**, 844 (2000).

[71] M. Van Kampen, C. Jozsa, J. T. Kohlhepp, P. LeClair, L. Lagae, W. J. De Jonge, and B. Koopmans, *All-optical probe of coherent spin waves*, Phys. Rev. Lett. **88**, 227201 (2002).

[72] G. P. Ju, J. Hohlfeld, B. Bergman, R. J. M. van de Veerdonk, O. N. Mryasov, J. Y. Kim, X. W. Wu, D. Weller, and B. Koopmans, *Ultrafast generation of ferromagnetic order via a laser-induced phase transformation in FeRh thin films*, Phys. Rev. Lett. **93**, 4 (2004).

[73] J. U. Thiele, M. Buess, and C. H. Back, *Spin dynamics of the antiferromagnetic-to-ferromagnetic phase transition in FeRh on a sub-picosecond time scale*, Appl. Phys. Lett. **85**, 2857 (2004).

[74] T. Roth, D. Steil, D. Hoffmann, M. Bauer, M. Cinchetti, and M. Aeschlimann, *Dynamics of the coercivity in ultrafast pump-probe experiments*, J. Phys. D: Appl. Phys. **41**, 5 (2008).

[75] M. C. Weber, H. Nembach, and J. Fassbender, *Picosecond optical control of the magnetization in exchange biased NiFe/FeMn bilayers*, J. Appl. Phys. **95**, 6613 (2004).

[76] Z. Xu, X. D. Liu, R. X. Gao, Z. F. Chen, T. S. Lai, H. N. Hu, S. M. Zhou, X. J. Bai, and J. Du, *Photoinduced magnetic softening of perpendicularly magnetized* $L1_0$*-FePt granular films*, Appl. Phys. Lett. **93**, 3 (2008).

[77] N. Kazantseva, U. Nowak, R. W. Chantrell, J. Hohlfeld, and A. Rebei, *Slow recovery of the magnetisation after a sub-picosecond heat pulse*, EPL **81**, 6 (2008).

[78] U. Atxitia, O. Chubykalo-Fesenko, N. Kazantseva, D. Hinzke, U. Nowak, and R. W. Chantrell, *Micromagnetic modeling of laser-induced magnetization dynamics using the Landau-Lifshitz-Bloch equation*, Appl. Phys. Lett. **91** (2007).

[79] B. Koopmans, G. Malinowski, F. D. Longa, D. Steiauf, M. Faehnle, T. Roth, M. Cinchetti, and M. Aeschlimann, *Explaining the paradoxical diversity of ultrafast laser-induced demagnetization*, Nat. Mater. **9**, 259 (2010).

[80] T. L. Gilbert, *A Lagrangian formulation of the gyromagnetic equation of the magnetic field*, Phys. Rev. **100**, 1243 (1955).

[81] A. Kirilyuk, A. V. Kimel, and T. Rasing, *Ultrafast optical manipulation of magnetic order*, Rev. Mod. Phys. **82**, 2731 (2010).

[82] *D. Briggs and M. P. Seah (Eds.), Practical Surface Analysis* (Wiley, Chichester, 1990).

[83] J. B. Pendry, Low Energy Electron Diffraction, (Academic Press, New York, 1974).

[84] J. Stöhr, *X-ray magnetic circular dichroism spectroscopy of transition metal thin films*, J. Electron Spectrosc. Relat. Phenom. **75**, 253 (1995).

[85] J. Kerr, Philos. Mag. **3**, 339 (1877).

[86] J. Kerr, Philos. Mag. **5**, 161 (1878).

[87] *See Molecular Electro-Optics, Part 1, Theory and Methods, edited by C. T. O'Konski* (Dekker, New York, 1976).

[88] E. R. Moog and S. D. Bader, *Smoke signals from ferromagnetic monolayers: p(1x1) Fe/Au(100)*, Superlattices Microstruct. **1**, 543 (1985).

[89] S. D. Bader, E. R. Moog, and P. Grünberg, *Magnetic hysteresis of epitaxially-deposited iron in the monolayer range: a Kerr effect experiment in surface magnetism*, J. Magn. Magn. Mater. **53**, L295 (1986).

[90] J. Zak, E. Moog, C. Liu, and S. Bader, *Universal approach to magneto-optics*, J. Magn. Magn. Mater. **89**, 107 (1990).

[91] L. D. Landau and E. M. Lifshtz, Electrodynamics of Continuous Media, (Pergamon, London, 1960).

[92] J. C. Maxwell, Electricity and Magnetism **Vol. 2.**, Chap. 21 (1873).

[93] H. R. Hulme, Proc. R. Soc. London, Ser. A **135**, 237 (1932).

[94] C. Kittel, Phys. Rev. **83**, 208(A) (1951).

[95] P. N. Argyres, *Theory of the Faraday and Kerr effects in ferromagnetics*, Phys. Rev. **97**, 334 (1955).

[96] http://www.hindsinstruments.com/ (05.08.2014)

[97] J. T. Kohlhepp, *Exchange interaction studies using epitaxially stabilized expanded fct-Mn(001)*, J. Phys. D **40**, 1300 (2007).

[98] J. T. Kohlhepp, H. Wieldraaijer, and W. J. M. de Jonge, *Onset of magnetic interface exchange interactions in epitaxially grown Mn/Co(001)*, J. Mater. Res. **22**, 569 (2007).

[99] J. Hafner and D. Spišák, *Ab initio investigation of the magnetism of tetragonal Mn: Bulk, surface, ultrathin films, and multilayers*, Phys. Rev. B **72**, 144420 (2005).

[100] P. J. Hsu, C. I. Lu, Y. H. Chu, B. Y. Wang, C. B. Wu, L. J. Chen, S. S. Wong, and M. T. Lin,

Layered antiferromagnetic spin structures of expanded face-centered-tetragonal Mn(001) as an origin of exchange bias coupling to the magnetic Co layer, Phys. Rev. B **85**, 174434 (2012).

[101] C. H. Wang, Y. Y. Huang, and W. C. Lin, *Combination of exchange-bias and long-range interlayer couplings in Fe/fct-Mn/Co trilayers*, J. Appl. Phys. **109**, 103908 (2011).

[102] M. Caminale, R. Moroni, P. Torelli, W. C. Lin, M. Canepa, L. Mattera, and F. Bisio, *Reentrant Surface Anisotropy in the Antiferromagnetic/Ferromagnetic Bilayer Mn/Co/Cu(001)*, Phys. Rev. Lett. **112**, 037201 (2014).

[103] W. L. O'Brien and B. P. Tonner, *Surface-enhanced magnetic-moment and ferromagnetic ordering of Mn ultrathin films on fcc Co(001)*, Phys. Rev. B **50**, 2963 (1994).

[104] G. R. Harp, M. M. Schwickert, M. A. Tomaz, T. Lin, D. Lederman, E. Mayo, and W. L. O'Brien, *Competition between direct exchange and indirect RKKY coupling in Fe/V(001) superlattices*, IEEE Trans. Magn. **34**, 864 (1998).

[105] K. Lenz, S. Zander, and W. Kuch, *Magnetic proximity effects in antiferromagnet/ferromagnet bilayers: The impact on the Néel temperature*, Phys. Rev. Lett. **98**, 237201 (2007).

[106] M. Erkovan, Y. A. Shokr, D. Schiestl, C. B. Wu, and W. Kuch, *Influence of Ni_xMn_{1-x} thickness and composition on the Curie temperature of Ni in Ni_xMn_{1-x}/Ni bilayers on $Cu_3Au(001)$*, accepted for publication in J. Magn. Magn. Mater. (DOI: 10.1016/j.jmmm.2014.02.017).

[107] M. Y. Khan, C. B. Wu, and W. Kuch, *Pinned magnetic moments in exchange bias: Role of the antiferromagnetic bulk spin structure*, Phys. Rev. B **89**, 5 (2014).

[108] Y. Li and K. Baberschke, *Dimensional crossover in ultrathin Ni(111) films on W(110)*, Phys. Rev. Lett. **68**, 1208 (1992).

[109] T. Ambrose and C. L. Chien, *Finite-size effects and uncompensated magnetization in thin antiferromagnetic CoO layers*, Phys. Rev. Lett. **76**, 1743 (1996).

[110] M. Stampe, P. Stoll, T. Homberg, K. Lenz, and W. Kuch, *Influence of ferromagnetic-antiferromagnetic coupling on the antiferromagnetic ordering temperature in Ni/Fe_xMn_{1-x} bilayers*, Phys. Rev. B **81**, 104420 (2010).

[111] F. Huang, M. T. Kief, G. J. Mankey, and R. F. Willis, *Magnetism in the few-monolayers limit: a surface magnetooptic Kerr-effect study of the magnetic-behavior of ultrathin films of Co, Ni, and Co-Ni alloys on Cu(100) and Cu(111)*, Phys. Rev. B **49**, 3962 (1994).

[112] P. Krams, F. Lauks, R. L. Stamps, B. Hillebrands, and G. Guntherodt, *Magnetic anisotropies of ultrathin Co(001) films on Cu(001)*, Phys. Rev. Lett. **69**, 3674 (1992).

[113] C. M. Schneider, P. Bressler, P. Schuster, J. Kirschner, J. J. Demiguel, R. Miranda, and S. Ferrer, *Epitaxy and magnetic properties of fcc cobalt films on Cu(100)*, Vacuum **41**, 503 (1990).

[114] W. Kuch, *Layer-resolved microscopy of magnetic domains in multi-layered systems*, Appl. Phys. A-Mater. Sci. Process. **76**, 665 (2003).

[115] W. Kuch, *X-ray magnetic circular dichroism for quantitative element-resolved magnetic microscopy*, Phys. Scr. **T109**, 89 (2004).

[116] W. Kuch, L. I. Chelaru, F. Offi, J. Wang, M. Kotsugi, and J. Kirschner, *Three-dimensional noncollinear antiferromagnetic order in single-crystalline FeMn ultrathin films*, Phys. Rev. Lett. **92**, 017201 (2004).

[117] W. Kuch, X. Y. Gao, and J. Kirschner, *Competition between in-plane and out-of-plane magnetization in exchange-coupled magnetic films*, Phys. Rev. B **65** (2002).

[118] S. Mizukami, X. M. Zhang, T. Kubota, H. Naganuma, M. Oogane, Y. Ando, and T. Miyazaki, *Gilbert Damping in Ni/Co Multilayer Films Exhibiting Large Perpendicular Anisotropy*, Appl. Phys. Express **4** (2011).

[119] U. Atxitia, O. Chubykalo-Fesenko, J. Walowski, A. Mann, and M. Münzenberg, *Evidence for thermal mechanisms in laser-induced femtosecond spin dynamics*, Phys. Rev. B **81**, 174401 (2010).

[120] T. Kato, Y. Matsumoto, S. Okamoto, N. Kikuchi, O. Kitakami, N. Nishizawa, S. Tsunashima, and S. Iwata, *Time-Resolved Magnetization Dynamics and Damping Constant of Sputtered Co/Ni Multilayers*, IEEE Trans. Magn. **47**, 3036 (2011).

[121] M. K. Donahue and D. G. Porter, OOMMF User's Guide version 1.2a3 Published: 2002 URL: http://math.nist.gov/oommf.

[122] W. W. Wang, C. P. Mu, B. Zhang, Q. F. Liu, J. B. Wang, and D. S. Xue, *Two-dimensional periodic boundary conditions for demagnetization interactions in micromagnetics*, Comput. Mater. Sci. **49**, 84 (2010).

[123] M. I. Kaganov, I. M. Lifshitz, and L. V. Tanatarov, *Relaxation between electrons and the crystalline lattice*, Sov. Phys. Jetp. **4**, 173 (1957).

[124]G. P. Zhang, W. Hübner, E. Beaurepaire, and J. Y. Bigot, in *Spin Dynamics in Confined Magnetic Structures I*; *Vol. 83*, edited by B. Hillebrands and K. Ounadjela (Springer-Verlag Berlin, Berlin, 2002), p. 245.

[125] W. Weber, R. Allenspach, and A. Bischof, *Determining magnetic anisotropies from hysteresis loops*, Appl. Phys. Lett. **70**, 520 (1997).

[126] K. Baberschke, *The magnetism of nickel monolayers*, Appl. Phys. A-Mater. Sci. Process. **62**, 417 (1996).

[127] B. Schulz and K. Baberschke, *Crossover from in-plane to perpendicular magnetization in ultrathin Ni/Cu(001) films*, Phys. Rev. B **50**, 13467 (1994).

[128] W. Kuch, J. Gilles, S. S. Kang, S. Imada, S. Suga, and J. Kirschner, *Magnetic-circular-dichroism microspectroscopy at the spin reorientation transition in Ni(001) films*, Phys. Rev. B **62**, 3824 (2000).

[129] C. Won, Y. Z. Wu, J. Choi, W. Kim, A. Scholl, A. Doran, T. Owens, J. Wu, X. F. Jin, H. W. Zhao, and Z. Q. Qiu, *Magnetic stripe melting at the spin reorientation transition in Fe/Ni/Cu(001)*, Phys. Rev. B **71**, 224429 (2005).

[130] Y. Z. Wu, C. Won, A. Scholl, A. Doran, H. W. Zhao, X. F. Jin, and Z. Q. Qiu, *Magnetic Stripe*

Domains in Coupled Magnetic Sandwiches, Phys. Rev. Lett. **93**, 117205 (2004).

[131] M. Djordjevic and M. Münzenberg, *Connecting the timescales in picosecond remagnetization experiments*, Phys. Rev. B **75**, 4 (2007).

[132] F. Offi, W. Kuch, L. I. Chelaru, K. Fukumoto, M. Kotsugi, and J. Kirschner, *Induced Fe and Mn magnetic moments in Co-FeMn bilayers on Cu(001)*, Phys. Rev. B **67**, 094419 (2003).

[133] W. Kuch, K. Fukumoto, J. Wang, F. Nolting, C. Quitmann, and T. Ramsvik, *Thermal melting of magnetic stripe domains*, Phys. Rev. B **83**, 172406 (2011).

List of publications

Publication containing parts of this thesis:

B. Zhang, C.-B. Wu, and W. Kuch, *Tailoring interlayer coupling and coercivity in Co/Mn/Co trilayers by controlling the interface roughness*, J. Appl. Phys. **115**, 233915 (2014).

Other publications:

C. P. Mu, W. W. Wang, H. Y. Xia, B. Zhang, Q. F. Liu, and J. B. Wang, *Fast Magnetization Switching by Linear Vertical Microwave-Assisted Spin-Transfer Torque*, J. Nanosci. Nanotechnol. **12**, 7460 (2012).

J. B. Wang, C. P. Mu, W. W. Wang, B. Zhang, H. Y. Xia, Q. F. Liu, and D. S. Xue, *Low current density spin-transfer torque effect assisted by in-plane microwave field*, Appl. Phys. Lett. **99**, 032502 (2011).

Y. Ren, J. Wang, Q. Liu, Y. Dai, B. Zhang, and L. Yan, *Tailoring coercivity and magnetic anisotropy of Co nanowire arrays by microstructure*, J. Mater. Sci. **46**, 7545 (2011).

List of presentations:

B. Zhang, C.-B. Wu, and W. Kuch: *Exchange bias and long-range magnetic interlayer coupling in Co/Mn/Co trilayers*. DPG Frühjahrstagung, Talk, 30.04.-04.04.2014, Dresden, Germany.

B. Zhang, C.-B. Wu, and W. Kuch: *Exchange bias and long-range magnetic interlayer coupling in Co/Mn/Co trilayers*. IEEE International Magnetics Conference, Talk, 04.05.-08.05.2014, Dresden, Germany.

B. Zhang, O. Sandig, J. Kurde, F. Kronast, and W. Kuch: *Laser-induced magnetization dynamics of Co/Ni/Cu(001) close to the spin reorientation transition observed by PEEM*. 21st International Colloquium on Magnetic Films and Surfaces (ICMFS), Poster, 24.-28.09.2012, Shanghai, P. R. China.

B. Zhang, O. Sandig, J. Kurde, F. Kronast, and W. Kuch: *Laser-induced precessional magnetization dynamics of epitaxial Co/Ni bilayers on Cu(001)*. Third Joint BER and BESSY Users Meeting, Poster, 30.11.-02.12.2011, Berlin, Germany.

B. Zhang, O. Sandig, J. Kurde, F. Kronast, and W. Kuch: *Laser-induced precessional magnetization dynamics of epitaxial magnetic layers*. Summer School SFB 616, Exciting Excitations: From Methods to Understanding, Poster, 25.-29.07.2011, Waldbreitbach, Germany.

Acknowledgments

First of all, I would like to express my sincere gratitude to my PhD supervisor, **Prof. Dr. Wolfgang Kuch**, for his support and fruitful discussions throughout my four years' studies. He always gave me precious advises on the experiments and on the interpretation of the results. His suggestions and ideas are meaningful and interesting. I benefited a lot from the discussion with him. His way of attentively and insightfully reviewing my papers as well as thesis was also very much appreciated.

I am also grateful to **Prof. Dr. Katharina J. Franke** for co-supervising my dissertation as a second supervisor and the opportunity to present my work in her group. I enjoyed the discussions with her.

I feel deeply grateful to **Dr. Julia Kurde**, she introduced me to the PEEM experiment at BESSY Ⅱ. I learned a lot from beginning to operate the instruments during two weeks beamtime. She was patient to tell me how to analyze the data as well as the nice ideas about the simulation.

I got a great help from **Dr. Chii-Bin Wu**. We made the chamber running, repaired the evaporator, set up the MOKE, got the first Auger data, the first MOKE data. He always shared his ideas and spent a lot of time for discussion.

Many thanks to **Dr. Yaqoob Khan**, this is my first time to know the vacuum chamber in the lab. Many useful discussions from him and thanks for his help for FP teaching. Thanks to **Oliver Sandig**, together with him I did the experiments at BESSY Ⅱ. I wish to thank **Yasser Shokr**, he used a lot of time to prepare the chamber and made the magnetic cores. It's my pleasure to work with him for the MOKE and PEEM experiment.

I am very much thankful to **Dr. Matthias Bernien**, he always offered his help at any time and he can resolve all the problems in the lab. Learning the STM from **Jiaming Song**, I will miss the time for helping each other. Thanks to **Dr. Felix Hermanns** for help with the cooling system and the magnetic coils. Also the help from **Alex Krüger**, especially for introduction to Latex is acknowledged. Many thanks to **Dr. Yin-Ming Chang**, designing the magnet for MOKE, and working together in the BESSY lab.

Thanks to all of the members of the **AG Kuch**, I am very happy to enjoy work with you. Many of the ideas can be dated back to the intense discussions with group members, which have always

been inspiring. I can still recall many of them that are fresh in my memory as if they had happened yesterday.

I also got the help from **Weiwei Wang**, who offered the simulation code. And thanks for the cooperation work for the time-resolved dynamic and skyrmion simulations.

Thanks for the PEEM team in BESSYⅡ, **Dr. Florian Kronast** and **Dr. Sergio Valencia**.

Many thanks to **Marion Badow**, she helped me to order all the things and to refund the bills. Thanks to **Uwe Lipowski** for technical support.

Thanks for the friends, especially for the people studying in Berlin, we encourage each other, have the full and interesting life here.

I gratefully acknowledge funding by the China Scholarship Council.

In the end, I want to thank my family, especially my parents wholeheartedly, for understanding and supporting me during my four years' study in a foreign country away from home. As it in a traditional Chinese poem says, it is hard for a small plant to repay the warmness of the sun (谁言寸草心，报得三春晖). I wish the expectation of my parents can be at least repaid by my endeavor and dedication embedded in the thesis.

Erklärung

I hereby declare to have written this thesis on my own. I have used no other literature and resources than the ones referenced. All text passages that are literal or logical copies from other publications have been marked accordingly. All figures and pictures have been created by me or their sources are referenced accordingly. This thesis has not been submitted in the same or a similar version to any other examination board.

Place, Date Signature